Effect of Disorder on Domain Wall Dynamics

ScuDo
Scuola di Dottorato ~ Doctoral School
WHAT YOU ARE, TAKES YOU FAR

Doctoral Dissertation
Doctoral Program in Physics (30^{th}cycle)

Effect of Disorder on Domain Wall Dynamics

By

Bhaskarjyoti Sarma

******

Supervisor(s):
Gianfranco Durin, Supervisor
Istituto Nazionale di Ricerca Metrologica (INRIM), Torino,
Italy

Doctoral Examination Committee:
Lasse Laurson, Tampere University of Technology, Tampere, Finland.
Liza Herrera Diez, CNRS - Université Paris Sud - Université Paris Saclay, Orsay, France.
Dario Daghero, Politecnico di Torino, Torino, Italy
Carlo Ricciardi, Politecnico di Torino, Torino, Italy
Alessandro Magni, Istituto Nazionale di Ricerca Metrologica (INRIM), Torino, Italy

Politecnico di Torino
2018

Declaration

I hereby declare that, the contents and organization of this dissertation constitute my own original work and does not compromise in any way the rights of third parties, including those relating to the security of personal data.

Bhaskarjyoti Sarma
2018

* This dissertation is presented in partial fulfillment of the requirements for **Ph.D. degree** in the Graduate School of Politecnico di Torino (ScuDo).

To my parents....

Acknowledgements

First of all, I express my gratitude to my supervisor Gianfranco Durin for giving me the opportunity to work in the interesting topic of domain wall dynamics, for being patient with me, helping and guiding me. I am extremely thankful to Felipe Garcia Sanchez and Arianna Casiraghi for their help, all the scientific and social discussions and close guidance. They were always ready to discuss with me any questions. Then I would like to thank each one of my PhD committee members for agreeing to be in my committee gracefully, reading my thesis and providing valuable comments to improve it.

I am thankful to the researchers from magnetism group at INRIM, in particular to Alessandro Magni for introducing me to MOKE microscopy, letting me to work and use their resources in the lab.

Thanks to my colleague Ali Nasseri and all the ITN-WALL mates for the memorable time as part of the WALL network. I could learn a lot from each one of them and I feel lucky to meet these wonderful group of people. Thanks to the PIs of ITN-WALL who helped me to build a foundation in magnetism through their lectures and discussions. Special thanks to Ben Van di Wiele from University of Gent, Dafine, Liza and Yuting from University of Paris-Sud, Samridh from University of Mainz and Singulus for giving their valuable time for me during my secondments and also for giving me the opportunity to learn and work in their labs.

Thanks to the administration of ISI Foundation for all the bureaucratic help.

My gratitude to my parents, brother, sister-in-law and my relatives for their support and understanding throughout my student life. It was very important to me.

Last but not the least, a special thanks to the European commission for providing me the funding to carry out this work.

Abstract

The purpose of this work is to study the effects of disorders on domain wall dynamics in perpendicular magnetic anisotropy ultra-thin ferromagnetic materials. It is done, firstly, by experimental study of domain wall dynamics in Ta/CoFeB/MgO material where distributions and strengths of pinning points are controlled by light ion irradiation and secondly, by micromagnetic study of the dynamics and morphology of a bubble domain in a disorder induced PMA material with Dzyaloshinskii-Moriya interaction.

By studying the effects of He^+ ion irradiation on domain wall dynamics, it is found that irradiation influences the distribution of pinning points as well as their strengths, thereby influencing the velocities of domain walls. The velocities are found to be lowest for non-irradiated samples, then it is observed to increase with irradiation and then decrease at higher irradiations suggesting that there is an optimum irradiation where velocity should be maximum.

On the other hand, by studying the dynamics of bubble domain using micromagnetic simulations in ultra-thin films with disorder and Dzyaloshinskii-Moriya interaction, it is found, as expected that magnetic bubbles expand asymmetrically along the axis of the in-plane field under the simultaneous application of out-of-plane and in-plane fields. Remarkably, the shape of the bubble was found to have a ripple-like part which caused a kink-like (steep decrease) feature in the velocity versus in-plane field curve. It is shown that these ripples originate due to the nucleation and interaction of vertical Bloch lines. Furthermore, it is also shown that the Dzyaloshinskii-Moriya interaction field is not constant, in contradiction with the results of experiments, but rather depends on the in-plane field.

Contents

List of Figures

List of Tables

Chapter 1

Introduction

Since the invention of writing in the ancient Mesopotamian civilization around 3100 BCE, humans have been evolving in the way knowledge is stored and accessed. Storage of knowledge, information or data has evolved from writing in stones in ancient times to writing on paper using ink and print technology in the last centuries and recently to storage based on analog and digital technologies. The forms of data generated everyday: text, audio or video are stored in analog or digital formats. Rapid advancement of technology has made us move from paper-based storage to technology based storage. Technology based storage started with the use of magnetic tape in 1928. Since then, it has improved enormously. It is estimated that an approximately 2.5 quintillion bytes of data are generated each day by 3.7 billion people (less than 50% of world's population) all around the globe. In a recent study, it was reported that world's capacity to store information has increased from less than three exabytes in 1986 to 295 exabytes in 2007, doubling each 3 years [1]. This number rose to 5 zetabytes ($5x10^{21}$ Bytes) in 2014 [2]. To put this number into perspective, this much amount of data if written in books is equivalent to stack of books covering 2.5 times the distances between earth and sun. With such huge amount of data to be stored and read, there is an enormous need to improve our current state of storage technology.

The state of a storage technology can be evaluated in terms of the parameters: storage density (amount of data that can be written per square unit area), speed (how fast given amount of data can be written and read), power consumption and cost. A study carried out in 2003 at University of California in Berkeley reported that

92% of all new informations generated in 2002 was stored on hard disk drives [3]. Therefore, improving the state of hard disc drives becomes the obvious focus for scientists. Present day hard disc technology consists of a magnetic material where data are written in terms of bits. Each bit is a uniformly magnetized part called domain and separated from the neighboring bit by a transition region called domain wall. Since the invention of the first hard disc drives in 1956, the storage capacity of hard disc has been improving exponentially. The most dramatic improvement came after the discovery of the Giant Magneto Resistance by Peter Grünberg [4] and Albert Fert [5] in 1989, which also led to the beginning of spintronics where the spin degree of freedom instead of the charge of an electron is exploited.

After decades of exponential improvement, current hard disc drives face two major challenges in terms of their ability to further improve their storage density because of fundamental limits and to avoid failure because of a mechanical read-write head. In order to solve these challenges, a new type of device called Racetrack Memory [6, 7] has been proposed. It is a 3 dimensional vertical array of nanowires where data is written in a domain of choice by a localized field from an Oersted line and read by a read-head by moving the domain to read-head as shown in figure 1.1. For realization of this device, we need to be able to precisely move the domain walls. Because of the promises offered by racetrack memory, domain wall dynamics has become an area of huge interest.

Not only racetrack memory, study of domain wall dynamics has attracted significant attention in the spintronics research community due to its potential for applications, but also in future logic [8] and sensing [9–11] devices. Although, DW dynamics holds lots of promises, yet there are many open questions that need to be understood for the realization of these devices in the future. Among these, we pursue two questions in this thesis. The first question deals with controlling domain wall motion by manipulation of the sample properties with high energy light ion irradiation at the local level. The second question investigates the dynamics and shape of a magnetic bubble domain under the influence of an external field and its consequence on the measurement of the Dzyaloshinskii-Moriya interaction (DMI), an interaction that significantly affects domain wall motion.

In order to answer these questions, the rest of the thesis is divided into the following chapters:

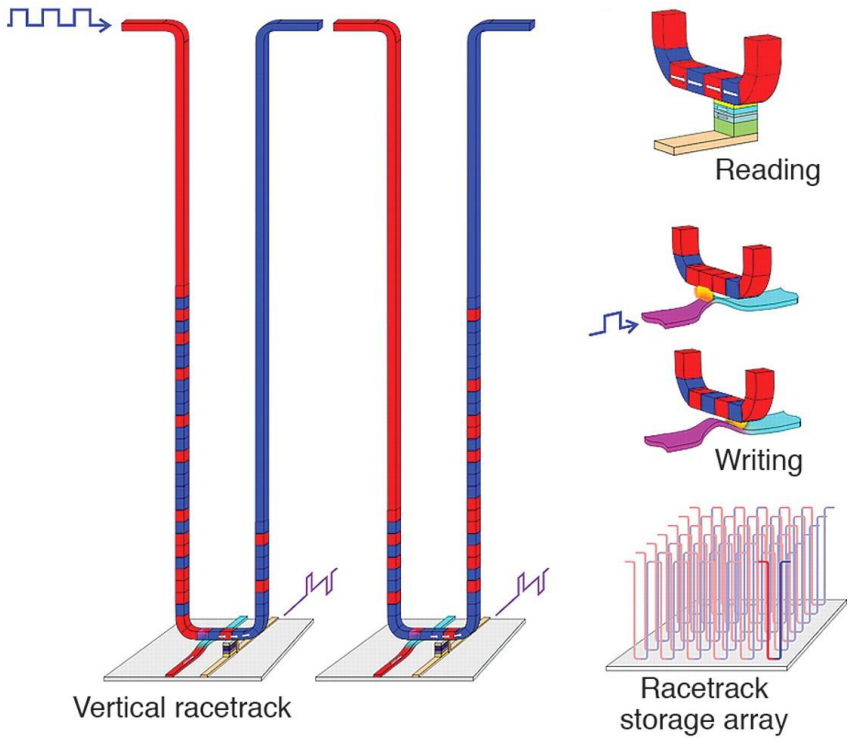

Fig. 1.1 Schematic of proposed racetrack memory based on ferromagnetic nanowire. Red and blue regions are domains with opposite magnetizations that works as bits to store information. In order to read or write a bit, all DWs are moved coherently with spin-polarized current pulses to the Reading or Writing location. Racetrack storage array can be built to achieve high density storage because of its 3-dimensional structure. Adapted from [6].

- **Chapter 2: Introduction to Ferromagnetism**
  In this chapter, we will present the theoretical background that is necessary to understand the work done in this thesis. At first, origin of ferromagnetism and different energies associated with ferromagnetic metals will be discussed in order to explain the formation of magnetic domains and domain walls. Then we will look at the means to move domain walls, explaining about the field and current driven domain wall motion along with the underlying physics. After this, a widely used analytical model, namely a 1D model for predicting motion of domain walls will be introduced. Finally, we will explain creep, the phenomenological model developed for domain wall dynamics in disordered media in the presence of low driving force.

- **Chapter 3: Methods**
  In this chapter, details of methods used for experiments and micromagnetic simulations performed in this thesis will be explained. First, a widely used growth method for ultra-thin film, sputtering, will be introduced and important characterization methods used for this films will be discussed. After explaining the irradiation process of thin films by high energy He^+ ions in brief, magneto optical Kerr effect microscopy, a method used for viewing domain walls and their motion, will be presented. Lastly, computational and numerical aspects of performing micromagnetic simulations for the motion of domain walls in graphical processing units will be explained.

- **Chapter 4: Controlling local pinning by light ion irradiation**
  For device applications, understanding the localized pinning points and their strength in the material are of extreme importance for precise prediction of the dynamics of domain walls. In this chapter, manipulation of local dynamics of domain wall with He^+ ion irradiation in perpendicularly magnetized Ta/CoFeB/MgO ultra-thin films will be discussed. Effect of irradiation on the macroscopic magnetic properties e.g. anisotropy, saturation magnetization etc. is also discussed.

- **Chapter 5: Dynamics and morphology of chiral magnetic bubbles in perpendicularly magnetized ultra-thin films**
  Recently, domain wall dynamics in ultra-thin films has been found to be significantly influenced by an interaction known as the Dzyaloshinskii-Moriya interaction (DMI) . In this chapter, we present the effect of DMI on the dy-

namics and morphology of a magnetic bubble domain using micromagnetic simulations. We also compare the results from micromagnetics with an analytical model.

- **Chapter 6: Conclusion and future perspective**
  In this chapter, conclusions derived from the work done in this thesis will be summarized. Then the open questions arising out of this work will be presented.

Chapter 2

Introduction to Ferromagnetism

In this chapter, a review of the fundamental concepts in order to understand origin of ferromagnetism and formation of magnetic domains and domain walls will be explained. After that, different ways to move domain walls along with a discussion on different models used for predicting DW motion will be presented.

2.1 Atomic magnetic moments

In order to understand origin of magnetism, that we experience in our everyday life at the macroscopic or even at microscopic level, we will start at the atomic level. Matter consists of atoms. Let us consider the classical picture of an atom, that consists of negatively charged electrons revolving around the positively charged nucleus. Coulomb's forces of attraction between an electron and the nucleus is balanced by the centrifugal force due to its circular motion preventing the electron from collapsing into the nucleus. Electron has both charge ($q_e = -1.6 \times 10^{-19}$ coulombs) and mass ($m_e = 9.1 \times 10^{-31} kg$) and it has two kinds of motion. One is orbital motion around the nucleus and the other one is spin i.e. rotation about its own axis. Because of these motions it has two kinds of angular momentum: orbital angular momentum and spin angular momentum. From classical mechanics, orbital angular momentum (L) of the electron because of its uniform orbital motion with radius of its orbit r is $m_e vr$, where v is the velocity of the electron . On the other hand, magnetic moment due to an electron orbiting around the nucleus in a system as shown in figure 2.1 is IA where I is the electric current in the orbit due to the motion

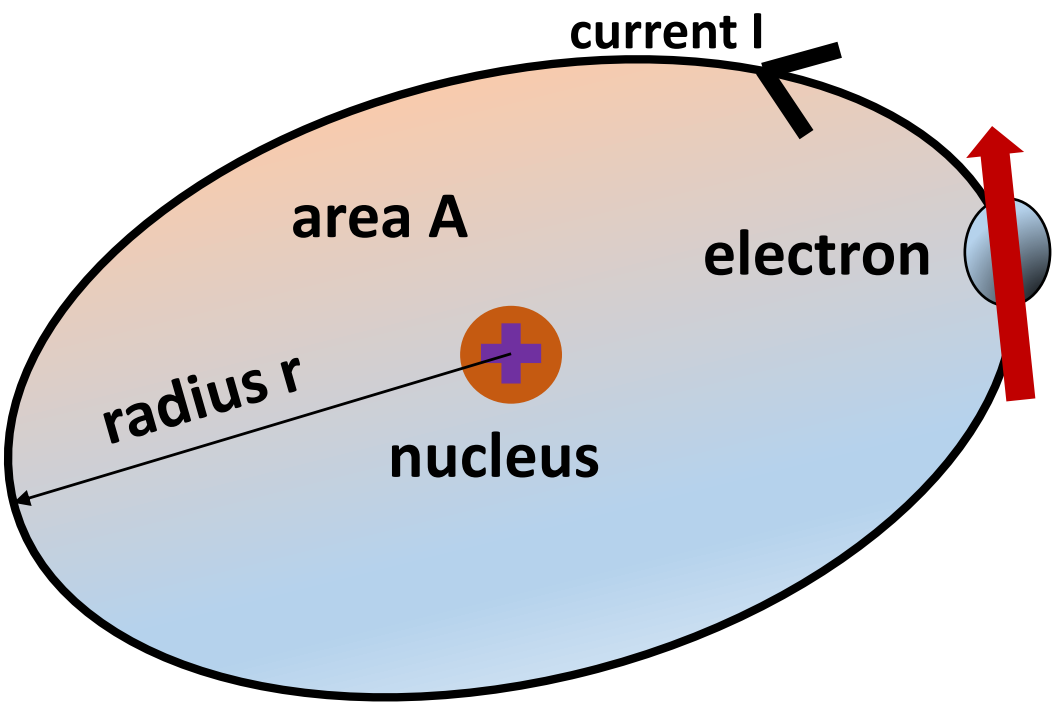

Fig. 2.1 Schematic of motion of an electron around its nucleus giving rise to magnetic moment.

of electron and A is surface area enclosed by the loop with its unit Am^2. Replacing I with $\frac{q_e}{T}$, where T is the time taken to complete one complete rotation and A with πr^2 we get the expression for magnetic moment as:

$$IA = \frac{q_e v_e r}{2} = \frac{q_e}{2m_e} m_e v_e r = \frac{q_e}{2m_e} L \tag{2.1}$$

The above equation tells us that magnetic moment is proportional to orbital angular momentum and direction of magnetic moment is opposite to the direction of orbital angular momentum, since q_e is negative. The proportionality factor $\left(\frac{q_e}{2m_e}\right)$ between magnetic moment (IA) and orbital angular momentum (L) is called the gyromagnetic ratio (γ). Bohr theory proposes that angular momentum of an electron is quantized in the following form:

$$L = n\frac{h}{2\pi} = n\hbar \tag{2.2}$$

where n is any integer number. In the ground state $n = 1$ and the magnetic moment due to an electron, called as *Bohr magneton* (μ_B) becomes $\mu_B = \gamma L = \frac{q_e}{2m_e}\hbar =$

$9.274 \times 10^{-24} Am^2$ (or J/T). Bohr magneton is a convenient and widely used unit of magnetic moment.

However, value of gyromagnetic ratio due to spin of electron is $\frac{q_e}{m_e}$, meaning that gyromagnetic ratio due to spin of an electron is twice due to its orbital motion. Therefore, spin of the electron is twice effective in contributing to magnetic moment.

Total angular momentum of an electron is the sum of its orbital angular momentum ($\mathbf{L}$) and spin angular momentum ($\mathbf{S}$). In order to calculate the magnetic moment due to a single atom in a macroscopic material, we need to embark on quantum mechanics. Magnetic moment due to a single atom is given by the following formula:

$$\boldsymbol{\mu} = -g\mu_B \sqrt{\mathbf{J}(\mathbf{J}+1)} \tag{2.3}$$

where $\mathbf{J} = \mathbf{L} + \mathbf{S}$ is the total angular momentum and g is the Lande factor and is a function of $\mathbf{L}$, $\mathbf{S}$ and $\mathbf{J}$ in the following way:

$$g = 1 + \frac{J(J+1) + S(S+1) - L(L+1)}{2J(J+1)} \tag{2.4}$$

Orbital angular momentum ($\mathbf{L}$) and spin angular momentum ($\mathbf{S}$) can be calculated from the quantum numbers of electrons. In table 2.1, we calculate the atomic magnetic moments of three most widely used 3d ferromagnetic metals: Fe, Co and Ni. Below $3d$ shells, all are fully occupied and paired electrons with opposite spin does not contribute to the magnetic moment, because they cancel each other. For Fe, calculating orbital angular momentum from its orbital angular quantum number (m_l) we get $L = 2$ and calculating spin angular momentum from spin quantum number (s), we get $S = 2$. According to Hund's rule, $J = L + S$ since the orbital is more than or equal to half-filled. By knowing L, S and J, Lande factor g can be calculated from equation 2.4 above and magnetic moment due to one atom of Fe from equation 2.3 becomes 6.71 μ_B. Similarly, it can be calculated for Co, Ni and other atoms as well.

Based on this calculation of the atomic magnetic moment, it seems that all materials having unpaired electrons will be magnetic. However, later we will see that even though individual atoms may have a magnetic moment, it still may not be magnetic macroscopically. This depends on the interaction among individual moments, that governs the macroscopic behavior of the material.

Atom	Configuration	L	S	J	g	μ (μ_B)
Fe	[Ar] 3d ↑↓ ↑ ↑ ↑ ↑ 4s ↑↓	2	2	4	1.5	6.71
Co	[Ar] ↑↓ ↑↓ ↑ ↑ ↑ ↑↓	3	3/2	9/2	1.33	6.61
Ni	[Ar] ↑↓ ↑↓ ↑↓ ↑ ↑ ↑↓	3	1	4	1.25	5.59

Table 2.1 Calculation of atomic magnetic moments for Fe, Co and Ni ferromagnetic metal atoms.

2.2 Micromagnetic Free Energies

In the previous section, we have seen the origin of atomic magnetic moments. Now we will look at the micromagnetic energy terms that dictate the orientation of these moments in a material and therefore, type of the magnetic material.

Exchange energy

Exchange energy favors two neighboring magnetic moments to align parallel or antiparallel to each other. The expression for exchange interaction is:

$$E_{ex} = -J\,\mathbf{S}_i \cdot \mathbf{S}_j \tag{2.5}$$

where $\mathbf{S}_i$ and $\mathbf{S}_j$ are two neighboring magnetic moments and J is the exchange integral. J determines whether a magnetic material is ferromagnetic or antiferromagnetic as shown in figure 2.2. If $J > 0$, neighboring magnetic moments prefer to align in the parallel direction and leads to a ferromagnetic material. If J<0, neighboring magnetic moments prefer to align in the anti-parallel direction and leads to an antiferromagnetic material. From this figure, we can also see that the ratio of atomic separation to radius of the unfilled 3d shell is a key parameter in determining whether a material is ferromagnet or antiferromagnet. If this value is above around 1.5 e.g. as in Fe, Co and Ni, it is ferromagnet and it is antiferromagnet otherwise. Exchange is a short range interaction and is the strongest interaction locally. It is quantum mechanical in origin and results from the Pauli's exclusion principle.

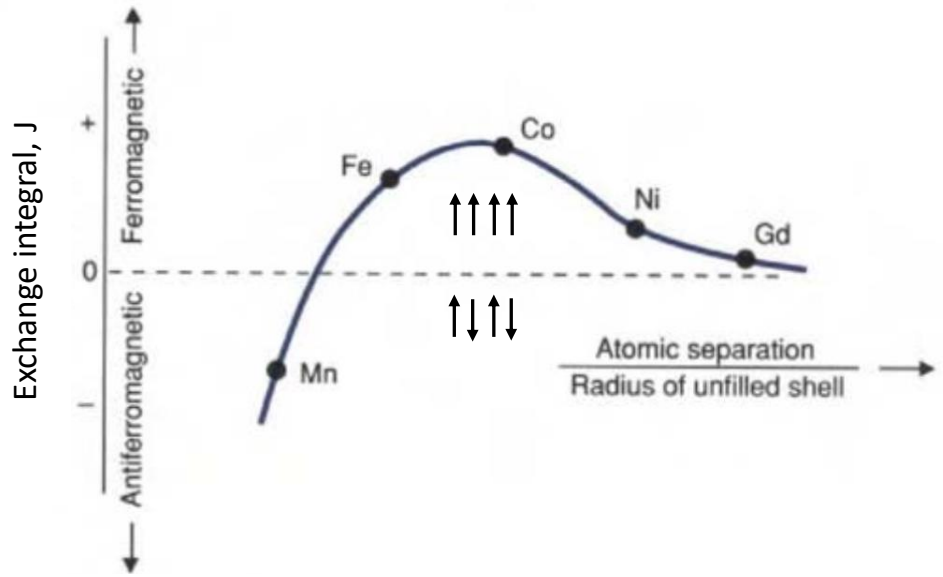

Fig. 2.2 Exchange integral as a function of ratio of atomic distance to radius of the unfilled 3d shell for some ferromagnets and antiferromagnets. Adapted from [13].

Different forms of model exist for the exchange interaction. Two phenomenological models are the band or itinerant electron model and the localized moment model [12]. Some other models for specific forms of exchange interactions are RKKY interaction, double exchange and superexchange.

Micromagnetic expression for exchange energy density is written as:

$$E_{ex} = A[(\nabla m_x)^2 + (\nabla m_y)^2 + (\nabla m_z)^2] \tag{2.6}$$

where A is the exchange stiffness constant expressed in J/m or erg/cm. It is a material property and its value can be measured experimentally from the dispersion relation of spin-wave resonance [14]. The typical values of this constant are in the range of 0.1-20 pJ/m. It can also be calculated using the Ab-initio density functional theory [15]. A depends on temperature and the expression for its value at absolute zero temperature is $A(T = 0K) \approx \frac{k_B T_C}{a}$ where T_C is the Curie temperature, k_B is the Boltzmann constant and a is the lattice constant of the material.

Anisotropy energy

Anisotropy energy considers the preference of magnetic moments to align along a

particular direction, known as easy axis. There are different sources of anisotropy energy. One principal source is magnetocrystalline anisotropy energy originating from spin-orbit coupling (LS) and ionic crystal field. Therefore, easy axis direction is defined by the crystal structure of the material. Expression for uniaxial anisotropy energy density to the second term can be written as:

$$E_{an} = -K_{u1}(\mathbf{m}\cdot\mathbf{e})^2 + K_{u2}(\mathbf{m}\cdot\mathbf{e})^4 \tag{2.7}$$

where **e** is the easy axis vector. Anisotropy constants K_{u1} and K_{u2} have the units of energy density and depend on composition and temperature. Although higher order terms to the above equation can be added, their contribution is not significant [16]. Energy density E_{an} depends on the relative orientation of **m** with respect to easy axis vector **e**. If we consider only the first order term and $K_{u1} > 0$ anisotropy is axial. On the other hand, if $K_{u1} < 0$ then the anisotropy is planar in a direction perpendicular to the easy axis.

Cubic anisotropy density for materials having cubic symmetry is expressed as:

$$E_{an,cubic} = K_{c1}(m_x^2 m_y^2 + m_y^2 m_z^2 + m_z^2 m_x^2) + K_{c2} m_x^2 m_y^2 m_z^2 \tag{2.8}$$

where m_x,m_y and m_z are the components of m along the axes of cubic lattice and K_{c1}, K_{c2} are cubic anisotropy constants with units of energy density. If $K_{c1} > 0$ as in the case of BCC iron and ignoring K_{c2}, energy is minimum along the [100] direction. Thus [100] is the easy axis. Due to cubic symmetry [010] and [001] are also easy axes. If $K_{c1} < 0$, as in the case of FCC Nickel and ignoring K_{c2}, energy is minimum along the [111] directions. Values of K_{c1} for Fe at $20^{\circ}C$ and for Ni at $23^{\circ}C$ are $4.72 \times 10^4\ J/m^3$ and $-5.7 \times 10^3\ J/m^3$ respectively [13].

Another source of anisotropy important in ultra-thin films and nanostructures with a high surface area to volume ratio is the surface anisotropy. It has its origin in the spin-orbit coupling in the same way with magnetocrystalline energy. It arises because magnetic moment of atoms at the vicinity of surface have different energies from the atoms at the bulk. If the number of atoms at the surfaces are much more than the atoms at the bulk as in nanostructured materials, contribution from this anisotropy become significant. Effective anisotropy in the material is a combination

of surface and bulk anisotropy that can be expressed in the following way:

$$K_{eff} = K_{an,bulk} + \frac{K_{an,s}}{d} \tag{2.9}$$

where K_{bulk} is the bulk anisotropy constant with unit J/m^3, that considers the contribution from magnetocrystalline anisotropy and magnetostatic energy (discussed later), $K_{an,s}$ is the surface anisotropy constant with unit J/m^2 and d is the thickness of the material. As thickness of the material becomes smaller and smaller, this contribution become more and more significant.

Expression for energy density due to surface anisotropy to the first order can be written as:

$$E_{an,s} = K_{an,s}\left[1 - (\mathbf{m}\cdot\mathbf{n})^2\right] \tag{2.10}$$

Surface anisotropy constant $K_{an,s}$ is expressed in J/m^2. When $K_{an,s} > 0$, it favors the perpendicular alignment of magnetic moment with respect to plane of material leading to perpendicularly magnetic anisotropy material.

Other than magnetocrystalline and surface anisotropy, there are other sources of anisotropies as well e.g. magnetoelastic and shape anisotropy. Magnetoelastic anisotropy leads to a change in the magnetization due to mechanical strain applied to the material or a change in its shape due to the application of an external field. This anisotropy is not relevant in this thesis and therefore not discussed in detail. Shape anisotropy will be discussed later in brief along with magnetostatic energy.

Exchange interaction, discussed before is isotropic meaning that it is in its minimum energy condition as long as ferromagnetic or antiferromagnetic order is maintained. Therefore it is anisotropy energy that determines along which direction the material will maintain the ferromagnetic or antiferromagnetic order.

Zeeman energy

Zeeman energy is the term that describes the effect of an external magnetic field ($\mu_0\mathbf{H}$) on the magnetic moments. Expression for this energy density is given by:

$$E_{Zeeman} = -\mu_0\,(\mathbf{m}\cdot\mathbf{H}) \tag{2.11}$$

where μ_0 is the permeability in vacuum. Value of this energy depends on the angle between the magnetization and the external field. It is minimum when both are in

the same direction. Thus, Zeeman energy favors the magnetic moment to align along the external magnetic field.

Magnetostatic energy

Magnetostatic energy originates as a result of dipolar energy due to interaction between two magnetic moments. Expression for dipolar energy is given by:

$$E_{dipolar} = \frac{\mathbf{m}_i \cdot \mathbf{m}_j}{r_{ij}^3} - \frac{3(\mathbf{m}_i \cdot \mathbf{r}_{ij})(\mathbf{m}_j \cdot \mathbf{r}_{ij})}{r_{ij}^5} \tag{2.12}$$

where $\boldsymbol{m}_i$ and $\boldsymbol{m}_j$ are two magnetic moments and $\boldsymbol{r}_{ij}$ is the position vector between the two moments. Dipolar energy is a long range interaction and it is the only non-local energy. Therefore, while calculating magnetostatic energies of the magnetic sample, it needs to be summed for all magnetic moments inside volume of the sample.

From another perspective, if we consider a material magnetized in one direction, then a stray field outside the sample and a demagnetizing field (H_{demag}) inside the sample are generated. Demagnetizing field opposes the internal magnetization direction. Expression for the demagnetizing field is:

$$\mathbf{H}_d = -N\mathbf{M} \tag{2.13}$$

where N is the demagnetizing tensor. For a perpendicularly magnetized infinite sample $N = 1$. Expression for magnetostatic energy density is given by:

$$E_{ms} = -\frac{1}{2}\,\mu_0\,\mathbf{H}_d \cdot \mathbf{M} \tag{2.14}$$

Magnetostatic energy can only be reduced by avoiding the formation of magnetic charges. Magnetic surface charges are given by the expression:

$$\sigma = (\mathbf{M} \cdot \mathbf{n}) \tag{2.15}$$

where $\mathbf{n}$ is the vector along the surface normal. In order to avoid surface charges, magnetization tend to align along the boundaries.

As a consequence of magnetization trying to minimize surface charges, magnetostatic energy is responsible for the formation of domains in ferromagnetic materials. A domain is a region with individual magnetic moments aligned in one direction as

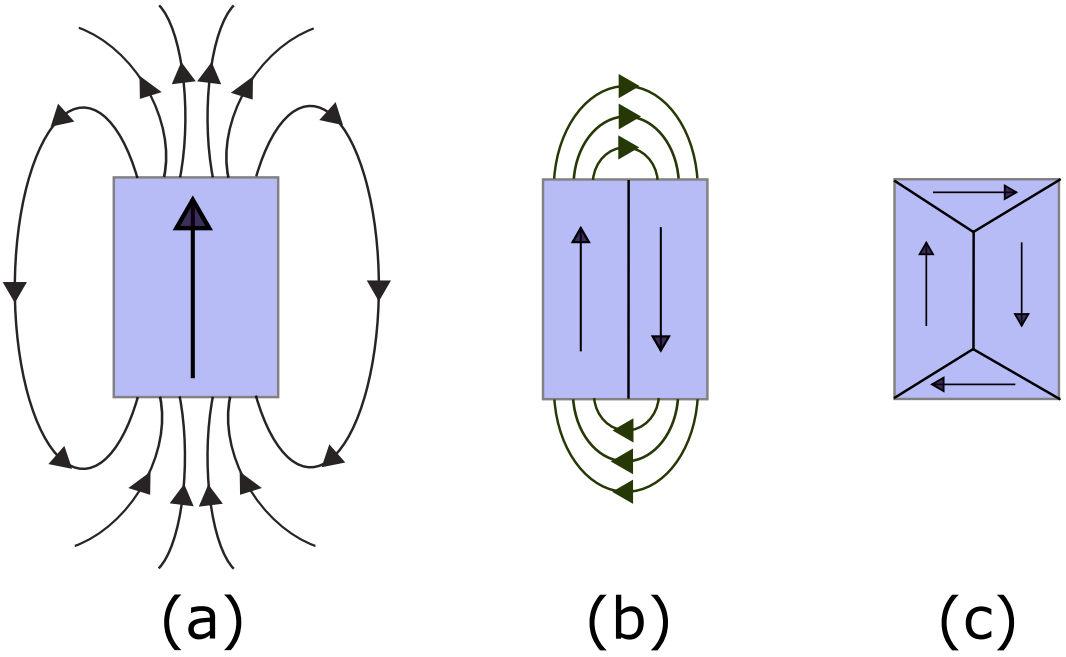

Fig. 2.3 Schematic of the change in strength of the stray field due to the formation magnetic domains.

shown in figure 2.3. Between two domains there is a domain wall, a region through which a gradual change of magnetization from one direction to another take place. A sample with single domain structure has the maximum magnetostatic energy.

2.3 Domain walls

As discussed previously, domains exist in ferromagnetic materials to minimize the magnetostatic energy. Inside domains magnetizations are aligned along the easy axis direction. Between two neighboring domains, there is a domain wall. Domain wall (DW) is the region where magnetization gradually make a transition from one direction of the easy axis to another direction. The reduction in magnetostatic energies however comes at the cost of increase in energy due to the formation of DWs. Therefore, the competition between magnetostatic energy and DW energy decides the size of domains. On the other hand, size of the domain wall is determined by the competition between exchange energy and uniaxial anisotropy energy. Exchange energy wants to make the DW as thick as possible, while anisotropy wants to make the DW as thin as possible. Between this, DW finds its stable width.

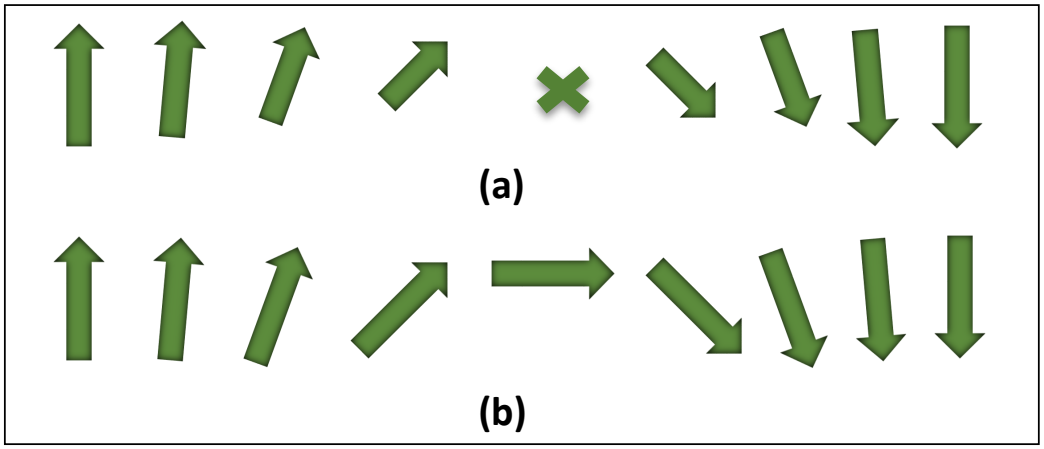

Fig. 2.4 Schematic of Bloch wall (a) and Néel wall (b).

Depending on how magnetization inside the domain wall changes from border of one domain to the other, DWs are classified into different types. When the angle between magnetizations in two neighboring domain is 90° or 180°, then the DW is called a 90° or 180° DW. Depending on the angle between plane of rotation of the magnetization and plane of the wall, 180° walls are further divided into Bloch DW and Néel DW. In Bloch DW, plane of rotation of the magnetization is parallel to the plane of the wall while it is perpendicular for Néel DW. A schematic of these two types of DWs are shown in 2.4.

2.4 Dzyaloshinskii-Moriya interaction

Dzyaloshinskii-Moriya interaction (DMI) is a type of exchange interaction discussed in section 2.2. Origin of its study goes to long time ago, when some antiferromagnets e.g. Fe_2O_3, $MnCO_3$ and $CoCO_3$ showed weak ferromagnetism. In order to explain the weak ferromagnetism in these materials, Dzyaloshinskii phenomenologically postulated an antisymmetric exchange interaction that favors a canting of the neighboring spins, instead of parallel or antiparallel alignment as in Heisenberg exchange interaction described before. Later, Moriya developed it further by considering its physical origin spin-orbit coupling. The Hamiltonian for this interaction between two neighboring spins, S_1 and S_2 as shown in figure 2.5 is given by:

$$\mathscr{H}_{12} = -\mathbf{D}_{12} \cdot (\mathbf{S}_1 \times \mathbf{S}_2) \tag{2.16}$$

where $\mathbf{D}_{12}$ is the Dzyaloshinskii-Moriya interaction vector. In this figure, a ferromagnetic layer (in grey color) is on the top of a heavy metal layer (e.g. Pt, Pd, Ta etc.). DMI interaction is mediated through the heavy metal atoms. The direction of the DMI vector is perpendicular to the plane containing both the spins and the heavy metal atom. From equation 2.16, the energy is minimum when neighboring spins are orthogonal to each other. Depending on the sign of DMI vector, neighboring spins are canted towards or away from each other. The above equation also tells that when neighboring spins are parallel to each other as inside a domain in the ferromagnet or antiparallel to each other as in an antiferromagnet, DMI energy contribution from those spins is zero. It is only inside the domain wall in ferromagnet, from where DMI energy gets its contribution.

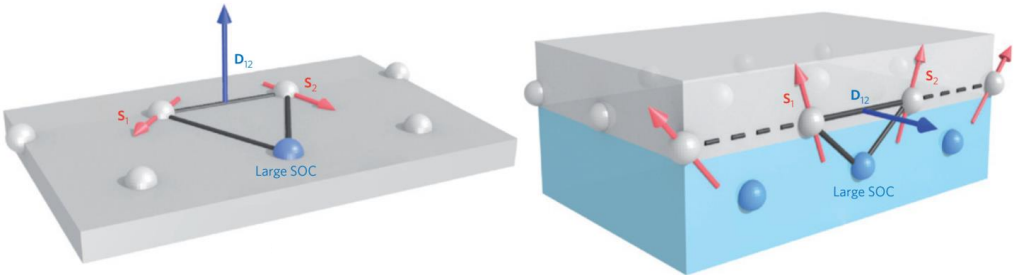

Fig. 2.5 Schematic of the Dzyaloshinskii-Moriya interaction in a ferromagnetic layer (gray) due to the presence of a heavy metal layer (blue). Adapted from [17].

For DMI to exist in a material, material needs to have a structural inversion asymmetry (SIA). There are some naturally occurring materials e.g. B20 compounds that has SIA and as a consequence of that it exhibits DMI naturally [18]. However with the advancement of material growth technology, it has become possible to produce or grow artificial materials where symmetry can be broken at the interface between two adjacent layers. The two adjacent layers on both sides of the interface maintain having uniform crystal structures with an inversion center between them. Some examples of artificially produced systems that showed presence of DMI are material where a heavy metal impurity atom with strong spin-orbit coupling is placed next to a magnetic atom [19, 20] in spin glasses, material with an ultra-thin magnetic film on the top or below a heavy metal atom layer [21–23] or even material where defects [24] are introduced to create SIA. Perpendicularly magnetized ultra-thin films that are studied in this thesis are deposited having a heavy metal layer on one or both sides of the ferromagnet. Most significant effect of DMI on the

perpendicularly magnetized ultra-thin films is that it dictates inside the domain wall how the magnetization rotates from one side to the other. Depending on different rotation scheme, it raises or lowers the DMI energy. Usually in these films without DMI, a Bloch wall is energetically favored because it lowers the demagnetizing energy. However if DMI interaction is present, a Néel wall is favored. Depending on the sense of rotation (chirality) as shown in figure 2.6, which is influenced by the sign of DMI, it can be a right hand (positive DMI) or left hand (negative DMI) chiral domain wall.

Micromagnetic expression for energy, expressed in energy per unit surface area due to interfacial DMI is written in the following form [25]:

$$E_{DMI} = D\left(m_z\frac{\partial m_x}{\partial x} - m_x\frac{\partial m_z}{\partial x} + m_z\frac{\partial m_y}{\partial y} - m_y\frac{\partial m_z}{\partial y}\right) \tag{2.17}$$

Integrating this equation over the interface area, expression for the total energy becomes [25, 26]:

$$\varepsilon_{DMI} = -\pi D d_{film}\cos\phi \tag{2.18}$$

The above equation shows that energy is minimum when $\phi = 0$ (D>0) or $\phi = \pi$ (D<0). On the other hand, one can write the expression for Zeeman energy in the presence of an in-plane field as:

$$\varepsilon_{Zeeman,ip} = -\pi\mu_0 M_s \Delta d_{film}(H_x\cos\phi - H_y\sin\phi) \tag{2.19}$$

From equations 2.18 and 2.19, one can interpret the effect of DMI as an effective in-plane field H_x, acting perpendicular to the domain wall. Direction of this field depends on the sign of DMI.

2.5 Magnetization Dynamics

In the introduction, we discussed about the need for understanding motion of DWs. There are two fundamental ways by which a domain wall can be moved: by external magnetic field or by spin polarized current. Below we discuss the mechanism by which an external field or spin polarized current can lead to the motion of DWs.

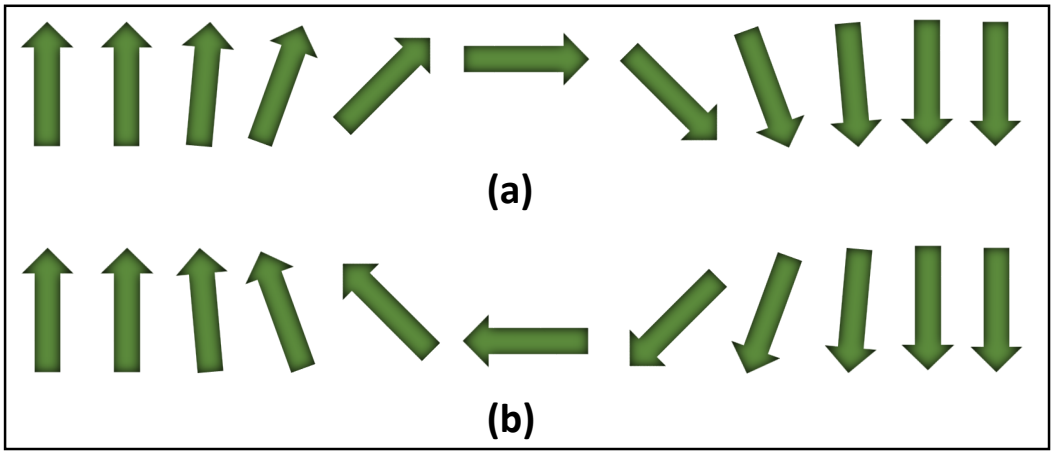

Fig. 2.6 Schematic of right hand (clockwise sense of rotation) and left hand (anticlockwise sense of rotation) chiral Néel DW in a perpendicularly magnetized ultra-thin film.

2.5.1 Field induced magnetization dynamics

Now we will see what happens to the magnetization when an external magnetic field is applied. If the magnetization is represented by $\mathbf{M}$, then the torque ($\boldsymbol{\tau}$) acting on the magnetization due to an external homogeneous magnetic field ($\mu_0\mathbf{H}$) can be written in the following form:

$$\boldsymbol{\tau} = \mathbf{M} \times \mu_0 \mathbf{H} \tag{2.20}$$

On the other hand, torque is equal to the rate of change of angular momentum. From the relationship between angular momentum and magnetic moment we get:

$$\boldsymbol{\tau} = \frac{d\mathbf{L}}{dt} = \frac{1}{\gamma}\frac{d\mathbf{M}}{dt} \tag{2.21}$$

Therefore, from the above two equations we get:

$$\frac{d\mathbf{M}}{dt} = \gamma\,(\mathbf{M} \times \mu_0 \mathbf{H}) \tag{2.22}$$

This expression tells us how the individual magnetic moments at the atomistic level evolve with time when an external field is applied. It tells that rate of change of magnetic moment is perpendicular to both magnetic moment and field vector. It also tells that magnetic moment precesses around the external field keeping the angle

between them fixed. Magnetic moment never reaches equilibrium, unless field is already aligned with the moment. The frequency with which the moment precesses around the moment is also called as Larmor frequency and is equal to $\frac{\gamma\,\mu_0|\mathbf{H}|}{2\pi}$.

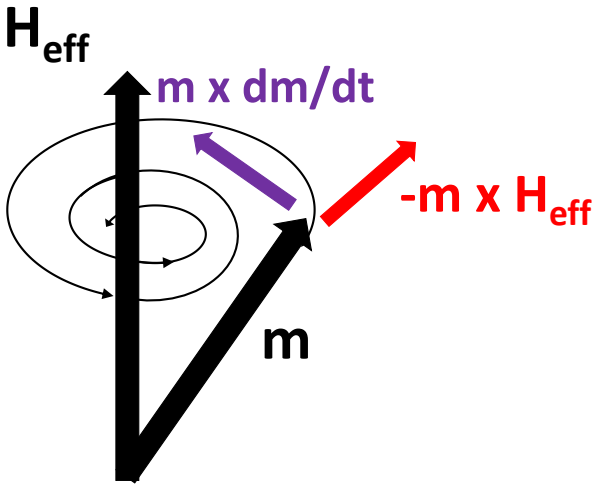

Fig. 2.7 Precession (in red) and damping (in blue) of a magnetic moment due to an effective field H_{eff}.

Based on the fundamental idea of the torque, Landau and Lifshitz first proposed field driven magnetization dynamics considering it in terms of an effect of an effective field ($\mathbf{H}_{eff}$). Effective field takes into account all the internal interactions of the magnetic material and also the effect of external form:

$$\mathbf{H}_{eff} = -\frac{1}{\mu_0}\frac{dE}{d\mathbf{M}} \tag{2.23}$$

where, μ_0 is the magnetic permeability in vacuum, E is the total energy density and $\mathbf{M}$ is the magnetization vector.Total energy takes into account all the micromagnetic energy contributions discussed earlier:

$$E = E_{an} + E_{ex} + E_{ms} + E_{DMI} + E_{Zeeman} + ... \tag{2.24}$$

Replacing $\mathbf{H}$ by $\mathbf{H}_{eff}$ in equation 2.22, Landau-Lifshitz equation becomes:

$$\frac{d\mathbf{M}}{dt} = \gamma \left(\mathbf{M} \times \mu_0 \mathbf{H}_{eff}\right) \tag{2.25}$$

Unlike the above equation, in experiments however, it was observed that magnetic moment precesses around the effective field and eventually aligns along with it. This is because, in reality, there are loss mechanisms due to excitation of spin waves, eddy current, phonon excitations via spin-lattice coupling etc [27]. In order to account for this, Landau and Lifshitz introduced a phenomenological damping torque to the equation 2.25:

$$\frac{d\mathbf{M}}{dt} = -\gamma\, \mathbf{M} \times \mu_0 \mathbf{H}_{eff} - \alpha_{LL}\, \mathbf{M} \times (\mathbf{M} \times \mathbf{H}_{eff}) \tag{2.26}$$

where α_{LL} is the damping parameter, a dimensionless coefficient. First term is the precession term and second term is the damping term, that takes into account all the relaxation mechanisms.

One convenient way to express this equation is in terms of reduced magnetization $\mathbf{m} = \frac{\mathbf{M}}{M_s}$. It has unit magnitude and direction same as the magnetization vector $\mathbf{M}$.

Later, Gilbert phenomenologically took into account for the relaxation mechanism by introducing a viscous force proportional to $\mathbf{m} \times \frac{d\mathbf{m}}{dt}$:

$$\frac{d\mathbf{m}}{dt} = -\gamma\, \mathbf{m} \times \mu_0 \mathbf{H}_{eff} + \alpha_G\, \mathbf{m} \times \frac{d\mathbf{m}}{dt} \tag{2.27}$$

This equation is known as Landau-Lifshitz-Gilbert (LLG) equation. The motion of the magnetic moment becomes slower for higher $\frac{d\mathbf{m}}{dt}$, in principle with the viscous motion. The precession term and damping term from this equation are illustrated in figure 2.7 in order to show the mechanism by which the magnetization aligns along the direction of effective field.

Equation 2.26 (Landau-Lifshitz) and 2.27 (Landau-Lifshitz-Gilbert) are equivalent to each other and the former can be derived from the later by vector cross multiplication of both sides of the equation with $\mathbf{m}$.

$$\mathbf{m} \times \frac{d\mathbf{m}}{dt} = -\gamma_0\, \mathbf{m} \times (\mathbf{m} \times \mathbf{H}_{eff}) + \alpha_G\, \mathbf{m} \times (\mathbf{m} \times \frac{d\mathbf{m}}{dt}) \tag{2.28}$$

where the product of γ and μ_0 is replaced by γ_0. Then using the following property of vector cross multiplication:

$$\mathbf{a} \times (\mathbf{b} \times \mathbf{c}) = (\mathbf{a} \cdot \mathbf{c})\, \mathbf{b} - (\mathbf{a} \cdot \mathbf{b})\, \mathbf{c} \tag{2.29}$$

we get:

$$\mathbf{m} \times \frac{d\mathbf{m}}{dt} = -\gamma_0\, \mathbf{m} \times (\mathbf{m} \times \mathbf{H}_{eff}) + \alpha \left[\left(\mathbf{m} \cdot \frac{d\mathbf{m}}{dt} \right) \mathbf{m} - (\mathbf{m} \cdot \mathbf{m}) \frac{d\mathbf{m}}{dt} \right] \tag{2.30}$$

In the above equation $\mathbf{m} \cdot \frac{d\mathbf{m}}{dt} = 0$ because both the vectors are perpendicular to each other and $\mathbf{m} \cdot \mathbf{m} = 1$. This yields:

$$\mathbf{m} \times \frac{d\mathbf{m}}{dt} = -\gamma_0\, \mathbf{m} \times (\mathbf{m} \times \mathbf{H}_{eff}) - \alpha\, \frac{d\mathbf{m}}{dt} \tag{2.31}$$

Taking this expression for $\mathbf{m} \times \frac{d\mathbf{m}}{dt}$ from the above equation, putting them in equation 2.27 and then rearranging the terms we can get:

$$\frac{d\mathbf{m}}{dt} = -\frac{\gamma_0}{1+\alpha^2} \left[(\mathbf{m} \times \mathbf{H}_{eff}) + \alpha\, \mathbf{m} \times (\mathbf{m} \times \mathbf{H}_{eff}) \right] \tag{2.32}$$

This is the explicit form of the Landau-Lifshitz-Gilbert equation. This form can be obtained from Landau-Lifshitz equation by renormalizing its precession and damping term with $\frac{\gamma_0}{1+\alpha^2}$ and $\frac{\gamma_0\, \alpha}{1+\alpha^2}$. This equation is used for the numerical micromagnetic simulations done in this thesis. This form of the equation is preferred over the other form, because here the time derivative of the magnetization is only in the left hand side of the equation.

2.5.2 Current induced magnetization dynamics

Even though current induced magnetization dynamics has been the topic of investigation along with field induced dynamics since the 1970s, underlying mechanism behind current induced dynamics was not easily understood as the field induced one. Current induced magnetization dynamics can be viewed as the result of interaction between conduction electrons, that are at or above the Fermi level and localized

electrons, that are below the Fermi level. L. Berger in his series of papers [28–34] in the 70's dealt with this interaction. In the meantime, first experimental evidence of current induced motion of DWs was demonstrated by Freitas [35] and Hung [36] in permalloy. In order to explain the motion of DWs by conduction electrons, Berger proposed [28, 29] that conduction electrons can interact with the magnetic moments inside a DW through s-d exchange interaction. Conduction electrons (charge current) that contains equal amount of spin-up or spin-down electrons, when pass through a ferromagnet become spin polarized, i.e. number of one spin is more than the other, and these spin polarized electrons interact with the magnetic moments inside the DW.

Later on, many scientists, starting with Slonczewsi [37], tried to explain the magnetization dynamics under current by adding additional terms to the LLG equation. It was assumed that the angular momentum of the conduction electrons follow that of the localized electrons and there is a complete transfer of momentum from conduction electrons to the localized ones. This was called as the adiabatic hypothesis. Later on, a non-adiabatic term was considered in order to take into account for the mistracking between the conduction electron spin and localized moment. Tatara [38], Waintal [39] and Vanhaverbeke [40] added two spin transfer torques (STT): adiabatic and non-adiabatic, as the effect of spin-polarized currents to the LLG equation.

Lately, Zhang and Li [41] modeled the effect of conduction electrons in terms of an "s-d" Hamiltonian $H_{s-d} = -J_{ex}\,\vec{s}\cdot\vec{S}$, where s and S are spins of conduction and localized electrons and J_{ex} is the exchange coupling strength between them. Shortly after that, Thiaville et al. [42] modified the LLG equation by including a phenomenological non-adiabatic parameter in the following form:

$$\frac{d\mathbf{m}}{dt} = -\gamma_0\,\mathbf{m}\times\mathbf{H}_{eff} + \alpha\,\mathbf{m}\times\frac{d\mathbf{m}}{dt} - \overbrace{[\mathbf{u}\cdot\nabla]\mathbf{m}}^{adiabatic\ term} + \overbrace{\beta\mathbf{m}\times[(\mathbf{u}\cdot\nabla)\mathbf{m}]}^{non-adiabatic\ term} \tag{2.33}$$

where, **u** is a vector along the direction of the electron motion and its magnitude is given by:

$$u = \frac{J\,P\,g\,\mu_B}{2\,e\,M_s} \tag{2.34}$$

Here, J is the current density in A/m^2, P is the polarization of the spin-polarized current. A typical polarization P=0.56 is measured in permalloy. β is the degree of

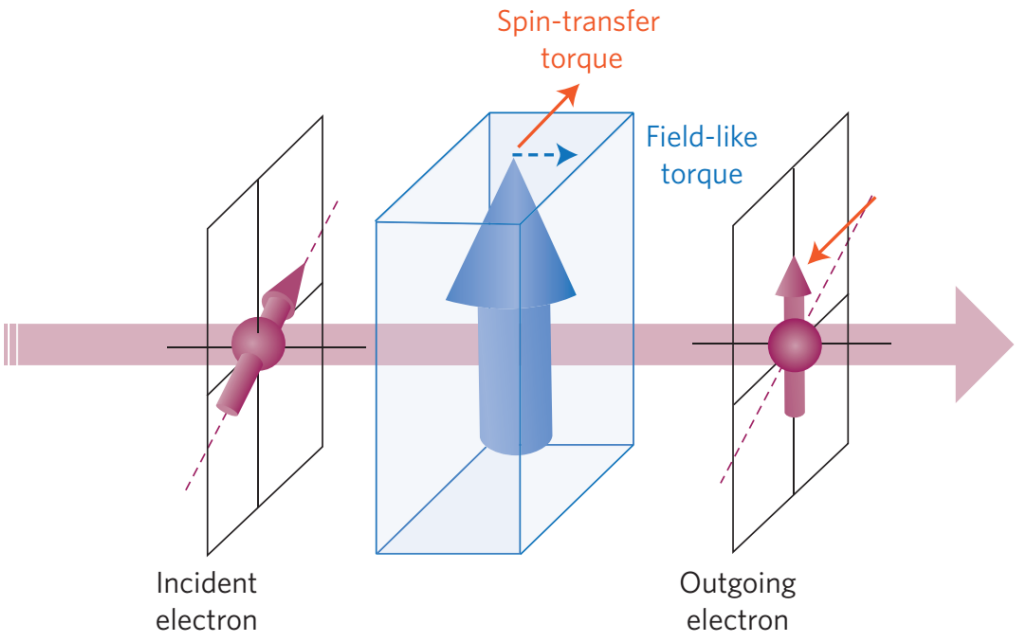

Fig. 2.8 Schematic of torques transferred to the magnetization (in blue Vertical arrow) by an incoming spin polarized electron. Due to interaction between the electron and moment, two types of torques are transfered to the magnetic moment. One is spin-transfer torque that lies in the same plane as the spin of the incident and outgoing electron. Other one is field-like torque lying perpendicular to that plane. Adapted from [43].

non-adiabaticity, a dimensionless parameter and depends on the material. The values of β is measured to be much smaller than unity and of the order of α [38, 44].

The physics behind how currents can generate torques to change the direction of magnetization can be illustrated with the help of figure 2.8. Here a spin polarized current carrying spin angular momentum interacts with the localized magnetic moment. As a result of the interaction, it transfers its momentum to the localized magnetic moment causing the momentum to change its direction and then gets transmitted or reflected losing some momentum. This interaction causes torques on the magnetic moment: one spin transfer torque (STT) that lies on the same plane as that of the incident electron and other field-like torque that lies perpendicular to the STT. The first one is also called as the in-plane or adiabatic spin -transfer torque or Slonczewski-like torque and the later is called as the perpendicular or non-adiabatic or field-like torque, as it acts on the magnetization like an external field. The direction of motion of the domain wall due to STT is along the direction of electron flow or opposite to the direction of current. Whether the explicit LLG or Gilbert form is used, also determines the form of the current driven equation [45].

On the other hand, in heterostructure materials having heavy metal on one or both sides of the ferromagnetic metal, another effect due to the spin dependent scattering of the charge current with the heavy metal needs to be taken into account. This effect is known as spin Hall effect [46]. The charge current flowing in the heavy metal experiences a scattering that produces a spin current in a direction perpendicular to the direction of current and to the interface. This spin current diffuses into the ferromagnetic layer and can transfer torque into the magnetic moments by spin transfer mechanism. Relevant torque terms can be added to the LLG equation to take spin Hall effect effect into account [47, 48].

2.6 Analytical model for DW dynamics

Phenomenological models of magnetization dynamics discussed before can tell us about the evolution of a DW by calculating how the individual moments evolve in the system. These calculations based on LLG equation is a computationally expensive process. However, analytical models for DW dynamics can give us this information in terms of set of equations that needs material properties as input. The most widely used analytical model for DW dynamics is known as the 1D model, developed first

by Walker in the 50's. He developed sets of equations that describes the motion of a Bloch wall in a nanowire. The Bloch wall was assumed to be a particle like zero dimensional object moving in a 1 dimensional nanowire under uniform magnetic field. Magnetization is assumed to be changed only along one direction. In the recent times, it has become a very useful tool for predicting the dynamics of DWs. 1D model predicts the motion of DWs in a nanowire in terms of a set of collective coordinates: domain wall position (q), internal magnetization angle (ϕ) and width (Δ).

In order to relate local magnetic moment with the collective coordinates, spherical coordinates of the magnetic moment can be written in terms of the collective coordinates using the profile of Bloch wall as an ansatz in the following form:

$$\theta(x,t) = 2\ atan\ \left[exp\ \left(\frac{x-q}{\Delta}\right)\right] \tag{2.35}$$

$$\varphi(x,t) = \phi \tag{2.36}$$

Here θ is the angle of magnetization with the positive z-axis and and ϕ is the angle of in-plane component of magnetization with the x-axis.

Magnetization obeys the classical Euler equations of motion:

$$\frac{\partial L}{\partial \dot{X}} - \frac{d}{dt}\left(\frac{\partial L}{\partial \dot{X}}\right) = 0 \tag{2.37}$$

where X is any collective coordinate : q, ϕ or Δ. L is the Lagrangian of the system and is written in the following form [49]:

$$L = \int E + \frac{M}{\gamma}\ \dot{\varphi}\ cos\theta \tag{2.38}$$

This equation assumes no loss of energy and describes the precessional motion of the magnetic moment. Therefore, in order to take into account the damping, frictional forces is added into equation 2.37 in terms of Rayleigh dissipation function,R:

$$\frac{\partial L}{\partial X} - \frac{d}{dt}\left(\frac{\partial L}{\partial \dot{X}}\right) + \frac{\partial R}{\partial \dot{X}} = 0 \tag{2.39}$$

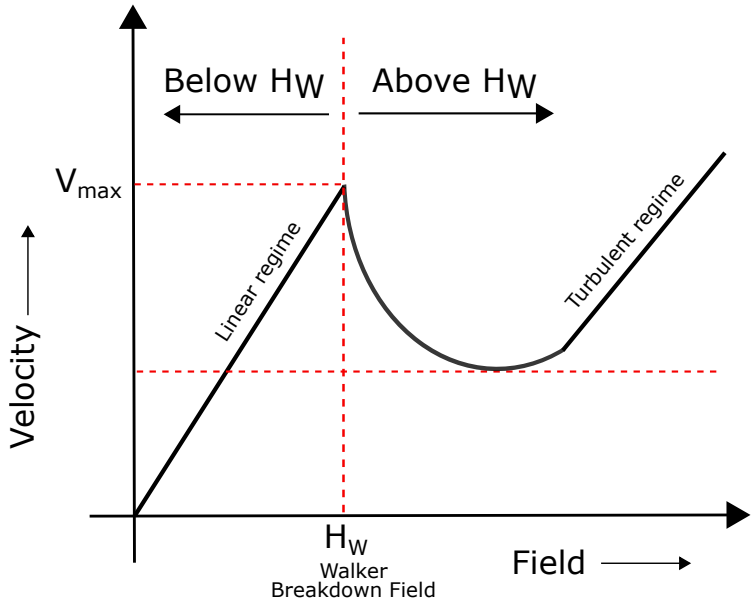

Fig. 2.9 Different regimes of the DW motion based on the prediction of 1D model.

This is the Euler-Lagrange-Rayleigh equation of motion for a magnetic system. The Rayleigh function is given by [50, 51]:

$$R = \left(\frac{\alpha\, M_s}{2\gamma}\right) \int \dot{\theta}^2 + \dot{\varphi}^2 sin^2\theta \tag{2.40}$$

It considers the rate of change of magnetic moment which is equivalent to particle velocity in classical mechanics.

Calculating L and R and then from equation 2.39, we can derive the following equations:

$$\dot{\phi} + \frac{\alpha}{\Delta}\dot{q} = \gamma H \tag{2.41}$$

$$\frac{\dot{q}}{\Delta} - \alpha\dot{\phi} = \gamma H_K \sin\phi\ \cos\phi \tag{2.42}$$

$$\dot{\Delta} = \left(\frac{12\gamma}{\alpha M_s \pi^2}\right)\ \left[\frac{A}{\Delta} - \left(K_0 + K\sin^2\phi\right)\Delta\right] \tag{2.43}$$

These set of equations represent 1D model of DW dynamics. By solving these equations evolution of parameters such as position, width and magnetization angles of DWs can be obtained. Predictions of the velocity of a DW based on above equations

is presented in figure 2.9. It predicts two regimes of DW motion: steady flow and precessional flow. Steady flow is below the field called walker field ($H_W = \frac{\alpha}{2} H_K$). In this regime, DW velocity is given by the expression:

$$v(t) = \frac{\gamma_0 \Delta^*(\phi^*)}{\alpha} H \tag{2.44}$$

where ϕ^* is the equilibrium value of ϕ, given by:

$$\phi^* = \frac{1}{2}\, sin^{-1}\left(\frac{H}{H_W}\right) \tag{2.45}$$

and Δ^* is the equilibrium value of the width after relaxation, given by:

$$\Delta^*(\phi) = \sqrt{\frac{A}{K_0 + K\, sin^2\phi}} \tag{2.46}$$

Maximum velocity reached in this regime is:

$$v_{max} = \frac{\gamma_0 \Delta}{\alpha} H_W \tag{2.47}$$

Above Walker breakdown, a sharp drop in velocity occurs and DW reaches a turbulent regime where the magnetization precesses around the field continuously and velocity of the DW oscillates between positive and negative values.

2.7 DW dynamics in disordered media

Other than LLG equations for magnetization dynamics and 1D model for motion of domain walls, there is another relevant phenomenological theory called 'creep theory' that describes the motion of DWs under external force when material inhomogeneity and temperature are present. In this section, we present a general review of this theory. This theory can, in principle, be applied to many other physical systems e.g. ferroelectric domain walls, earth quakes, fractures, contact lines in wetting etc. It has become excellently successful in predicting the motion of DWs for ferromagnetic material systems compared to other systems.

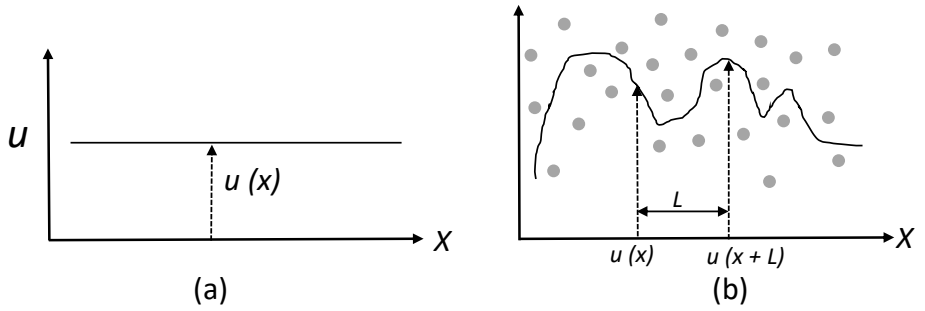

Fig. 2.10 Schematic of displacement of an elastic interface without pinning points (a) and in the presence of pinning points (b). Pinning points, represented with grey solid circles, cause the interface to become rough.

Let us consider a system with an elastic interface of length L with randomly distributed disorder or pinning points as shown in figure 2.10. In this figure two scenarios: one without pinning points or disorder and the other with pinning points are shown. When no pinning points are present, the interface maintains a flat configuration, while in the presence of pinning points it roughens. Now, let us assume that average pinning strength of the pinning points are f_{pin} and number of pinning points per unit of surface area is n_i. Let ξ be the characteristic length over which a pinning point can influence the interface with its pinning force. Then the area over which pinning points influencing the interface lies is ξL. By multiplying density of pinning points with this area, we get the number of pinning points influencing the interface equal to $n_i \xi L$. Therefore, we will get the pinning forces for weak pinning points as :

$$F_{pin} = f_{pin} \left(n_i \xi L\right)^{\frac{1}{2}} \tag{2.48}$$

Consequently, the pinning energy due to this pinning force can be written as:

$$\varepsilon_{pin} = \left(f_{pin}^2 n_i \xi L\right)^{\frac{1}{2}} \xi \tag{2.49}$$

Pinning forces can cause bending of the interface around the pinning point. However this results in increase in length of the interface and therefore also an increase elastic energy. The expression for elastic energy due to a deformation u as a function of x as shown in figure 2.10 can be written as:

$$\varepsilon_{el} = \int_0^L \frac{E_{el}}{2} \left(\frac{\partial u}{\partial x}\right)^2 dx \approx E_{el} \left(\frac{\xi^2}{L}\right) \tag{2.50}$$

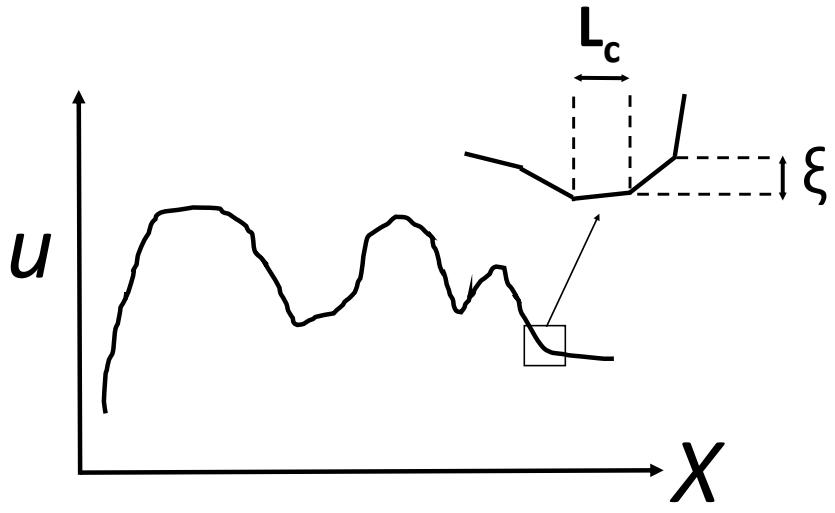

Fig. 2.11 Schematic of Larkin length L_c and parameter ξ of an elastic interface. The interface can be considered consisting of small segments of length L_c

where E_{el} is the elastic energy of the domain wall. For a Bloch wall in the absence of a driving field, it gets contribution from exchange and anisotropy energy and becomes equal to $4\sqrt{AK}$. From equation 2.49 and equation 2.50, we see that pinning energy scales with L as $L^{\frac{1}{2}}$ and elastic energy as $\frac{1}{L}$. Therefore for very small lengths elastic energy dominates and interface always remains flat. But above a critical length L_c, pinning energy can dominate and cause bending of the interface. This critical length L_c, the Larkin length occurs when the pinning energy equilibrates the elastic one. Thus by equating pinning energy with elastic one and replacing L for L_c we can get the expression for L_c as:

$$L_c = \left(\frac{E_{el}^2 \xi^2}{4\gamma_{pin}}\right)^{\frac{1}{3}} \tag{2.51}$$

where $\gamma_{pin} = f_{pin}^2 n_i \xi$. Schematic of Larkin length and parameter ξ is shown in figure 2.11. The interface can be viewed as consisting of number of small segments of length L_c. Over this length L_c, displacement u of interface changes by ξ.

Pinning energy corresponding to the length L_c is called as scaling energy constant (U_c) and is given by:

$$U_c = \left(E_{el} \xi^4 \gamma_{pin}\right)^{\frac{1}{3}} \tag{2.52}$$

Other than L_c and U_c, another parameter of interest is depinning field, denoted by H_{dep}. It is the external force or field, that has to be applied in order to overcome the pinning force. By equating pinning energy with Zeeman energy $M_s H d_{film} L\Delta$ where d_{film} is the film thickness, we get:

$$H_{dep} = \frac{E_{el}\xi}{M_s\ d_{film}\ L_c^2} \tag{2.53}$$

Below depinning field no motion of interface take place at zero temperature. It is shown in figure 4.5(b). However, when there is non-zero temperature, motion of domain wall takes place due to thermally activated jumps even below depinning field. This situation when $T > 0$ and applied field $H << H_{dep}$ is called as creep regime of DW motion. In this regime, thermally activated jumps between spatially separated metastable states takes place. An energy barrier exists between two metastable states and there is a characteristic length for which this energy barrier is minimum. This length is denoted as L_{opt} and it represents the optimal size of the thermally activated jump that the DW has to overcome in order to find a new metastable state with lower energy. It is schematically shown in figure 4.5 and it can be expressed as:

$$L_{opt} \ \sim \ L_c \left(\frac{H_{dep}}{H}\right)^{\frac{1}{2-\zeta}} \tag{2.54}$$

where (ζ) is called as the roughness of the interface. It is one important property of the interface and is a direct result of interaction of the interface with pinning points. It is calculated from spatial averaging of a correlation function that finds correlation between displacement of two different points of the interface separated by a distance L (figure 2.10(b)) in the following way:

$$< [u(x+L)^2 - u(x)^2] > \ \sim \ \left(\frac{L}{L_c}\right)^{2\zeta} \tag{2.55}$$

The value of ζ depends on the dimensionality of motion of the interface, denoted by n. In a 2D film, an one dimensional interface $(D = 1)$ is restricted to move only along one direction. Therefore,dimensionality of the motion of interface in our case is 1 and for $n = 1$, we get $\zeta = 2/3$.

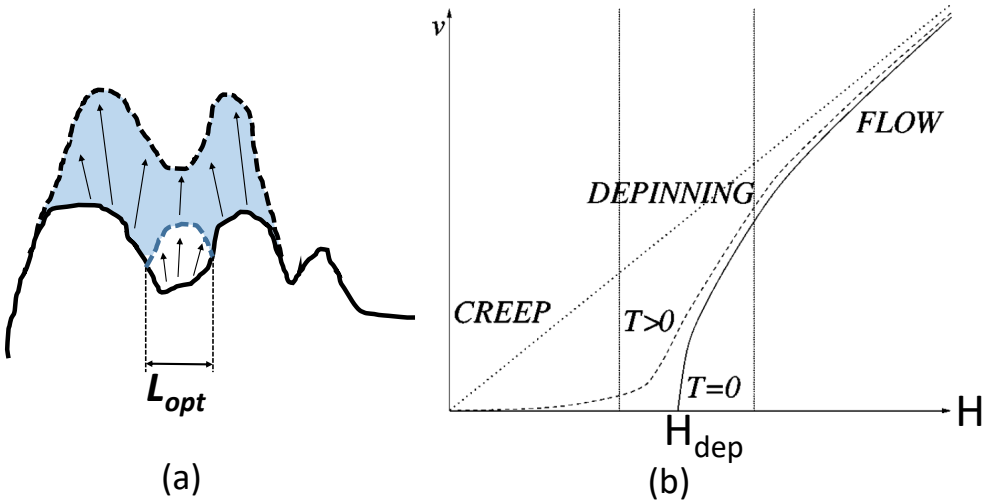

Fig. 2.12 (a) Schematic of thermally activated jump and characteristic length L_{opt} of DW, (b) theoretical prediction of the DW velocity (v) vs. force characteristic curve considering DW as an elastic interface moving in a weakly disordered medium at T=0 (solid line) and at T>0 (dashed line). Dashed linearly proportional line represents the velocity for a pure medium. Taken from [52].

For this thermally activated DW motion, velocity of DW can be expressed in terms of the energy barrier by the following Arrhenius-like equation:

$$v_{creep} = v_0 \, exp\left[-\frac{U}{k_B T}\right] \tag{2.56}$$

where, U is the energy barrier that the DW needs to overcome at temperature T and v_0 is the pre-exponential factor related to attempt frequency. Energy barrier U depends on the interface properties and the properties of disorders in material. It is also a function of applied field (H) and is given by:

$$U(H) = U_c \left(\frac{H_{dep}}{H}\right)^{\mu} \tag{2.57}$$

Here $\mu = \frac{D-2+2\zeta}{2-\zeta}$ with D being called as the dimensionality. DW in an ultra-thin perpendicular ferromagnetic film, as in the case of this thesis, can be treated as an one dimensional elastic interface $(D = 1)$ if we assume that its width is uniform and film is thin enough for its magnetization not to vary along the direction of film

normal. If the film is not thin enough, then $D = 2$ for DWs in thick magnetic film. For $D = 1$ and $\zeta = 2/3$, we get $\mu = 1/4$.

Therefore, from equation 2.56 and equation 2.57 we get the velocity of DW in the creep regime as:

$$v_{creep} = v_0 \, exp \left[-\frac{U_c}{k_B T} \left(\frac{H}{H_{dep}} \right)^{-\frac{1}{4}} \right] \tag{2.58}$$

Chapter 3

Methods

In this chapter, methods used for the experiments as well as for the micromagnetic simulations presented in this thesis will be discussed. In the experimental part, growth of the magnetic thin films, irradiation, magneto optical Kerr microscopy and image analysis software will be discussed. In the micromagnetic simulation part, underlying methods for micromagnetic simulations are discussed.

3.1 Experimental

In chapter 4, we present the study of local dynamics of domain walls in Si/SiO_2/Ta (5nm)/$Co_{20}Fe_{60}B_{20}$ (1nm)/MgO (2nm)/Ta (3nm) ultra-thin films. Three samples are deposited by magnetron sputtering and then they are annealed at 300 °C for one hour. All the samples exhibit perpendicular magnetic anisotropy. The magnetic properties of these materials are discussed in chapter 4. Two samples are then irradiated with He^+ ion with fluences of $8x10^{18}$ and $16x10^{18}$ He^+/m^2. The effect of irradiation on the magnetic properties as well as on domain wall dynamics will be discussed in chapter 4.

The experiments were conducted first by saturating the magnetization of the sample in one direction and then nucleating a magnetic bubble domain by applying pulses of magnetic field in the opposite direction. Growth of the bubble domain under the application of a constant out-of-plane field is captured using a wide field Kerr microscope in polar configuration. The images of expanding magnetic bubbles

at consecutive time steps were then processed using a python code developed in our group.

3.1.1 Growth of the magnetic thin films

DC magnetron sputtering was used in order to deposit the Si/SiO_2/Ta/CoFeB/MgO/Ta magnetic samples. Sputtering is the most widely used deposition technique for ultra-thin magnetic films such as Ta/CoFeB/MgO or Pt/Co/Pt. The sputtering chamber consists of a cathode (negatively polarized) and anode (positively polarized) in a high vacuum system (1x10^{-4} Pa or lower). Argon gas is introduced inside the vacuum chamber under application of an electric field. Due to the application of the electric field, electrons are accelerated from the cathode towards the anode. In this process, electrons collide with the Ar gas atoms and due to these collisions, electrons knock-out one electron from the Ar atom, causing Ar atoms to get ionized and positively charged. These positively charged Ar^+ ions move towards the cathode. In the cathode, the target material plate is placed. Ar^+ ions bombard the target atoms, transfer momentum to these atoms and knock them out. With the momentum received from Ar^+ ions, target atoms move towards the substrate, get deposited leading slowly to nucleation and film formation. In magnetron sputtering, secondary electrons emitted because of the collision between Ar^+ ions and target material are used more efficiently by applying a magnetic field. This magnetic field traps the secondary electrons for longer time leading to a more efficient bombardment of the target atoms. Depending on the power supply, there are two kinds of magnetron sputtering: DC and RF (radio frequency). DC magnetron sputtering is usually used for metal thin films, while RF sputtering is used for thick and non-conducting films.

The CoFeB samples studied in this thesis were deposited using a DC magnetron sputtering Singulus ROTARIS system. During my secondment at Singulus Technologies, I had the opportunity to understand the deposition of these films in the system.

3.1.2 Characterizations of the magnetic thin films

After deposition a thorough structural and magnetic characterization needs to be carried out to probe its properties. Sometimes it is done in-situ during the deposition

as well. Below some important characterization techniques relevant for CoFeB PMA material used in this thesis are discussed.

Structural characterizations

X-ray diffraction

X-ray diffraction (XRD) is a non-destructive technique that can be used to know whether the film is crystalline or amorphous, if crystalline, then crystallographic informations such as crystal structure of the film, spacing between crystal planes, epitaxial or polycrystalline, if polycrystalline then grain size etc. It works by letting a monochromatic beam of x-rays to incident on the sample at an angle θ between the x-ray and the sample plane and measuring the intensity of diffracted beams using a scintillator type detector at an angle 2θ between the incident x-ray and detector. According to Brag's law of diffraction, a constructive interference between the diffracted beams takes place when the path difference between two diffracted beams is equal to an integral multiple of wavelength of the x-rays, or the condition $n\lambda = 2d\sin\theta$ is satisfied. Here n is the order of diffraction, λ is the x-ray wavelength (often $\mathrm{Cu}_{K\alpha} = 0.154\ nm$), d is the distance between planes and θ is the angle of incidence of x-rays. When a specular scan is done by varying θ and maintaining the x-ray and detector coupled at $\theta - 2\theta$, peaks appear at particular angles in the intensity of diffracted beams vs. θ plot and by knowing the angle at which the peaks appear, distance between the crystallographic planes and its crystal structure can be known.

X-ray reflectivity

X-ray reflectivity (XRR) is a technique similar to XRD in the way the measurement is carried out with the difference that in XRR the angle of incidence (θ) is small ($<15^\circ$) while XRD is carried out for larger angles. XRR is relevant to this thesis as it can be used to measure interfacial thickness (e.g. thickness of the Ta/CoFeB interface in Ta/CoFeB/MgO material), layer thickness as well as electron density. It can also be used to calibrate the growth rate of sputter systems.

An XRR measurement is shown in figure 3.1 where intensity of reflected beam of x-rays incident on a Ta(5 nm)/CoFeB(1nm)/MgO(2 nm) sample is measured as a function of the incident angle (θ). When the incident angle is larger than θ_c, the critical angle below which total internal reflection takes place, reflections from different interfaces of the sample results in interference fringes. The period of

interference fringes is determined by the thickness of each layer. A more rapidly reduced intensity with increasing reflecting angle is observed because of the diffuse scattering resulting from surface and interface roughness. An equation for calculating the layer thickness is given by T.C. Huang et al. [53]:

$$m\lambda = 2\,t\,\sqrt{sin^2\theta_i - \theta_c^2} \tag{3.1}$$

where m is the order of the reflected fringe, θ_i is the angle at which the fringe appears and t is the layer thickness. However, the parameters such as thickness of the interface, thickness of the layers and electron density can be extracted from the measurement data by fitting it with MAUD software [54]. The software works by describing the sample as a set of physical characteristics and using them to fit a set of reflectivity spectra obtained at different positions of the sample.

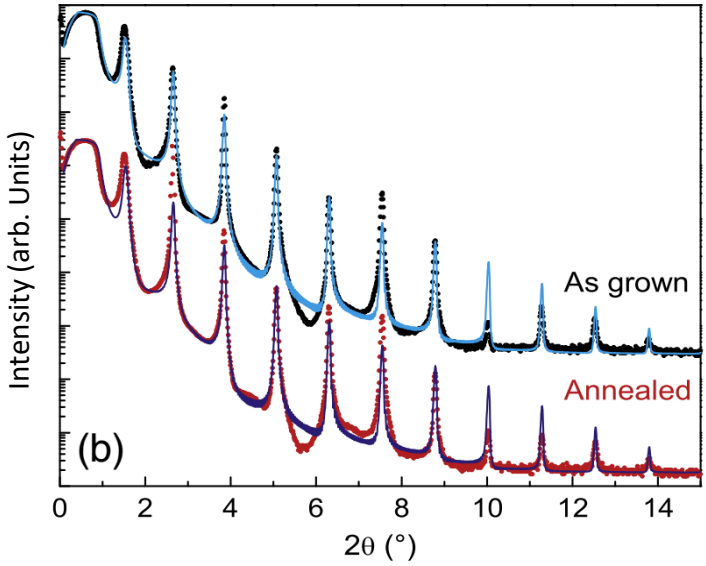

Fig. 3.1 An example of X-ray reflectivity (XRR) measurements (dots) and fitting (line) of a Ta (5 nm) /CoFeB(1 nm)/MgO trilayer period as-grown and annealed samples grown upon Si/SiO_2 substrates by sputtering. Cu K_α with wavelength 0.154 nm was used as the x-ray source. Taken from [55].

Magnetic characterizations

Vibrating sample magnetometer

Vibrating sample magnetometer (VSM) is a common technique used to measure the magnetization of a sample at a given applied field. Here the sample is placed

in a homogeneous magnetic field and vibrated near pick-up coils, where a voltage is generated because of the changing flux. From this voltage, magnetization in the sample can be measured. Additionally magnetic field, along the plane of the sample (hard axis) or perpendicular to the sample (easy axis), can be changed from high positive to high negative and then back to high positive to measure the hard axis or easy axis hysteresis loop. Magnetic properties such as saturation magnetization (M_s) and anisotropy field (H_K) can be obtained from these hysteresis loops.

SQUID magnetometer

A superconducting Quantum Interference Device (SQUID) magnetometer is one of the most sensitive magnetic field measuring instruments. In order to measure magnetic moment thousand times smaller than VSM $\approx 10^{-12}\ Am^2$, a SQUID is used. The magnetic properties that are measured from SQUID are the same as in VSM. The role of SQUID is to work as the detector that consists of closed superconducting loop with one (Radio frequency (RF) SQUID) or two (Direct current (DC) SQUID) Josephson junctions. Because of the highly non-linear I-V characteristic of the Josephson junction and the quantized nature of the magnetic flux through it, SQUID offers extreme sensitivity.

In the SQUID magnetometer, the SQUID is connected via superconducting wires to a system of detection coils that are also superconducting in nature. Similar to VSM, when the sample is moved through the detection coil , it causes a change in magnetic flux. This change in magnetic flux induces a change in the persistent current flowing across the superconducting loop as well as the SQUID. Then the magnetic moment of the sample can be determined by measuring the change in SQUID output voltage. In order to protect the measurement from small fluctuation in the ambient magnetic field or magnetic field generated because of the superconducting magnet, the SQUID is placed in a region of small and homogeneous magnetic field confined inside a superconducting shield and the detection coils are shaped in a particular geometry which contains three equally spaced, but outer ones winding clockwise in a single turn and middle one winding anticlockwise in a double turn.

3.1.3 Irradiation of the thin film with He^+ ion

Some of the Ta/CoFeB/MgO samples after deposition and annealing are irradiated with He^+ ions to cause interfacial mixing of atoms using an ion implanter schemati-

cally shown in Figure 3.2. He^+ ions were specially used, because they were shown to be efficient in mixing the atoms of the target sample despite their small mass [56]. An ion implanter is equipped with a universal ion source (S in figure 3.2), which is a hot cathode source where practically all elements, gas or solid, can be ionized. After ionization He^+ ions are accelerated and pass through a mass separator. Then they are focused by quadrupole lenses and the beam is made to enter an electrostatic XY scanner. This scanner applies a positive DC voltage in order to deflect the ions approximately by 5°, so that only the He^+ ions and not the neutral atoms enter the target chamber. In the target chamber, the sample to be irradiated is placed. The energy of the He^+ ions is chosen based on previous studies [57–59] in such a way that the ions stop at the surface of the sample. These energetic ions causes displacement of the atoms inside the sample. The factor that limits the current of the ions is the heating of the sample. An excessive current of He^+ ion can cause heating of the sample. Therefore, the current of He^+ ions has to be kept below a critical value so that the temperature of the sample is low enough for long range relaxation of the atoms or bulk diffusion by annealing to take place.

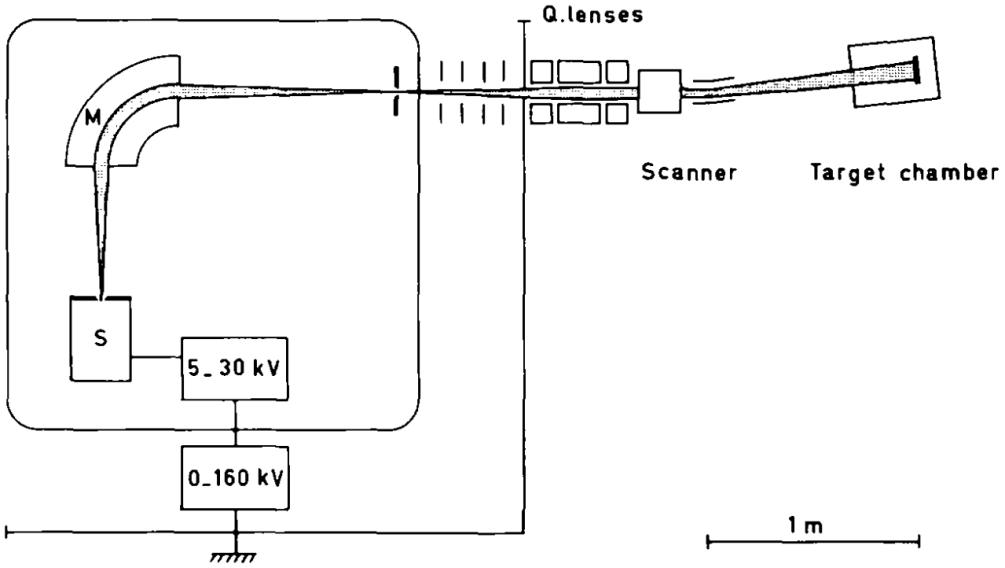

Fig. 3.2 Schematic of an ion implanter used for irradiating Ta/CoFeB/MgO samples. Adapted from [60].

3.1.4 Magneto optical Kerr microscopy

One of the goal of this thesis is to experimentally study the local dynamics of magnetic domain walls. For this we need to be able to visualize the motion of the domain walls. There are different techniques by which magnetic domains or the boundary between two domains can be detected. Some of them are: magneto optical methods, transmission electron microscopy, electron reflection and scattering methods, x-ray and neutron methods. Magneto-optical methods, being relatively simple, are widely used. In this thesis, we use a magneto-optical Kerr effect (MOKE) microscope to observe and record the motion of domain walls. What follows is the discussion of physics behind this method and the instrumental details of the microscope used in our work.

MOKE microscopy is a powerful and versatile technique to observe statics as well as dynamics of magnetic domains at the micrometer scale. It was discovered by Michael Faraday in 1845 that plane of polarization of light undergoes a rotation after transmission through a magnetized sample. Later in 1877 it was discovered by Kerr that, not only through transmission, but also after reflection from the surface of a magnetic sample, light undergoes a rotation of its plane of polarization. These two effects are known as Faraday effect and Kerr effect respectively. Faraday effect , being reliant on transmission,can be used only for samples that are transparent to light, such as yttrium-iron-garnet (YIG). In this thesis, we exploit Kerr effect for studying domain walls and their dynamics in CoFeB ultra-thin films.

Magneto-optical Kerr effect has its origin in the spin-orbit interaction. When linearly polarized light, that can be regarded as the linear superposition of right handed and left handed circularly polarized light, is incident on the magnetic material, light interacts with the conduction electrons of the magnetic metal and causes a rotation of the electrons providing them with orbital angular momentum. This momentum is equal in magnitude and opposite in direction depending on the right or left sense of the polarized light. Moreover, light being an electromagnetic wave, it contains a magnetic field and an electric field perpendicular to each other. A magnetic field makes the magnetization align along the direction of the field. The field of the polarized light, depending on its direction modifies the energy of the magnetization due to spin-orbit interactions. Because of this energy modifications, the refractive index of the magnetic material is modified. In other words, the right handed and left handed circularly polarized light experience different refractive

index in the magnetized material, a phenomenon known as circular birefringence (i.e. birefringence of circularly polarized light). This makes the right and left circularly polarized light to travel with different velocities and therefore, have a phase delay after they are reflected. After reflection they emerge as an elliptically polarized light with its plane of polarization rotated. This light is then sent through a polarizer, called as analyzer. The analyzer rotates the plane of polarization further by 90°. When the polarizer and analyzer axis are 90° apart (extinction condition), the intensity of the light is negligible. However, interaction of the light with magnetized sample makes the plane of polarization to rotate by some angle and because of this the angle between polarizer and analyzer is not 90°. After the analyzer, light goes into a detector transforming rotation of the plane of polarization into contrast of the magnetic domain. Rotation of the plane of polarization is directly proportional to the magnitude of the local magnetization of the material, and therefore the rotation or the contrast can be used to probe magnetic properties of the materials as well. This rotation also depends on the direction of the magnetization, thus allowing us to differentiate between different domains and the boundary between them.

MOKE microscope is used in different geometric configurations depending on the angle between incident light and the direction of magnetization as shown in Figure 3.3. In polar MOKE configuration, magnetization is perpendicular to the plane of the sample and light is incident at a close to zero incident angle. Polar configuration is suitable for perpendicular anisotropy materials and therefore, we use it for the work in this thesis. For in-plane materials two configurations, longitudinal and transverse, are used. In longitudinal configuration the magnetization is parallel to the sample plane, but in this case the incident angle of light is non-zero. Non-zero incident angle is required in longitudinal configuration for the wave vector of light to have some component along the direction of magnetization. However, transverse configuration is different from these two configurations. In the transverse case, magnetization is parallel to the sample plane, but perpendicular to the plane of incident light so that it has no-component of its wave vector along the magnetization. After reflection, the plane of polarization of light does not rotate and it remains linearly polarized in stead of elliptical polarization in other two cases. The contrast between two domains here is obtained due to the magnetization direction dependent reflectivity of the sample, which results in a change of intensity.

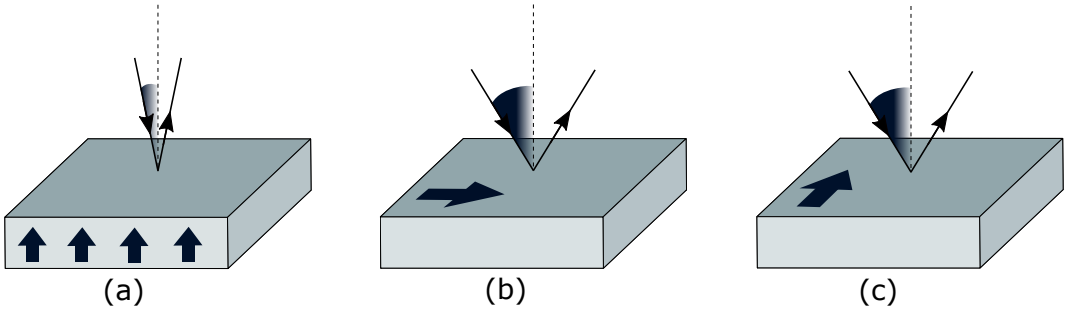

Fig. 3.3 Schematic of different MOKE configurations: (a) polar, (b) longitudinal and (c) transverse.

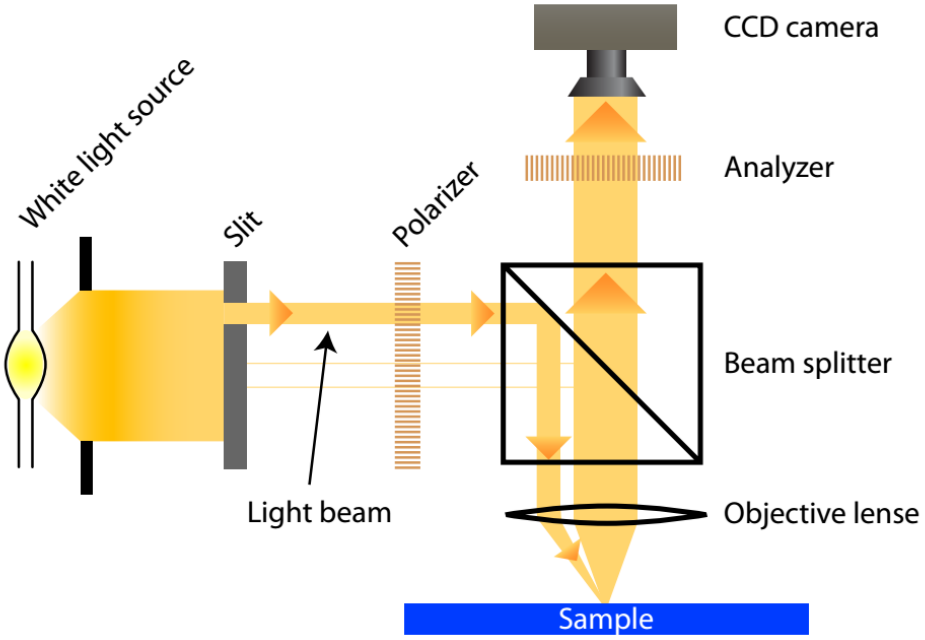

Fig. 3.4 Schematic of MOKE microscope. Adapted from [61].

In our experiments, a MOKE microscope developed and produced by Zeiss (Zeiss AXIOSKOP 2 Plus) equipped with a polarizer-analyzer configuration is used. A schematic of the set-up is shown in figure 3.4. White light produced by arc Hg lamp is used to illuminate the sample. Before reaching the sample, light from the lamp goes through a pinhole or slit (300 μm in diameter) producing a narrow beam of light.Then it goes through the polarizer (Glan-Thompson polarizer) producing linearly polarized light. It is reflected by a beam splitter and focuses onto the sample with an objective lens. After being reflected by the sample surface, it goes through

the objective lens, beam splitter and analyzer to reach the CCD camera, where the image is captured.

3.1.5 Image analysis software

After dynamics of domain walls are captured using a CCD camera integrated with the MOKE microscope, videos are processed using a python based image processing code developed in our group. I learnt to use this code, that can give contours of the bubble domains at each frame as an output. This information can then be further analyzed to calculate various relevant statistical quantities of interest. Below how the code works is explained.

In order to obtain contours of domain walls at each frame from the video, images are first stacked in a 3 dimensional way as shown in figure 3.5 (left). Then a Gaussian filter is applied along spatial as well as temporal axis to smoothen the frames. Each pixel has a gray value as a function of frame number or time.

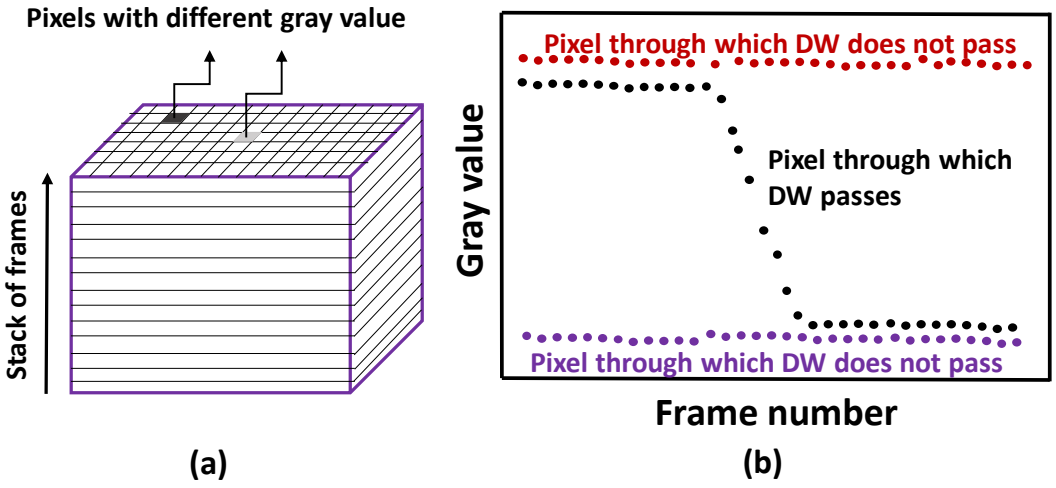

Fig. 3.5 Schematic of (a) image stack and (b) change in the gray value as a function of frame number representing three pixels: red and blue through which DW does not pass and black through which DW passes.

In figure 3.5(b), change in gray value of three pixels is schematically shown. If the domain wall does not pass through the pixel (represented in red and blue), then the gray value of the pixel remains constant. Magnitude of gray value depends on the magnetization direction in that pixel. However, if the domain wall passes through

the pixel, then a gradual change from a high to low value takes place. We want to know the precise frame in the region of gradual change where switching of the pixel takes place.

For finding the frame at which the pixel switches, cross correlation of the gray value function with a step function is an useful tool. Cross correlation between two continuous functions $f(t)$ and $g(t)$ is given as:

$$(f \star g)(\tau) = \int f(t)\, g(t+\tau)\, dt \tag{3.2}$$

Cross correlation is a function of the displacement τ and the value of cross correlation $(f \star g)$ is maximum when the two functions are most similar. In our case, $f(t)$ is the gray value function and g(t) is the step function. The step function is displaced along the time axis, cross correlation is calculated and it can tell us the value of the displacement for which the gray value function is most similar to the step function. For discrete functions, like in our case, the cross correlation function takes the following form:

$$(f \star g)\,[n] = \sum_i f[\,t_i\,]\, g[\,t_i + n\,] \tag{3.3}$$

where, t_i are discrete times and n is the displacement of the step function along the time axis. We consider the following step function:

$$g(t_i) = \begin{cases} +1 & t_i < t_0 \\ -1 & t_i > t_0 \end{cases} \tag{3.4}$$

Therefore, we get the following cross-correlation function:

$$(f \star g\,) = \sum_{t_i < t_0} f(t_i) - \sum_{t_i > t_0} f(t_i) \tag{3.5}$$

By dividing each side of the above equation with N, the number of points on each segment of the step function:

$$\frac{(f \star g\,)}{N} = \frac{\sum_{t_i < t_0} f(t_i)}{N} - \frac{\sum_{t_i > t_0} f(t_i)}{N} \tag{3.6}$$

The above quantity is calculated varying t_0. The value of t_0 at which this quantity is maximum is taken as the time at which the switching takes place. In our analysis, N is assigned the value of 10.

3.2 Micromagnetic Simulation

In chapter 5, we present the study of field driven dynamics of magnetic bubble domains. The mathematical tool to study the dynamics of magnetization is the Landau-Lifshitz-Gilbert equation (2.32). In the previous chapter, we discussed that micromagnetic theory is based on the continuum approximation of the magnetization in space. However, in order to study the dynamics of magnetization using the Landau-Lifshitz-Gilbert equation with continuum approximation, one has to find an analytical solution for this equation. Analytical solutions for this equation are found only for simple cases, thus limiting the simulations for complex micromagnetic problem. However, with the rapid progress in computing technology, it has become possible to solve the LLG equation numerically. LLG equation can be solved numerically using micromagnetic 2D simulations with the GPU-accelerated micromagnetic code Mumax^3 [62–64]. In the following paragraphs, details of the simulation using Mumax micromagnetic code is explained.

In order to solve the LLG equation, simulation space is first divided into smaller homogeneous rectangular cuboids, a method known as finite difference method. Magnetization inside each cuboid or cell is assumed to be uniform. It is called as the reduced magnetization and is given by $\mathbf{m} = \frac{\mathbf{M}}{\mathbf{M}_s}$ with $|\mathbf{m}| = 1$, i.e. only direction of $\mathbf{m}$ changes inside one cell during dynamics. The size of cells have to be smaller than the exchange length (l_{ex}), the length scale over which the magnetization changes significantly, expressed as:

$$l_{ex} = \sqrt{\frac{2A}{\mu_0 M_s^2}} \tag{3.7}$$

After the discretization of the simulation space, next step is to solve the LLG equation. Computationally challenging part here is to calculate the effective field ($\mathbf{H}_{eff}$), that appears on the right hand side of the equation. Local terms of the effective field, i.e. those terms that doesn't depend on the magnetizations in cells that are far away, such as anisotropy and applied field are straightforward to calculate.

Spatial derivatives of the magnetization, needed for calculating contribution of exchange or Dzyalloshinskii-Moriya interaction to $\mathbf{H}_{eff}$ are approximated using central derivatives based on a second-order Taylor expansion. The expressions for first and second derivative of an arbitrary function f are:

$$f_i^{'} = \frac{f_{i+1} - f_{i-1}}{2h} \tag{3.8}$$

$$f_i^{''} = \frac{f_{i+1} - 2f_i + f_{i-1}}{h^2} \tag{3.9}$$

where i is the cell center where the derivative needs to be calculated and h is cell spacing.

Magnetostatic field in a cell, being a long range interaction, depends on the magnetization inside all other cells. The average self-magnetostatic field at cell i can be calculated as:

$$\mathbf{H}_{d,i} = -M_s \sum_j \mathbf{N}(\mathbf{r}_i - \mathbf{r}_j) \cdot \mathbf{m}_j \tag{3.10}$$

where summation is over all cells, $\mathbf{r}_i$ or $\mathbf{r}_j$ is the position vector of i or j cell respectively, $\mathbf{N}(\mathbf{r}_i$ - $\mathbf{r}_j)$ is the symmetric demagnetizing tensor given by:

$$\mathbf{N}(\mathbf{r}_i - \mathbf{r}_j) = \frac{1}{4\pi} \oint_{S_i} \oint_{S_j} \frac{d\mathbf{S}_i \, d\mathbf{S}_j^{'}}{|r - r'|} \tag{3.11}$$

S_i and S_j are the surface of cell i and j and $\mathbf{S}_i$=S_i $\mathbf{n}$ and $\mathbf{S}_j^{'}$=S_j $\mathbf{n}^{'}$ are the surface vectors of the corresponding cells. Calculation of $\mathbf{H}_d$ at one cell requires the summation over all N number of cells. Therefore calculation of $\mathbf{H}_d$ for the whole simulation space needs $O(N^2)$ operations, while it is only $O(N)$ for local contributions of the effective field. Therefore, calculation of $\mathbf{H}_d$ is the most time consuming part of micromagnetic simulations. Thus, direct computation of $\mathbf{H}_d$ using the above equations (3.10 and 3.11) become notoriously challenging for large systems. Lots of efforts have been spent in the past in developing methods to estimate the magnetostatic fields efficiently. It was found that $\mathbf{H}_d$ can be calculated more efficiently by Fast Fourier Transform (FFT) techniques, because $\mathbf{H}_d$ can be recognized as a discreet convolution of $\mathbf{N}$ with $\mathbf{m}$. The techniques involve FFT of $\mathbf{N}$ and $\mathbf{m}$, multiplying their Fourier images locally in the reciprocal space and then taking the inverse FFT to obtain $\mathbf{H}_d$ in the forward space. The computation of $\mathbf{H}_d$ can

be performed in $O(N\ log\ N)$ operations, since FFT can be evaluated in $O(N\ log\ N)$ operation, in contrast to $O(N^2)$ operations needed for direct computation resulting from equation 3.10.

Time integration of the LLG is performed using explicit Runge-Kutta (RK45, the Dormand-Prince method [63]) methods. Adaptive time-step control is used in order to keep the error per step close to a preset value by adapting the time-step. Most of the calculations are performed on NVIDIA graphics processing Units (GPUs), that enables faster and larger scale simulations by massive parallelization of standard micromagnetic code. Parallelization in Mumax^3 is achieved using Go and CUDA.

One important aspect of simulating the dynamics of bubble domain is the different boundary conditions that can be applied, with each having its own merits or demerits. In figure 3.6, schematics of the different boundary conditions are presented. In open boundary conditions, effects due to the edges of the film becomes important when the bubble reaches the boundary. This condition works fine when our magnetic object of interest remains far away from the edges. On the other hand, in periodic boundary conditions, which are often used for approximating an infinite (large) system as in figure 3.6 by repeating the original simulation space, influences the dynamics of the bubble because of its interaction with the nearby bubble, even though it overcomes the disadvantage of open boundary condition. In order to overcome the limitations of open as well as periodic boundary conditions in our simulations, an infinite system is mimicked by adding dipolar energy generated from outside the simulated square as shown in figure 3.6(c).

In our study, we have a system of 1024 x 1024 x 1 rectangular cells of size 2 nm x 2 nm x 0.6 nm, as schematically shown in Figure 3.7. As a rule of thumb, the number of cells used are of the form 2^l x 2^m x 2^n where, l, m and n are positive integers.

Our simulation system mimics a Pt/$Co_{90}Fe_{10}$/Pt [65] ultra-thin square film of 2 x 2 μm^2, with material constants of saturation magnetization $M_s = 1353\ kA/m$, perpendicular magnetic anisotropy $K_u = 1.5\ MJ/m^3$, exchange constant $A_{ex} = 13\ pJ/m$, and a Gilbert damping parameter $\alpha = 0.2$. The DMI values used (0.3, 0.5, 0.75, and 1 mJ/m^2) correspond to different thicknesses of the Pt layers. The material disorder is realistically simulated [66–68] by a random distribution of grains of average size of 10 nm, and an exchange constant being varied at the border of the grains by 43%. A bubble domain of radius 256 nm is initialized in the center of the system and then

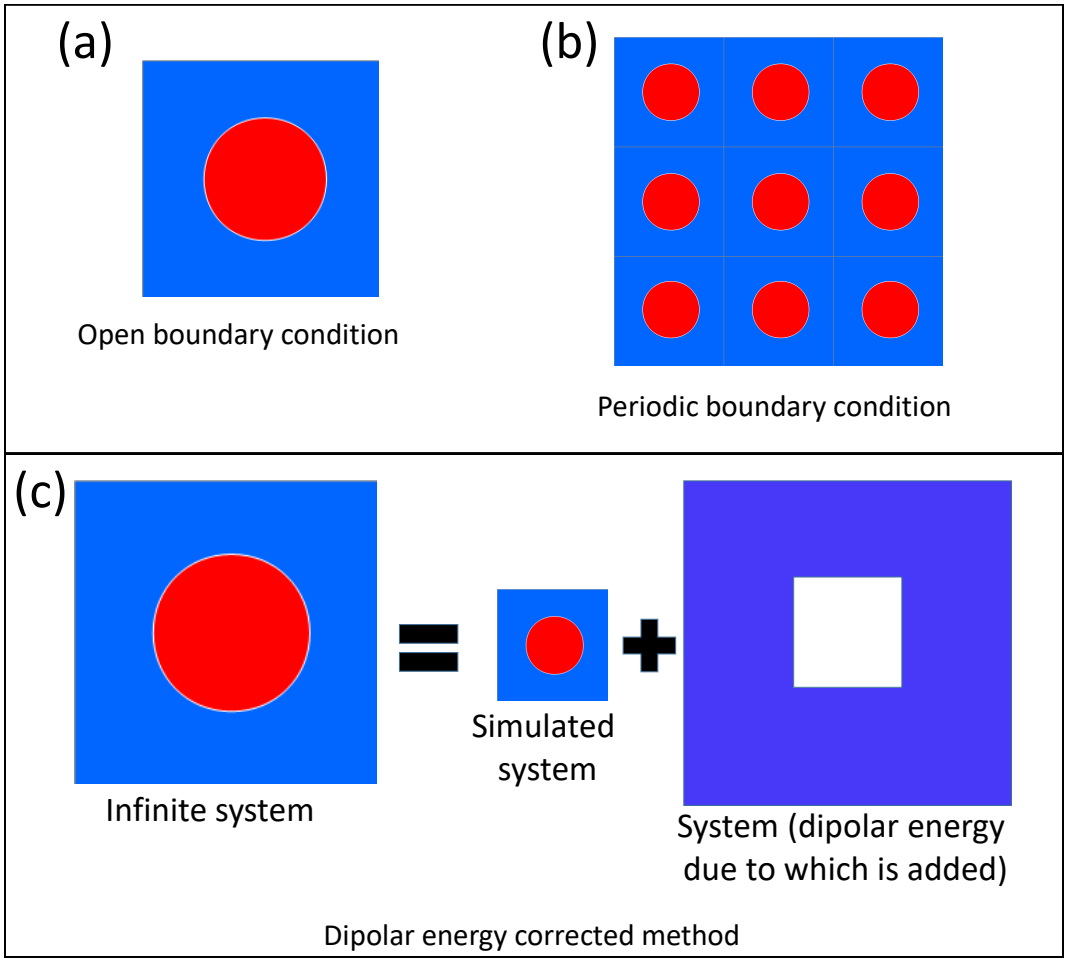

Fig. 3.6 Schematic of the different boundary conditions (a) open boundary condition, (b) periodic boundary condition and (c) dipolar energy corrected boundary condition.

allowed to expand under the application of external fields.The bubble domain is allowed to expand till it almost reaches the boundary of the system. To realistically simulate a large system, we correct for the dipolar energy to that of an infinite system by adding the field generated from outside the simulated square.

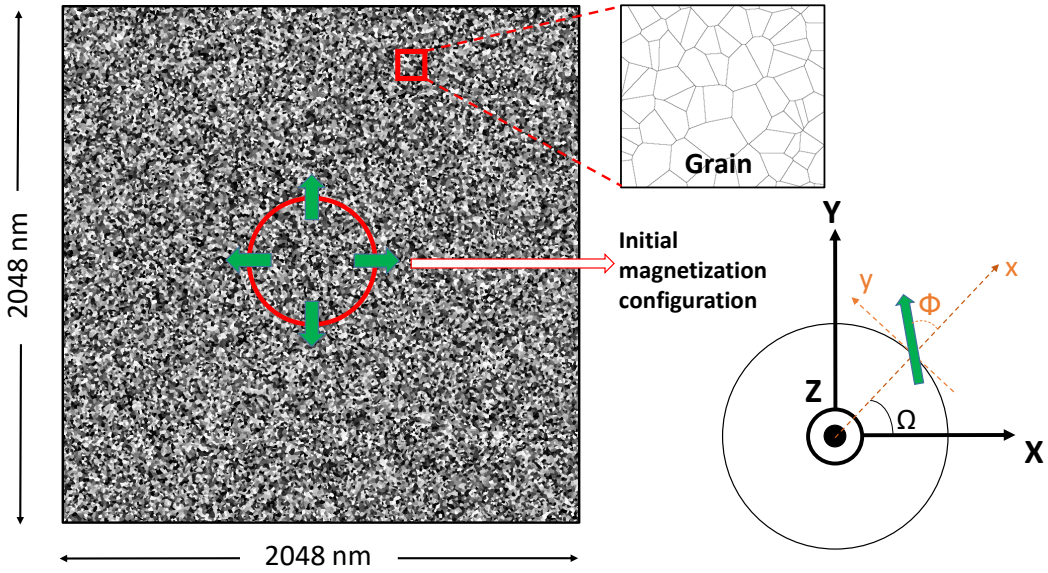

Fig. 3.7 Schematic of the simulation system depicting its dimension, initial magnetization configuration and grains. The thickness of the system is 0.6 nm. The exchange constant is reduced at the border of the grains by 43%.

Chapter 4

Controlling pinning strength with ion irradiation

In section 2.7, we discussed about the creep theory, where motion of domain walls takes place due to thermally activated jumps under very small applied field. We also emphasized in this section that pinning points and their strengths take a vital role in influencing the motion of domain walls. In this chapter, control of the density of pinning points and their strengths by light ion irradiation in perpendicularly magnetized Ta/CoFeB ultra-thin films will be presented.

4.1 Ta/CoFeB/MgO ultra-thin film

In the context of domain wall motion, ultra-thin films with perpendicular magnetic anisotropy (PMA) are of special interest due to their narrow domain wall width ($\sim 10-20$ *nm*) resulting from their high anisotropy values. This makes them good candidates for high density storage. Moreover, magnetic tunnel junctions (MTJs) made of PMA material are also potential candidate for non-volatile memory and logic devices because of their high thermal stability and low threshold current for current induced magnetization switching [69–71]. This has motivated scientists to explore various material systems such as (Co,Fe)-Pt alloys [72, 69, 73], Co/(Pd,Pt) multilayers [74–77] and rare-earth/transition metal alloys [78, 79] for PMA. Other than thermal stability and low threshold current for magnetization switching, a high tunneling magnetoresistance (TMR) ratio is also needed for efficient applications.

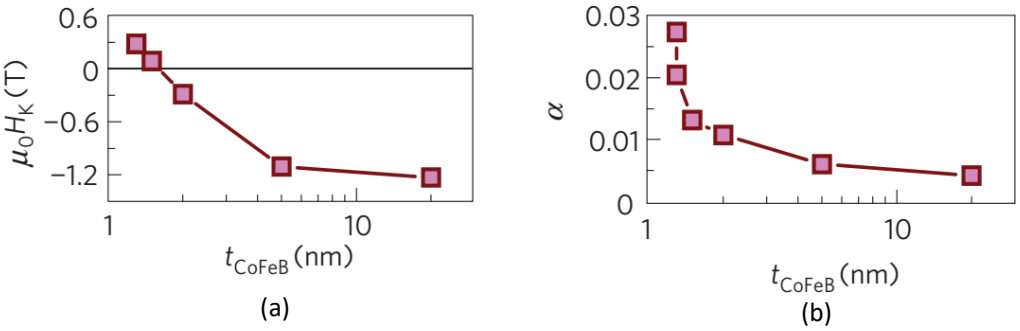

Fig. 4.1 (a) Anisotropy field ($\mu_0 H_K$) and (b) damping parameter (α) as a function of thickness of the CoFeB layer. Adapted from [80].

While none of the above systems meet all the requirements simultaneously, it was shown by S. Ikeda [80] et al. that when CoFeB is grown as an ultra-thin film on a Ta buffer layer with an MgO capping layer, strong PMA along with high TMR ratio (over 120%), high thermal stability at dimensions as low as 40 nm and low switching currents (49 μA) are obtained. Despite these excellent magnetic properties, some structural properties essential for efficient performance of the CoFeB layers in devices are: degree of CoFeB crystallization [81, 82], grain size [83] and the oxidation state of Iron Oxide [84] near the interface. To achieve these properties, CoFeB alloys, which is an amorphous soft magnetic material usually, were also annealed at temperatures around 300 $^{\circ}C$ in order to crystallize into BCC structure. Typically for this class of materials, first Ta atoms are deposited as a smoothening layer in order to minimize the roughness. Then CoFe is deposited in the amorphous state along with the inclusion of boron atoms, which crystallize after annealing, sometimes annealing being preceded by an in-situ infrared annealing [83]. The Ta/CoFeB interface is relatively sharp because Co atoms have solubility of only few percent in Ta and Fe has very low solubility [85]. On the top CoFeB/MgO interface, Oxygen atoms tend to form oxides with Mg instead of Fe, because Fe is nobler than Mg thus reducing corrosion at the interface. This interface becomes sharper upon annealing [82]. Diffusion of Oxygen atoms, which is initially incorporated in the transition metals (Co and Fe) because of the deposition conditions, takes a major role in determining the PMA. While migration of Oxygen atoms is vital for PMA, crystallization of CoFeB is vital for TMR ratio, both having different mechanisms. Thus for PMA one has to find a balance between PMA and TMR ratio. Since in in-plane CoFeB, one does not have to care about oxygen migration, a higher value

of TMR can be achieved. This led to the wide study of in-plane anisotropy CoFeB materials with large TMR ratio and also with very high spin polarization of the tunneling current [86]. However, phenomenal recent results of PMA CoFeB along with its other advantages discussed in the previous paragraph have triggered huge interests for this class of materials to further optimize its material properties.

Mostly exploited parameters for optimization of material properties are stacking of different layers, stoichiometric composition of CoFeB and growth conditions. With regard to the underlayer, Ta, Hf, Pt and Pd have been of particular interest, main concern being under which conditions the material shows PMA. While the origin of PMA has been a matter of debate, with some researchers showing that underlayer non-magnetic material is critical for PMA [87, 88], some researchers claiming that it originates only from the ferromagnetic/oxide interface [80, 89], it was shown by Liu et al. [90] that by replacing Ta underlayer with Hf, clear enhancement of PMA can be achieved. Following this work, a systematic study done with different underlayers showed that with Ta and Hf, PMA is observed for as grown material while with Pt or Pd PMA is observed only for annealed samples [91]. On the other hand, an enhanced PMA has also demonstrated by doping Ta with an optimum amount of Nitrogen atoms [92].

With regard to the CoFeB layer, important factors here are the thickness and composition of this layer. In figure 4.1 (a), anisotropy field is presented as a function of thickness of the CoFeB layer. A positive H_K in this plot means perpendicularly magnetized and a negative H_K means an in-plane magnetized system. H_K increases as thickness decreases and around $t_{CoFeB} = 1.5\ nm$ a change of easy axis from in-plane to out-of-plane takes place. In figure 4.1 (b), variation of damping parameter α as a function of thickness is presented. α increases slowly as the thickness decreases and then steeply increases below 2 nm thickness. However, the value of α even at the thinnest sample (~ 0.03) is much smaller than the typical values measured for Co/Pt (larger than 0.1) [93]. Low α is required for low switching currents in devices.

In a similar development it was reported by Ahn and Beach [94] for Ta/Co_xFe_{1-x}/MgO material that no PMA is obtained for Ta/Co/MgO or Ta/Fe/MgO with pure Co or Fe composition, but clear PMA is obtained for samples with intermediate composition. Other than the composition, growth conditions of the material (annealing or as-grown) also play a major role in PMA. In figure 4.2, hysteresis loops for different Co, Fe and B compositions are shown. $Co_{20}Fe_{60}B_{20}$ and $Co_{40}Fe_{40}B_{20}$

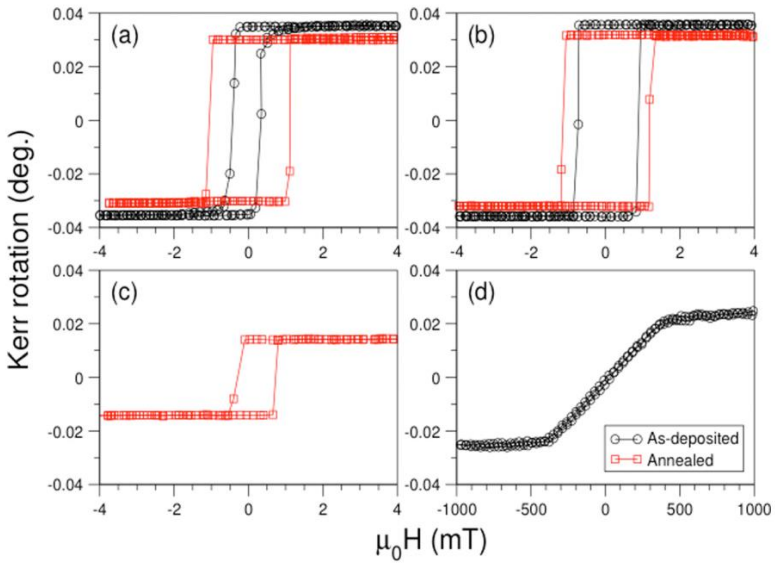

Fig. 4.2 Hysteresis loops measured for different combinations of Co, Fe and B compositions in annealed (red) and as-deposited (black) samples using MOKE. (a) $Co_{20}Fe_{60}B_{20}$, (b) $Co_{40}Fe_{40}B_{20}$, (c) $Co_{60}Fe_{20}B_{20}$ annealed, and (d) $Co_{60}Fe_{20}B_{20}$ as deposited. Adapted from [96].

show perpendicular magnetic anisotropy in both as grown (amorphous) and annealed state. However for $Co_{60}Fe_{20}B_{20}$ samples, as grown samples show an easy axis along the in-plane direction. However after annealing at 300 °C for 2 hours it shows some PMA (figure 4.2(c)). This suggests that annealing has an effect in increasing the anisotropy. It is also reflected in the figure that hysteresis loop for annealed one is sharper compared to the as-grown one.

MgO layer in Ta/CoFeB/MgO also influences the PMA. Dependence of PMA on MgO layer thickness was investigated by Yamanouchi et al. [95]. They found that a clear PMA was obtained in material having 1.5 nm thick CoFeB layer for MgO of more than 3 monolayers.

Later when obtaining PMA in CoFeB became a established procedure, C. Burrowes et al. [96] studied the creep velocities of DWs (figure 4.3) in ultra-thin Ta(5 nm)/CoFeB(1 nm)/MgO(2 nm)/Ta (5 nm) films for different compositions of Co and Fe in both annealed and as-grown states as a function of applied field. One of the striking feature in this plot is that DW velocity is obtained at fields as small as $0.1mT$. The depinning field, measured as the field value beyond which the velocity deviates from the creep law, obtained for all these samples is in the range of $2-3mT$. These

values of depinning fields are much smaller than typical values obtained for other 3d ferromagnetic PMA films such as FePt [97], Co/Pt [98] or Co/Ni [99]. For these materials, depinning fields are usually larger than $20mT$. These small depinning values in CoFeB samples were attributed to factors such as lower interface roughness, lower density of grain boundaries etc. relative to Co/Pt, Co/Pd or Co/Ni. This property of the CoFeB films makes it further attractive for applications because, a high depinning field means that a high threshold current is required for current induced domain wall motion and a high threshold current is detrimental for applications.

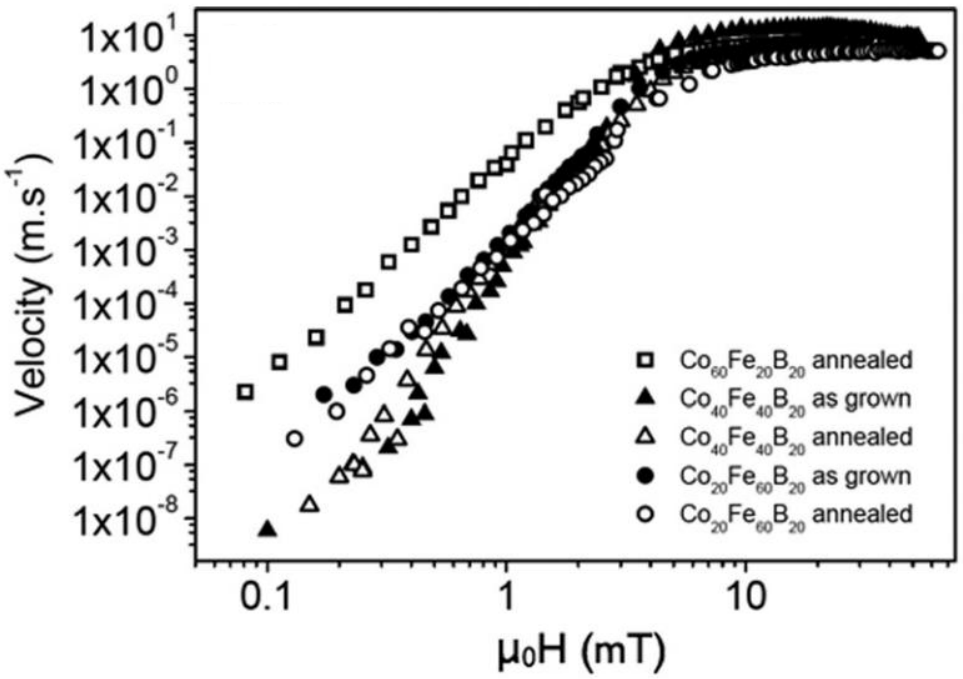

Fig. 4.3 DW velocities of different CoFeB samples: as grown (solid) and annealed (empty) as a function of applied field. Different symbols: square, triangle and circle represent different CoFeB compositions. Adapted from [96].

4.2 Light ion irradiation

It was shown by C. Chappert et al. [100] for Pt/Co thin film layers that irradiating the sample with light He^+ ions provides very good control of magnetic properties due to the intermixing of atoms at the Pt/Co interfaces. Perpendicular anisotropy in ultra-thin PMA materials is largely due to interfacial anisotropy and it arises because

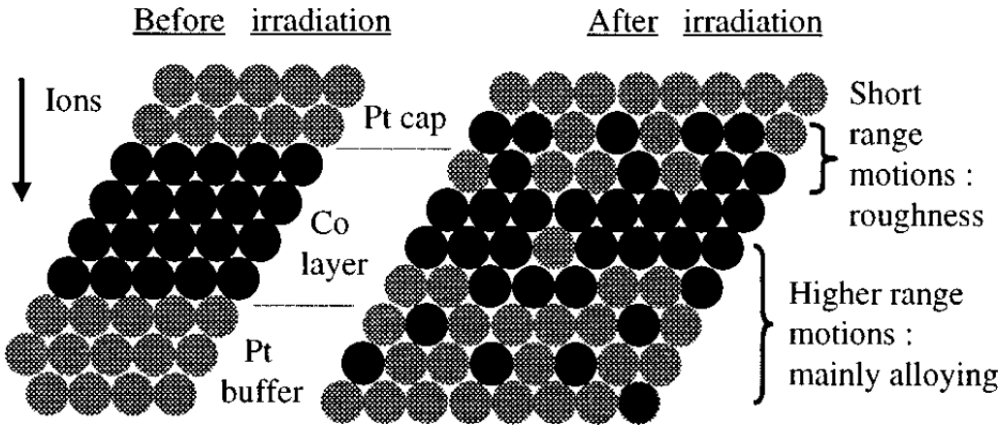

Fig. 4.4 Schematic of a Pt/Co/Pt layer to illustrate the effect of irradiation. Co atoms are represented in black and Pt atoms are represented in gray. Ions are irradiated from the top. Adapted from [102].

of symmetry breaking at the interfaces. Anisotropy energy having its origin in the spin-orbit coupling, depends on the environment of the atoms. Thus changing this environment at the interfaces with light ion irradiation facilitate an excellent tool to change its magnetic properties.

The change of atomic environment at the interfaces due to ion irradiation is depicted in figure 4.4 for a Pt/Co/Pt layer. Upon irradiation, intermixing of atoms takes place at the interfaces. Co atoms at the top layer undergo a short range motion (one atomic distance), while Co atoms at the bottom interface undergo a higher range motion. Here Co atoms can get isolated resulting in alloy formation. On the other hand, the motion of Co atoms at the top layer contributes to roughening of the interface having higher roughness with increasing irradiation. Other than roughening and alloying effect, irradiation can cause also strain release effect if the fluence is small ($\leq 10^{16}$ He^+/m^2) [101]. Strain arises due to the lattice mismatch between buffer layer and the ferromagnetic layer. Both roughening as well as strain release leads to a decrease in the magnetic anisotropy.

Effect of He^+ ion irradiation on Ta/CoFeB/MgO films has recently been studied by L. Herrera Diez et al. [103]. In their studies (figure 4.5), a clear decrease in effective magnetic anisotropy constant (K_e) and saturation magnetization (M_s, not shown in figure) as a function of irradiation dose was observed. Creep velocities of the DWs as a function of irradiation showed first an increasing behavior (from

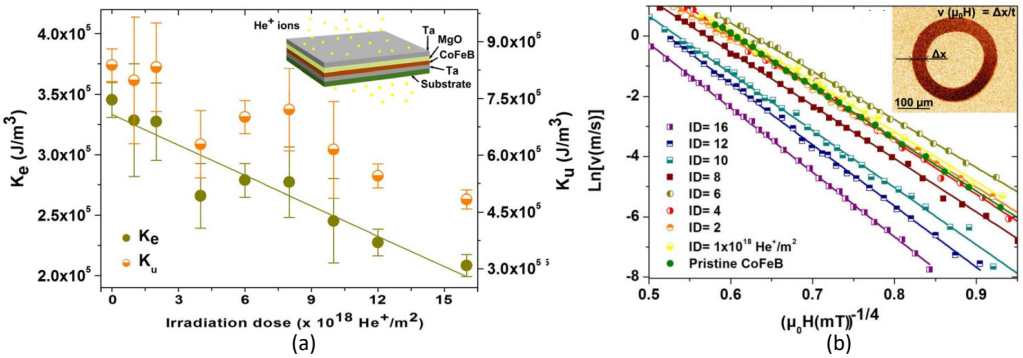

Fig. 4.5 (a)Variation of effective anisotropy (K_e) and magnetocrystalline anisotropy (K_u) as a function of irradiation dose. At the inset is a schematic of the Ta/CoFeB/MgO sample, (b) creep velocity (expressed in $ln[v(m/s)]$) as a function of applied field (expressed in $(\mu_0 H(mT))^{-1/4}$) for different irradiation doses. Symbols are experimental values and solid lines are fitting to equation 2.58. At the inset is the measurement scheme for velocity. Adapted from [103].

non-irradiated to fluence up to 6×10^{18} He^+/m^2) and then a decreasing behavior. The decrease in anisotropy could be understood because of the diffusion of Fe atoms from the upper CoFeB/MgO interface to the lower Ta/CoFeB interface, thus causing a change in the nature of the Fe oxide at the interface. It was also previously shown that by adding Fe atoms into the top CoFeB/MgO interfaces, an increase in the anisotropy constant could be attained [104]. It was also reported for these films that an increase in the damping parameter (α) from 0.01 to 0.03 can be attained by increasing the irradiation dose from 0 to 40×10^{18} He^+/m^2 [105]. While these studies presented excellent evidence of tuning the magnetic properties with irradiation, behavior such as velocity of domain walls remained challenging to explain and asked for deeper studies.

4.3 Control of pinning points by ion irradiation

In the previous section, studies done in order to understand the effects of ion irradiation on ferromagnetic samples are presented. All these studies present the effects of irradiation in terms of how macroscopic properties such as effective anisotropy, saturation magnetization, depinning field or domain wall velocities of the ferromagnet are affected. On the other hand, in section 2.7, we have seen that domain wall velocities in the creep regime depend on the number of microscopic pinning points

(pinning density) and their strengths. Particularly for PMA samples, the density of pinning points is of significant importance because PMA samples have narrow DWs and narrow DWs interact strongly with the random pinning points [106]. Due to these interactions, DWs get pinned and it is important to understand the pinning points from an application point of view as the motion of DWs is required to be predicted precisely. While experimental characterization of the localized pinning points remain notoriously challenging, we use the image processing method, described in section 3.1.5 to probe the pinning points, using domain walls at very small velocities deep in the creep regime that sweep across the pinning points.

In figure 4.6, the evolution of the bubble domain in the presence of a field ($\mu_0 H_z$) applied along the negative out-of-plane direction (into the plane) for three different samples (non irradiated, irradiated with fluence $8 \times 10^8\ He^+/m^2$ and irradiated with fluence $16 \times 10^8\ He^+/m^2$) are presented. To facilitate comparisons between the three samples the field H for bubble expansion was chosen such that the ratio $H/H^* = 0.01$ (refer equation 2.58) remains constant (H^* being an approximation of H_{dep}, taken from [103]). The images of the expanding magnetic bubbles at consecutive time steps were then processed as shown in figure 4.6 in order to visualize locally the bubble DW dynamics. While the magnetic bubble nucleated in the non-irradiated sample conserves its circular shape upon expansion (Fig. 1(a)), ion irradiation clearly increases the jaggedness of the DW in the other two samples, where the bubble DW evolves into a "cauliflower" shape figure 4.6 (b-c). This difference in jaggedness of the DW upon irradiation is due to the interplay of the number of pinning sites and their strength, governed by the degree of intermixing at the CoFeB/MgO and CoFeB/Ta interfaces [103]. From the time scale in the figure, it is also clear that the DW velocity is lowest for the non-irradiated case, then it increases for the medium irradiated one and then decreases for the highest irradiated one. From equation 2.58, we can see that for the same H/H_{dep} ratio, the velocity of the wall depends on the scaling energy constant U_c, which in turns (equation 2.52) depends on elastic energy of the wall (E_{el}), pinning force (f_{pin}) and density of pinning centers (n_i) with the relation $Uc \sim [E_{el}\xi^4\gamma_{pin}]^{\frac{1}{3}}$. The fact that the effective anisotropy constant decreases as a function of irradiation creates the initial impression that the velocity should increase as a function of irradiation. However, this is not true. This suggests that the change in anisotropy alone is not enough to explain the behavior of first increase and then decrease in velocity with irradiation. To explain this, local dynamics of the domain wall was studied and presented in the next section.

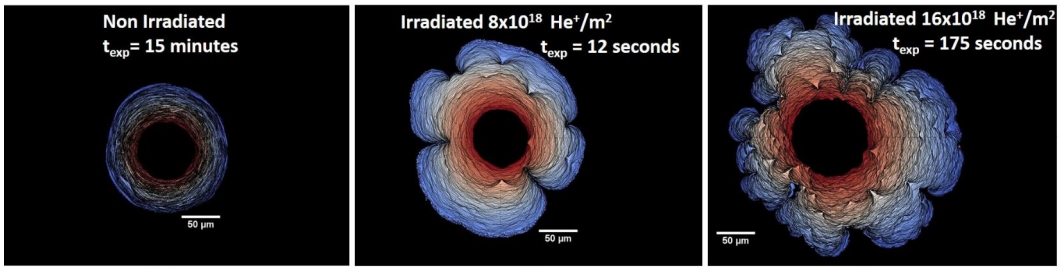

Fig. 4.6 Evolution of the bubble domain for the (a) non-irradiated film, (b) irradiated film with fluence $8 \times 10^{18}\ He^+/m^2$ and (c) irradiated film with fluence $16 \times 10^{18}\ He^+/m^2$ under the application of an out-of-plane field keeping H/H*=0.01. Each line represents a DW at a particular instant. Each image in (a), (b) and (c) is obtained by adding DWs from sequential images. Time lapses between two consecutive frames are 3s, 100 ms and 700 ms for (a), (b) and (c) respectively. Black domain at the center is the initially nucleated bubble domain. Color gradient represents the time evolution.

4.4 Local Dynamics of Domain Wall

In order to quantify the local dynamics of the DW expansion, we use the processed images in figure 4.6 to extract the waiting times of the DW at each pixel. To this aim, we first generate a Waiting Matrix $W(x,y,t)$ by calculating the total amount of time spent by the DW front $h(x,y)$ at each position (x,y) of the image, recorded as:

$$W(x,y,t) = \sum_t F(x,y) \tag{4.1}$$

where t represents all discrete times in one experiment over which summation runs and $F(x,y)$ is the so-called Front Matrix assigned to each recorded image. The size of the Front Matrix is equal to the size of the recorded image. $F(x,y)$ at an instant 't' is assigned the following value:

$$F(x,y) = \begin{cases} 1 & if\ h(x,y) = x,y \\ 0 & otherwise \end{cases} \tag{4.2}$$

Thus, $F(x,y)$ is assigned a value of one when $h(x,y) = x,y$, i.e. when the DW is located at the position (x,y). Otherwise, it is assigned a value of zero. This method for local dynamics was first developed to study the propagation of a crack along a heterogeneous weak plane [107, 108]. The Waiting Matrix is a matrix of integers

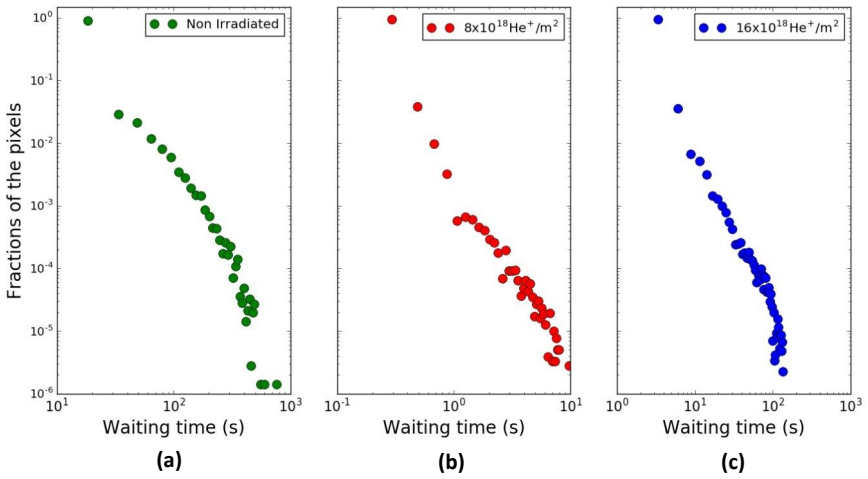

Fig. 4.7 Logarithmic plot of distributions of the waiting time for (a) non-irradiated film, (b) irradiated film with fluence 8×10^{18} He^+/m^2 and (c) irradiated film with fluence 16×10^{18} He^+/m^2. Along vertical axis is the fractions of the total number of pixels where the DW is detected during its propagation.

and in order to get the local waiting time of the DW, this matrix has to be multiplied by the time lapse between two consecutive frames.

In figure 4.7 distributions of the local waiting time of the DWs for the three samples in a logarithmic plot are presented. The distribution could follow an exponential decay in the non-irradiated case, while it could follow a power law in the irradiated cases. The values of the waiting times are different for the three samples. Indeed, as observed from figure 4.6 as well, waiting times are largest (i.e. velocity is smallest) for the non-irradiated sample, indicating largest values of the average pinning energy barrier U_c. Irradiation with a fluence of 8×10^{18} He^+/m^2 decreases the strength of the induced pinning centers, while a further increase in fluence introduces pinning centers with larger pinning strength. These results thus indicate that there should be an optimal fluence with minimum pinning barrier and pinning density.

In figure 4.8, the waiting time of the domain wall above a threshold value is presented for the three samples in a scatter plot during the expansion of the bubble. The threshold value for each case is assigned a value of two times the standard deviation of the non-zero waiting time distribution in the sample. The waiting time is proportional to the strength of the pinning points and therefore, it is a measure of the strength. A scatter point larger in size compared to other points in the sample

signifies that its strength is larger compared to other points as well. In the non-irradiated case it is seen that pinning strengths are homogeneous, but larger in values, compared to irradiated ones. Thus lots of homogeneous pinning points (n_i) with higher strengths (f_i) compared to other samples lead to largest U_c and thus, slowest domain wall velocity. On the other hand, in the irradiated cases there are few points with strong pinning strength.

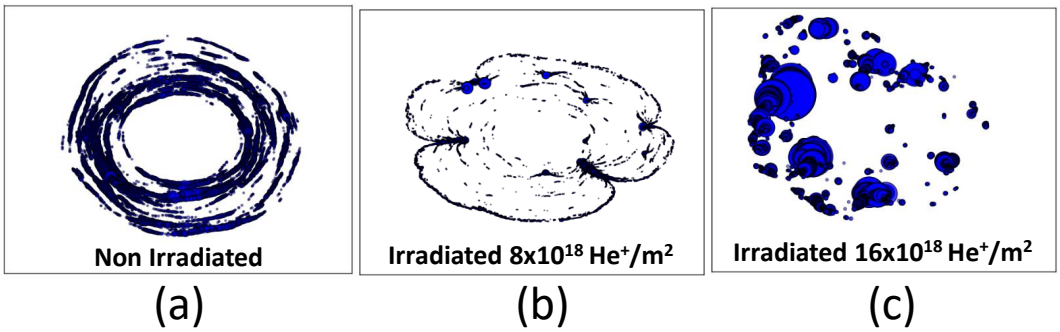

Fig. 4.8 Scatter plot of the waiting time (a measure of pinning strengths) for (a) non-irradiated film, (b) irradiated film with fluence 8×10^{18} He^+/m^2 and (c) irradiated film with fluence 16×10^{18} He^+/m^2.

Although intuitively it may seem that with irradiation number of pinning points and its strength should increase, our results show the opposite. Both irradiated samples have lower pinning strengths compared to the non-irradiated one. This could be due to the suppressing effect of irradiation in the range non-irradiated to 8×10^8 He^+/m^2 and then with further irradiation new stronger pinning points are created.

4.5 Conclusion

In conclusion, the dynamics of bubble DWs in terms of the local waiting time for three PMA samples with different irradiation fluences have been studied. Our analysis shows that ion irradiation influences both the number of pinning sites and their strength, and suggests there may be an optimal irradiation fluence at which DW dynamics are faster.

Chapter 5

Dynamics and morphology of chiral magnetic bubbles

We have discussed in Chapter 1 that the study of domain wall (DW) dynamics in ultra-thin films and nanowires has attracted significant attention in the spintronics research community due to its potential for applications in future memory, logic and sensing devices. All these applications require moving multiple DWs precisely with applied spin-polarized currents or magnetic fields. Initially, DW dynamics in Permalloy with in-plane magnetic anisotropy were extensively studied [109–113]. Afterwards, perpendicularly magnetized ultra-thin films attracted particular interest due to narrower domain walls compared to their in-plane magnetized counterparts. It was found that current-driven DW motion provides higher efficiency due to the enhanced values of spin-torque efficiency [114, 115], with the DWs moving in the same direction as that of the electrons flow. On the contrary, in heterostructures composed of a magnetic ultra-thin film adjacent to a heavy metal layer, it was found that DWs move in the direction opposite to the flow of electrons. This behavior was attributed to the spin Hall effect [116], which acts on the walls having a Néel configuration. In simultaneous developments, it was suggested that in such ultra-thin films the Dzyaloshinskii-Moriya Interaction (DMI) [117, 118] can result in a Néel wall type rather than a Bloch one [26, 119–121]. Interfacial DMI, as discussed in section 2.4, arises due to the high spin-orbit coupling in the heavy metal layer and the broken inversion symmetry along the thin-film layers. It results in an anti-symmetric exchange interaction, favoring an orthogonal orientation between two neighboring spins in contrast with the parallel alignment of the Heisenberg exchange interaction.

Remarkably, the DMI imposes the magnetization to rotate from one domain to the next with preferred handedness or chirality, resulting in right-handed and left-handed chiral Néel DWs. Such a property is essential for the spin-orbit torque to drive the DWs in the same direction, a feature that is fundamental for the realization of the next generation of devices, such as racetrack memories. Furthermore, two nearby Néel DWs with opposite chirality are extremely stable topologically, thus making them particularly suitable for applications.

In order to precisely control future spintronics devices, it is imperative to understand, control and measure the DMI. Several efforts have been made to estimate its value using different methods: asymmetric magnetic bubble expansion [122, 123], magnetic stripe domains annihilation [124] and Brillouin light scattering [125]. Especially for low values, the estimation can vary dramatically from method to method, also for nominally identical material systems. This is probably due to the strong sensitivity to interface quality, growth conditions [126, 127], thickness of heavy metal layer [128] etc. The simplest and thus most widely used method relies on magneto-optical measurements of the asymmetric expansion of a magnetic bubble under the simultaneous presence of in-plane and out-of-plane magnetic fields. In these experiments, the DMI value is inferred from the measure of the DMI field, i.e. the in-plane field at which the velocity of the bubble DW reaches a minimum. Implicitly, the DW is assumed to keep its width fixed during the expansion, which results in a constant DMI field.

In this chapter, we aim to test these implicit assumptions with micromagnetic simulations of the DW dynamics in a disordered medium (section 3.2), where the disorder is realistically incorporated into the material as a collection of grains with randomly distributed sizes and varying exchange constant at the edges.

5.1 Bubble domain without disorder

In this section stability of a bubble domain in the absence of any disorder is presented. In figure 5.1(b), snapshots of the bubble domain under the application of a field pulse (figure 5.1(a)) is shown. When a non-zero field is applied to the bubble of 512 nm in diameter for 5 ns, keeping the DMI constant at 0.5 mJ/m^2, the bubble domain start to expand and keep expanding until field becomes zero. When the field becomes zero, it starts shrinking and eventually disappear completely after 24 ns. This instability of

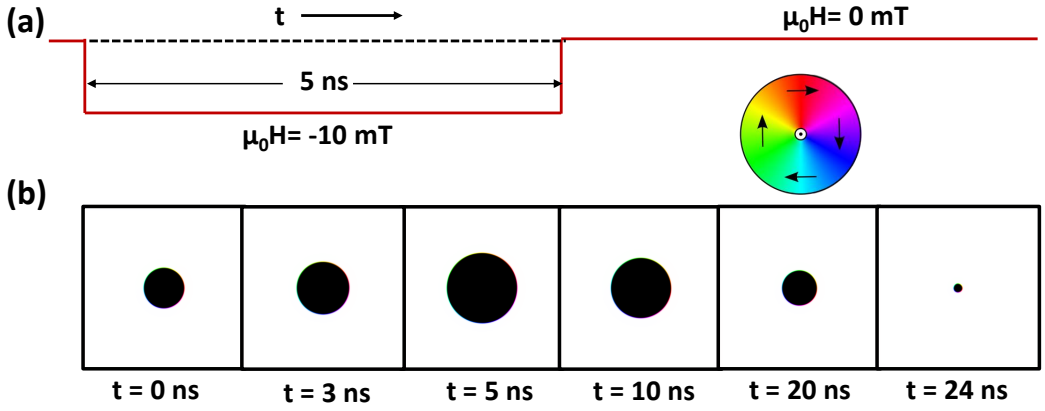

Fig. 5.1 (a) Schematic of the field pulse used and (b) snapshots of the bubble domain during its evolution at different times under the application of this pulse. DMI is kept constant at 0.5 mJ/m^2. Black means magnetization into the plane and white means magnetization out of the plane. Bubble domain keeps expanding when the field is on till 5 ns, then it starts to collapse as soon as field is removed, eventually leading to its complete disappearance. The wheel represents the color code for in-plane magnetization direction, red meaning magnetization along positive x-direction and blue meaning magnetization along negative y direction.

the bubble can be understood with the work of N. S. Kiselev *et al.* [129] presented in figure 5.2, where energy (E in blue) of the bubble is shown as a function of their size (radius R). It shows that there are some stable solutions (only one in this figure at $R = R_1$) where a bubble of particular radius can be stable. If it is below a critical radius R_C, then the bubble is not stable and collapses. However, when disorders are included in the system, bubbles remain stable without any external field. It is also worth noting that the domain wall of the bubble maintain Néel like structure during its expansion as well as shrinking, suggesting that a DMI constant of 0.5 mJ/m^2 is strong enough to make the domain wall completely Néel.

5.2 Dynamics of the Bubble in the Presence of In-plane Field

In figure 5.3 we present a snapshot of the bubble domain dynamics for a DMI constant of 0.5 mJ/m^2 during its evolution under the application of an out-of-plane field of -17 mT for different in-plane fields. Without an in-plane field the bubble

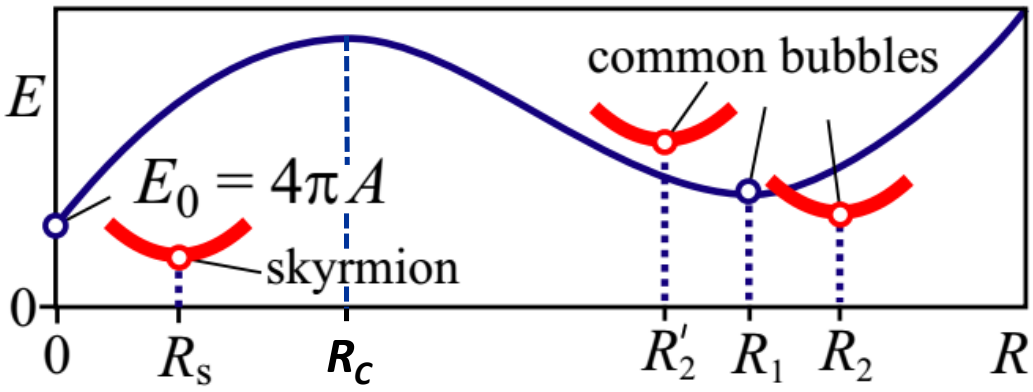

Fig. 5.2 Variation of energy of the bubble as a function of radius of the bubble. Adapted from [129].

.

domain expands symmetrically, while for a non-zero in-plane field, it becomes strongly asymmetrical, as expected. Remarkably, for in-plane fields between 30 mT and 100 mT, the front opposite to the direction of the in-plane field becomes "ripple-like", and the magnetization inside the DW undergoes a complex rotation as we show in the zoomed-in areas of figure 5.3. On the other hand, for very low and for very high in-plane fields, these ripples are absent and the domain wall appears rather smooth.

The fact that the magnetic bubble expands symmetrically without an applied in-plane field and asymmetrically when a non-zero in-plane field is applied, as shown in Fig. 5.3, is well-known for most perpendicular ultra-thin films with DMI. In our simulations we use positive values of DMI, so that the DMI field acts on the bubble domain in the radially outward direction. A positive in-plane field is thus parallel to the DMI field on the right side of the bubble and antiparallel on the left side. When these fields are parallel (antiparallel) they stabilize (destabilize) the DW. This simple picture helps us to understand why it is possible for the ripples to form. Incidentally, this is valid only when the two fields are comparable in amplitude, as at higher in-plane fields the DWs are very stable again.

In order to understand how the ripples affect the bubble expansion, we show in figure 5.4(a) the velocity of the right domain wall (RDW) and left domain wall (LDW) as a function of in-plane fields at two different out-of-plane fields (-13 mT and -17 mT). As the in-plane field decreases from higher positive values towards zero, the velocity of the RDW decreases. It keeps decreasing till a negative in-plane

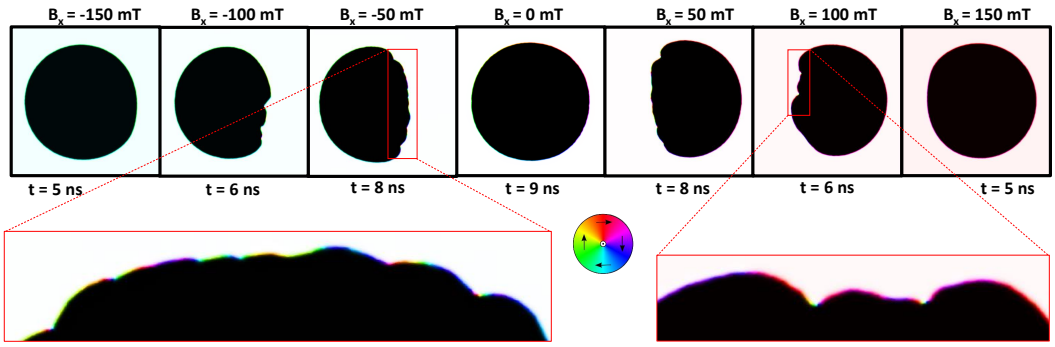

Fig. 5.3 Snapshots of the bubble domain during its expansion at different times under the application of an out-of-plane field of -17 mT and in-plane field (Bx) as indicated, keeping the DMI constant 0.5 mJ/m^2. Black means magnetization into the plane and white means magnetization out of the plane. The wheel represents the color code for in-plane magnetization direction, red meaning magnetization along positive x-direction and blue meaning magnetization along negative y direction.

field value, then steeply decreases, reaches its minimum and then increases again. For comparison, we show the width of the domain wall as a function of in-plane fields in figure 5.4(b) at the same out-of-plane fields. For both cases, the minimum is not at zero in-plane field, but it is shifted at values roughly corresponding to the onset of the drop in the DW velocity. On the other hand, it does not significantly depend on the out-of-plane fields.

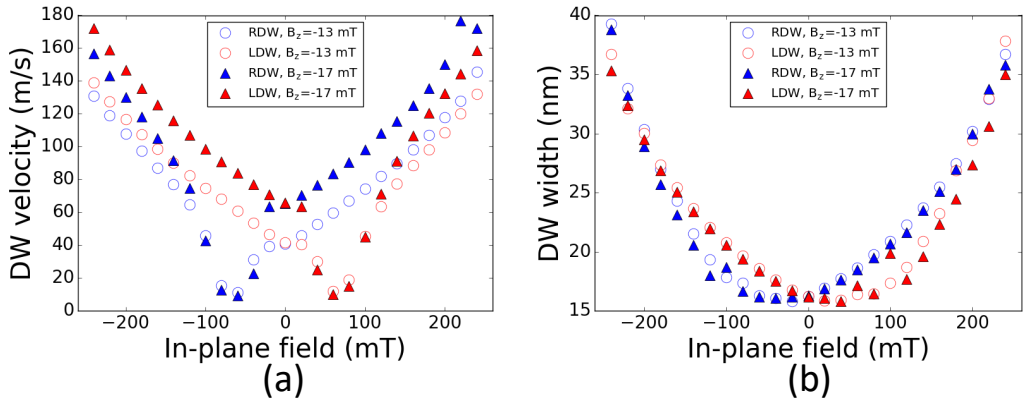

Fig. 5.4 Velocity (a) and width (b) of the right domain wall (RDW) in blue and left domain wall (LDW) in red as a function of in-plane field for $D = 0.5\ mJ/m^2$. Circles (empty) and triangles (solid) represent velocities at out-of-plane fields of -13 and $-17\ mT$, respectively.

Figure 5.5(a) displays the velocity of the RDW as a function of in-plane field for different DMI constants, and an out-of-plane field of $-17\ mT$. The nature of the velocity vs. in-plane field curve is similar to figure 5.4(a), moving the minimum

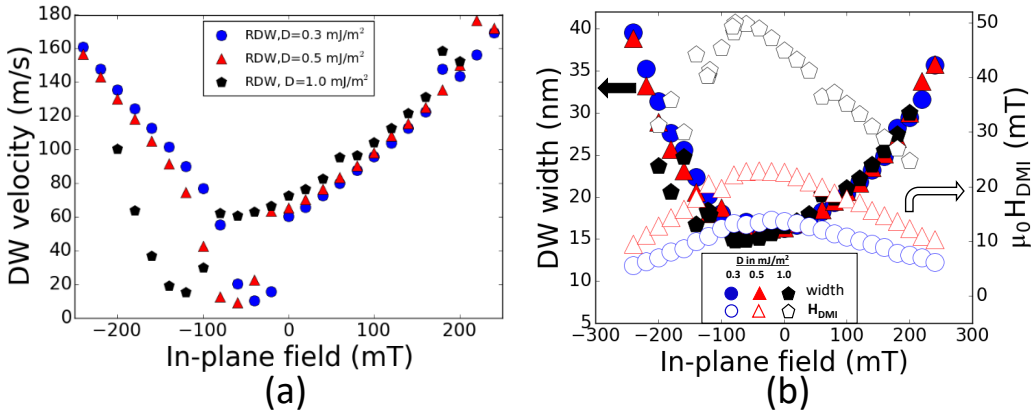

Fig. 5.5 (a) Velocity of the right domain wall (RDW) as a function of in-plane field at constant out-of-plane field of -17 mT, (b) width and DMI field of the RDW as a function of in-plane field for 3 different DMI constants keeping the OOP field constant at -17 mT.

at larger (negative) values for increasing DMI value. As shown, the formation of ripples is reflected in the velocity curves in Figs. 5.4(a), and 5.5(a). Some aspects of these curves can be understood with the help of the equation for free energy of the domain wall, given by [130]:

$$\sigma_{DW}(H_x,\Phi) = \sigma_0 + 2K_D\Delta cos^2(\Phi) - \pi\Delta M_s(H_x + H_{DMI})cos(\Phi) \qquad (5.1)$$

where σ_0 is the Bloch wall energy, and K_D the domain wall anisotropy energy. This equation tells us that the energy of the DW is anisotropic and depends on the magnetization angle of the DW. The energy of the DW is then maximum when H_x and H_{DMI} are antiparallel and minimum when parallel. The DWs with the maximum energy have the minimum velocity. This expression explains why there is a horizontal shift in the velocity curve.

Corresponding to figure 5.5(a), we show in figure 5.5(b) the width of the RDW and the DMI field as a function of in-plane field. The DMI field H_{DMI} is calculated using the expression $\mu_0 H_{DMI} = D/(M_s\Delta)$, where D is the DMI constant and Δ is the DW width. The latter depends on the in-plane field and has its minimum shifted towards a negative in-plane field value in the same way as in figure 5.4(b), while it does not show any marked dependence on the DMI constant. Having a dependence on the DW width, we can conclude that the DMI field also varies with the in-plane field.

D (mJ/m^2)	Onset (mT)	Minimum (mT)
0.3	0±2	-40±2
0.5	-22±2	-62±2
0.75	-38±2	-100±2
1	-80±2	-120±2

Table 5.1 Onset field and minima field for the right domain wall (RDW) at $B_z = -17\ mT$ for different DMI constants.

On the other hand, a few characteristic points can be identified in the velocity curves of figures 5.4- 5.5, as reported in Table 5.1. By 'Onset' we mean the in-plane field at which the velocity of the wall decreases steeply and the 'Minimum' is the in-plane field at which the velocity of the wall is minimum. In the table, magnitude of both the onset and minimum fields increase as a function of DMI.

5.3 Nucleation of Vertical Bloch Lines and evolution of topological Charge

The occurrence of ripples and the flattening of the bubble domain is clearly related to the kink like feature in the velocity vs in-plane field curve, described above. To better understand its origin, we present in figure 5.7(a) the magnetization angle φ at the center of the DW (with φ measured with respect to a fixed coordinate system, as in the sketch) against its position around the bubble (expressed by the angle Ω). With this representation, a perfect Néel wall all around the bubble periphery translates into a smooth increase from the coordinate $(0,0)$ to $(2\pi,2\pi)$. On the other hand, a Bloch wall all along the periphery would increase from $(0,\pi/2)$ to $(3/2\pi,2\pi)$ and then decrease to $(2\pi,\pi/2)$.

We present the case for an out-of-plane field of $-17\ mT$, an in-plane field of $100\ mT$ and a DMI constant of $0.5\ mJ/m^2$ as a typical behavior. At 0.2 ns after the application of the fields, the in-plane magnetization rotates along the periphery from 0 to 2π with some local fluctuations, showing a clear Néel wall configuration. At 4.38 ns, the magnetization still starts at 0 and ends at 2π, but showing big fluctuations. In particular, the in-plane magnetization suddenly makes a 2π rotation in clockwise direction (negative), comes back to zero with an anticlockwise rotation of 2π and makes another 2π rotation anticlockwise to end at 2π. A rotation of 2π angle of

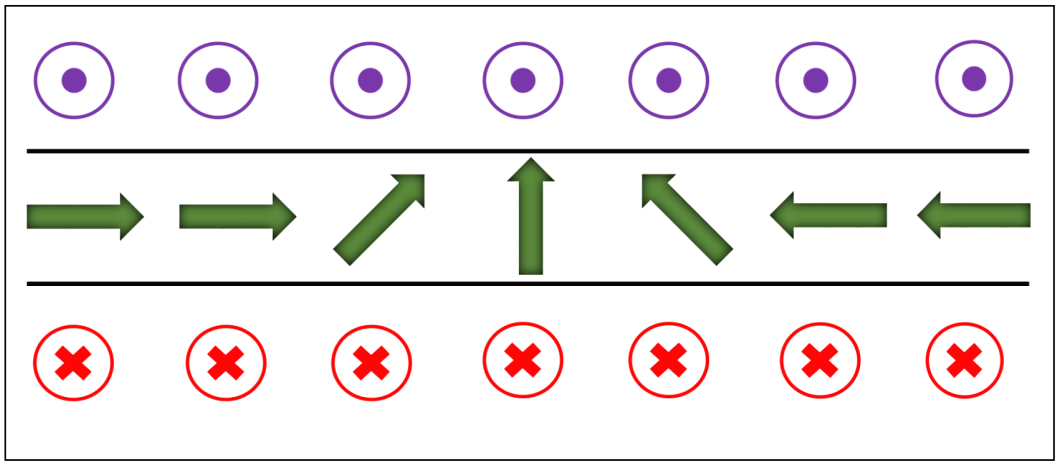

Fig. 5.6 Schematic representation of a vertical Bloch line (VBL) where rotation of the magnetizations take place inside a DW.

the in-plane magnetization along the periphery corresponds to the onset of a pair of vertical Bloch lines (VBL) [131]. As a matter of fact, three pairs of VBLs occur at t = 4.38 ns and two pairs at t=4.40 ns, meaning that two VBLs annihilate during the 20 ps time interval. These complex rotations of 2π angle are also visible in Fig. 5.3 as color fluctuations in the bubble front.

A schematic of a vertical Bloch line is shown in figure 5.6. A VBL is a topological defect where a rotation of the magnetization along the length of a DW takes place, thus dividing the domain wall. They are nucleated in disordered systems due to the incoherent precession of the magnetic moments within the DWs due to the spatial inhomogeneities of the effective field. Clearly, they are nucleated in pairs in order to conserve the total topological charge Q_{total} of the system. In other words, they must have opposite topological charge $\pm Q_{VBL}$. After nucleation, these VBLs start propagating and interact with each other. Different VBLs can have different widths due to the inhomogeneous component of the B_x acting on them, so that they also have different velocities [131]. As a consequence, fast VBLs come close to the slower ones and can annihilate each other if energetically favorable. These dynamics of VBLs are schematically shown in figure 5.8. Annihilation events can be studied in terms of time evolution of the total topological charge $Q_{total}(t)$, expressed as [132]:

$$Q_{total}(t) = \frac{1}{4\pi} \iint \mathbf{m}(t) \cdot \left(\frac{\partial \mathbf{m}(\mathbf{r},t)}{\partial x} \times \frac{\partial \mathbf{m}(\mathbf{r},t)}{\partial y} \right) dxdy \tag{5.2}$$

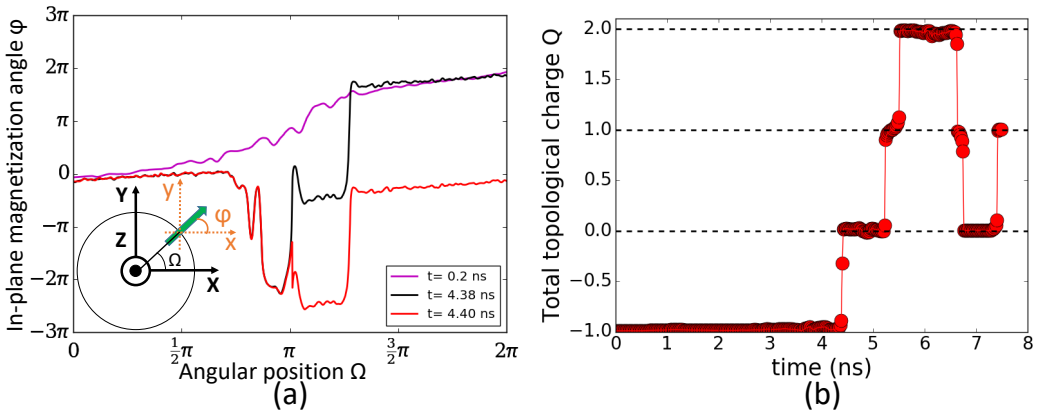

Fig. 5.7 (a) In-plane magnetization angle φ of the domain wall along the periphery of the bubble as a function of angular position of the DW. Positive (negative) angle means an anti-clockwise (clockwise) rotation. (b) Evolution of the total topological charge Q of the system showing six annihilation events of ± 1, corresponding to annihilation of two VBLs with the same topological charge of $\pm 1/2$.

where $\mathbf{m}(t)$ is the normalized magnetization at time t and position $\mathbf{r}$. Figure 5.7(b) shows six annihilation events where the topological charge jumps by ± 1, for which a pair of VBLs annihilate both having topological charge +1/2 or -1/2 respectively. Clearly, these jumps are not perfectly an integer number, due to the presence of disorder.

Although in the previous section, why there is a horizontal shift in the velocity curves of figures 5.4 and 5.5 could be explained, but the asymmetry in those curves, relative to the curves minima, observed in our simulations as well as in other experiments [127] could not be explained. It has been speculated that a chiral damping arising out of spin-orbit interaction could be responsible for this [130]. D.-Yun Kim *et al.* proposed that the asymmetry in the velocity curve is due to the dependence of energy on DW width [133]. In order to understand the flattening of the bubble, we need to explain it taking into account the formation of VBLs that we observe. Although the flattening of the bubble [134] or kink-like feature [127] of velocity vs in-plane field curve has been observed experimentally, most of these works focus on extracting the value of the DMI, while the shape of the bubble is seldom studied. D. Lau *et al.* used energetic calculations of the equilibrium shape of the bubble domain wall by Wulff construction in order to explain the shapes [134]. In their studies, they observed an asymmetric expansion of the bubble with a flattening DW at lower in-plane fields and a non-elliptical tear-drop shape at higher in-plane fields. While the tear-drop shape could be explained using the Wulff construction, it was

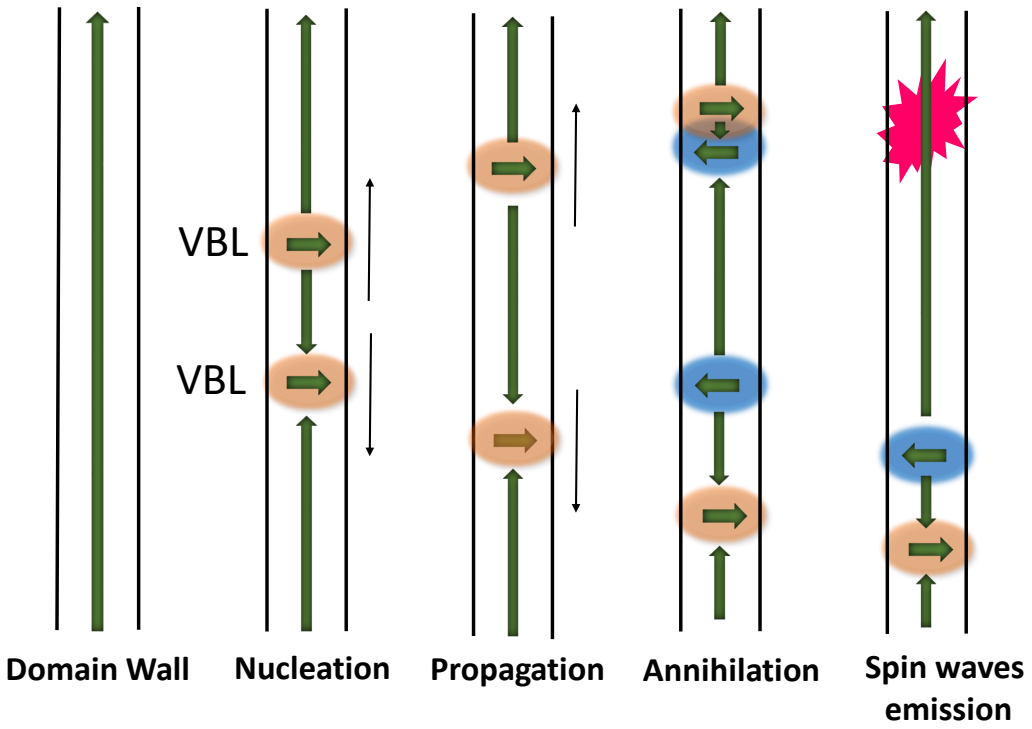

Fig. 5.8 Schematic of the nucleation, propagation and annihilation of vertical Bloch lines inside a domain wall.

not straightforward to explain the flattening shape. It was speculated in their work that the flattened shape could be due to the nucleation of vertical Bloch lines. Our detailed study of the rippled points confirm that the flattening is due to the nucleation and interaction of Vertical Bloch lines. The nucleation of VBLs has been observed for Co/Ni wide strips experimentally [131] and is predicted to occur when H_{DMI} is antiparallel to H_x. When the DMI is stronger, a higher in-plane field is needed for the formation of VBLs to take place. This explains why the onset and minimum points in table 5.1 are higher for higher DMI values. VBLs are high energy regions in the DW and therefore sections of DWs having VBLs have smaller velocities compared to the rest of the DW. Morphologically, they appear as pinned DW points, resulting in the occurrence of the ripples. VBLs are then responsible for reducing the overall velocity of one side of the bubble DW. Furthermore, we expect the velocity of the DW to be inversely proportional to the density of VBLs. Different velocities at different in-plane fields, as shown in Fig. 5.4(a), are related to the difference in the density of VBLs. The velocities of the right and left DWs have also been predicted by Pellegren et al. [135] using a dispersive elastic stiffness model. In this model, the velocities are

calculated from a modified DW elastic energy scale using the creep law. For small length scales, as in the case of our system, this model predicts the onset of the drop in the DW velocity as well as the convergence of RDW and LDW velocities at higher in-plane fields. These remarkable similarities between this model, which assumes non-zero temperature using energy barrier scaling, and our simulations, which are instead simulations of the dynamics performed at zero temperature, suggest that the observed properties of DW propagation under simultaneous application of in-plane and perpendicular fields originate from the intrinsic DW energy.

5.4 1D model of Domain Wall Dynamics and its fitting to domain wall

In order to check whether the motion of the bubble domain is consistent with 1D model of DW motion (discussed in section 2.6) , mobility of the RDW expressed as $\frac{velocity}{width \times B_z}$ as a function of in-plane field is presented in Fig. 5.9. According to the 1D model, mobility of the domain wall is expected to be proportional to the in-plane field. We see in this figure that, DW motion is not consistent with the 1D model in the region where VBLs are nucleated. A violation of the 1D model is in fact expected in the regions with VBLs because in these regions structure of the DW is 2 dimensional.

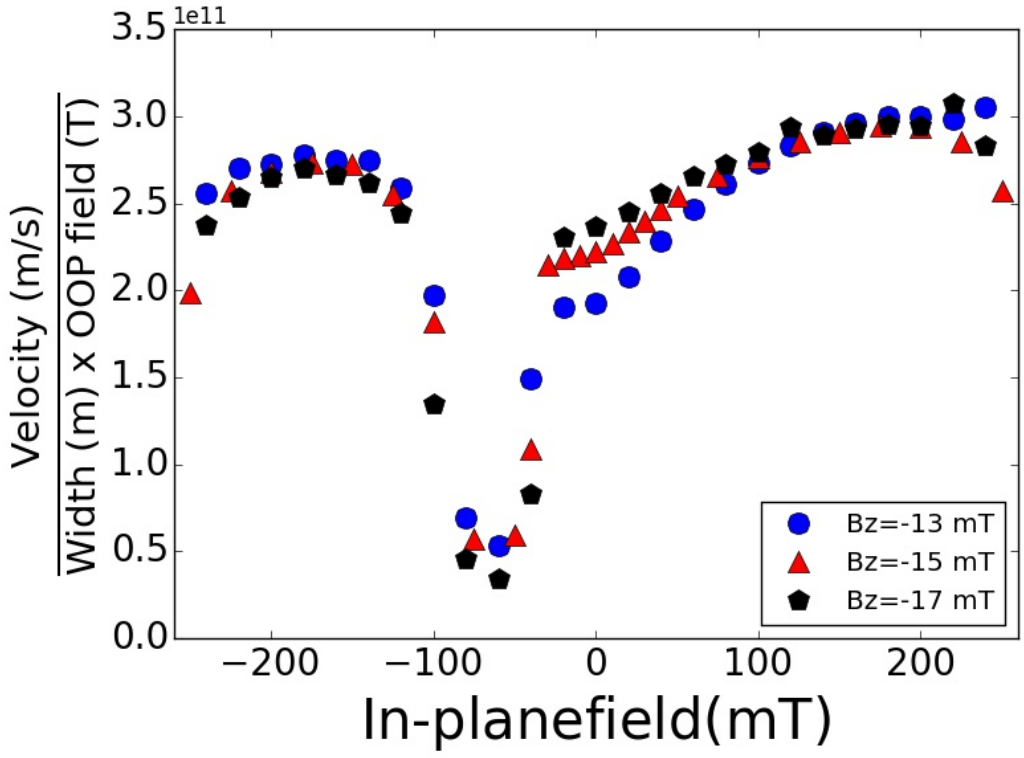

Fig. 5.9 Variation of mobility of the right domain wall expressed as ratio between velocity and product of width and OOP field as a function of in-plane field.

5.5 Comparison with models of DW dynamics

While the analysis based on micromagnetic simulations explains the drop and the minimum of the DW velocity of Fig. 5.4, in the previous section we have seen that, it seems to break the interpretation of the DW dynamics in simple terms, as for 1D class model [26], where a linear relation between velocity and DW width exists. In particular, while the velocity shows a significant dependence on the out-of-plane field, the width is totally unaffected. On the other hand, a failure of simple 1D models is totally expected in case of VBLs nucleation and annihilation. In 1D models, in fact, the magnetic moments inside the DW are assumed to vary only along one dimension and this is not the case when VBLs are present. To account for these discrepancies, a collective coordinate models (CCMs) that go beyond the simple 1D models [136] is extended to the bubble dynamics considered here. For simplicity, it is assumed that the points on the bubble are free and not interacting with each other. Then a local

in-plane field H_{eff}, and a local dipolar field (with demagnetizing factor N) at points on the bubble periphery is introduced as follows:

$$\begin{aligned} H_{x,eff} &= H_X cos(\Omega) + H_Y sin(\Omega) \\ H_{y,eff} &= -H_X sin(\Omega) + H_Y cos(\Omega) \\ N_{x,eff} &= N_X cos(\Omega) + N_Y sin(\Omega) \\ N_{y,eff} &= -N_X sin(\Omega) + N_Y cos(\Omega) \end{aligned} \tag{5.3}$$

where x and y are the local axes over which the equations are written, X and Y are the global axes, as shown in figure 3.7. With these assumptions, the equations derived for the CCMs will be exactly those found in Ref. [136], with no DW tilting and the local fields above replacing the global values. This model is then compared to the results of micromagnetic simulations to assess whether these models are accurate especially considering the disorder included in the model. As depicted in figure 5.10. it was found that by reducing the exchange constant by 43% of the nominal value (equivalent to the amount of exchange constant variation at the grain boundaries), the micromagnetic results could almost be reproduced. As such, the toy model seems to be valid at least for cases of low drive field.

In addition, the CCM can also be used to understand what happens at the ripple points. The steady state solution ($\Phi \sim 0$) for the magnetization angle of the DW in this case reads:

$$cos(\Phi_{eq}) = \frac{1}{2}\left[\frac{I_2^2}{I_1 I_4}\frac{H_z}{H_W} csc(\Phi_{eq}) + \alpha\frac{I_3}{I_4}\frac{H_{DMI}}{H_W} - \alpha\frac{I_6}{I_4}\frac{H_{x,eff} - H_{y,eff} cot(\Phi_{eq})}{H_W}\right] \tag{5.4}$$

where Φ_{eq} is the steady state magnetization, H_W is the conventional Walker Breakdown field, and the I_i are constants calculated for a specific Bloch profile [136]. If the equation above does not have a solution, the magnetization will continue to precess and can be determined using the full collective coordinate model. In the absence of the DMI and in-plane fields, the drive field determines whether Walker breakdown happens. However, in the presence of the in-plane field and DMI, there are two additional parameters that play a role in whether or not precession continues.

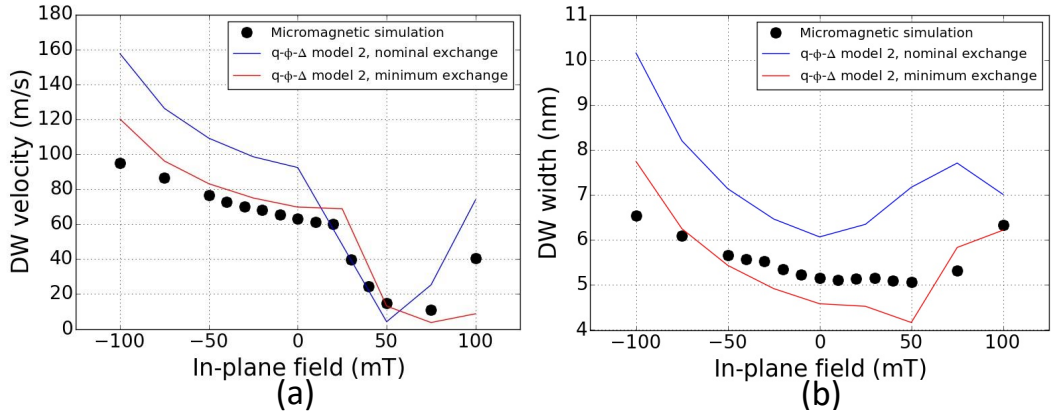

Fig. 5.10 Comparison between the micromagnetic simulations and collective coordinate model for the LDW at a drive field of $B_z = -17\ mT$. Nominal exchange is the actual value of the exchange constant and minimum exchange is the exchange constant after reducing it by 43% of the actual exchange constant.

The fact that the in-plane fields are locally determined means that points of precession can nucleate within the bubble locally, showing local Walker breakdown behavior. Physically speaking, such precessional motion will lead to 2D effects on the bubble, affecting the spin texture around that point and giving rise to the ripple like shape of the bubble. Even though the CCM is effectively a one-dimensional model, such ripples can be observed in the results as well.

5.6 Conclusions

The dynamics of chiral magnetic bubbles in perpendicular magnetic anisotropy materials using micromagnetic simulations in the presence of disorder have been studied. As expected, an asymmetry in the expansion of the bubble in the simultaneous presence of out-of-plane and in-plane fields is observed. There is a range of applied in-plane fields in which a part of the bubble shows ripple-like structures. These ripples cause a kink-like feature in the velocity of the domain wall. We confirm that the generation of ripples is due to the nucleation of vertical Bloch lines. We find that the width of the domain wall depends on the in-plane field and for the first time to our knowledge, it brings us to the remarkable conclusion that DMI field also depends on the in-plane field and is not a constant. Future studies on vertical Bloch lines can shed more light on the dynamics and shape of magnetic bubbles in ultra-thin

films and its effect on the measurement of DMI. Furthermore, the velocity curve fits qualitatively well to a collective coordinate model extended for bubble domain.

Chapter 6

Conclusions and outlook

This thesis deals with the domain wall dynamics in ferromagnetic medium with disorder. Experimental as well as computational tools are used to perform these studies.

Study of effect of light ion irradiation gave us the understanding of the localized pinning points, thereby providing us an excellent tool to manipulate the pinning points at the microscopic level. Other than the controlled disorder using irradiation, material contains intrinsic disorders, accumulated during its growth, in many different spatial scales e.g. atomic vacancies, interstitial atoms at the sub-nanometer scale to dislocations, grain boundaries in the microscopic scales and then to thickness or surface inhomogeneities in the macroscopic scale. The method discussed in this thesis, to extract information such as waiting time of the domain wall and strengths of the pinning points, is universally applicable for any kind of disorders in any material of interest, that works as a pinning site for the moving domain wall. Understanding the strength of the pinning sites and its distribution is of fundamental importance for efficient domain wall motion. Our computational method coupled with ion irradiation provides us an useful tool to control and quantify the strengths and distributions of the pinning points.

In this work, effects of irradiations on the dynamics of domain walls in terms of its waiting time and on the strength and distribution of the pinning points are studied. It is found that irradiation influences the number of pinning sites as well as their strengths. Furthermore, it suggests that there may be an optimal irradiation fluence at which DW dynamics are faster.

On the other hand, studying the dynamics of chiral magnetic bubble domains in perpendicularly magnetized anisotropy materials gave us the understanding of underlying mechanisms behind its shape and morphology. Dynamics of bubble domains in materials with DMI have been of significant interest, because it offers the simplest method for measuring DMI. Our study explains the rippled shapes of bubble domains that have been observed in experiments before. Remarkably, it brings into light the flaw in current DMI measurement method, thus providing suggestions for the experimental method for a more reliable measurement.

In this study, we found that there is a range of applied in-plane fields in which the bubble showed ripple-like structures and these structures influenced the velocity vs. in-plane field curve, thereby also influencing the measured values of DMI field. Our detailed studies showed that these ripples originate due to the nucleation and interaction of vertical Bloch lines. The remarkable result out of this work is that DW width depends on the in-plane field and therefore, DMI field also depends on the in-plane field and is not a constant, unlike assumption in the experiments.

Throughout this thesis, several open topics were identified, that could not be pursued because of time constraints. First of all, it was shown theoretically by A. Rosso [137] that by knowing the curvature of a domain wall around a pinning point, strength of the pinning point can be calculated. In our work, we get the contours of the domain walls around the pinning point. Therefore, it will be interesting to calculate the strengths of these points based on the literature above and then to compare them with the strengths based on waiting time. Then, how does strengths and densities of the pinning points changes as a function of irradiation fluences need to be understood for more irradiation doses in order to have a comprehensive understanding. In the long term, characterization of the pinning points has to be done for current driven domain wall motion, as this is the preferred form of excitation for applications.

From the area of bubble domain dynamics, an immediate next topic to study will be the dynamics of vertical Bloch lines and their influences on the velocities of domain walls. Factors affecting the VBL parameters such as its width, density need to be understood for PMA materials with DMI, since these parameters not only affect the DMI measurement method, but also the velocities of domain walls. On the experiment front, the fact that the width of the domain wall changes as function of in-plane field needs to be taken into consideration while measuring the

DMI. VBLs being the region of high energies, acts as a pinning point for the DWs, thus contributing to the roughness of the domain walls alongwith other disorders. Therefore, contribution of VBLs on the roughness of the DWs will be another interesting question to answer.

References

[1] M. Hilbert and P. López. The world's technological capacity to store, communicate, and compute information. *Science*, 332(6025):60–65, March 2011.

[2] M. R. Gillings, M. Hilbert, and D. J. Kemp. Information in the biosphere: Biological and digital worlds. *Trends in Ecology & Evolution*, 31(3):180–189, March 2016.

[3] P. Lyman and H. R. Varian. How much information? 2003. Technical report, UC Berkeley, School of Information Management and Systems., 2003.

[4] G. Binasch, P. Grünberg, F. Saurenbach, and W. Zinn. Enhanced magnetoresistance in layered magnetic structures with antiferromagnetic interlayer exchange. *Physical Review B*, 39(7):4828–4830, March 1989.

[5] M. N. Baibich, J. M. Broto, A. Fert, F. Nguyen Van Dau, F. Petroff, P. Etienne, G. Creuzet, A. Friederich, and J. Chazelas. Giant magnetoresistance of (001) Fe/(001) Cr magnetic superlattices. *Physical Review Letters*, 61(21):2472–2475, 1988.

[6] S. S. P. Parkin, M. Hayashi, and L. Thomas. Magnetic domain-wall racetrack memory. *Science*, 320(5873):190–194, 2008.

[7] S. S. P. Parkin. Unidirectional racetrack memory device. U.S. patent 7,551,469 B1. June 23, 2009.

[8] D. A. Allwood, G. Xiong, C. C. Faulkner, D. Atkinson, D. Petit, and R. P. Cowburn. Magnetic domain-wall logic. *Science*, 309(5741):1688–1692, 2005.

[9] R. Weiss, R. Mattheis, and G. Reiss. Advanced giant magnetoresistance technology for measurement applications. *Measurement Science and Technology*, 24(8):082001, July 2013.

[10] B. Borie, A. Kehlberger, J. Wahrhusen, H. Grimm, and M. Kläui. Geometrical dependence of domain-wall propagation and nucleation fields in magnetic-domain-wall sensors. *Phys. Rev. Appl*, 8(2), August 2017.

[11] B. Borie, M. Voto, L. Lopez-Diaz, H. Grimm, M. Diegel, M. Kläui, and R. Mattheis. Reliable propagation of magnetic domain walls in cross structures for advanced multiturn sensors. *Phys. Rev. Appl.*, 8(4), October 2017.

[12] D. Jiles. *Introduction to Magnetism and Magnetic Materials*. Springer-Science+Business Media, B.V., 1991.

[13] S. Chikazumi. *Physics of Ferromagnetism (International Series of Monographs on Physics)*. Clarendon Press, 1997.

[14] M. Lubecka, L. J. Maksymowicz, and R. Zuberek. Exchange-interaction constant of polycrystalline $CdCr_2Se_4$ thin films doped with In. *Physical Review B*, 42(7):3926–3928, September 1990.

[15] A.I. Liechtenstein, M.I. Katsnelson, V.P. Antropov, and V.A. Gubanov. Local spin density functional approach to the theory of exchange interactions in ferromagnetic metals and alloys. *Journal of Magnetism and Magnetic Materials*, 67(1):65–74, May 1987.

[16] A. Hubert and R. Schäfer. *Magnetic Domains - The Analysis of Magnetic Microstructures*. Springer, Berlin, New York, Heidelberg, 1998.

[17] A. Fert, V. Cros, and J. Sampaio. Skyrmions on the track. *Nature Nanotechnology*, 8(3):152–156, March 2013.

[18] P. Bak and M.H. Jensen. Theory of helical magnetic structures and phase transitions in MnSi and FeGe. *Journal of Physics C: Solid State Physics*, 13(31):L881–L885, November 1980.

[19] P.M. Levy and A. Fert. Anisotropy induced by nonmagnetic impurities in CuMn spin-glass alloys. *Physical Review B*, 23(9):4667–4690, May 1981.

[20] A. Fert and P.M. Levy. Role of anisotropic exchange interactions in determining the properties of spin-glasses. *Physical Review Letters*, 44(23):1538–1541, June 1980.

[21] A. Fert. Magnetic and transport properties of metallic multilayers. *Materials Science Forum*, 59-60:439–480, 1990.

[22] M. Bode, M. Heide, K. von Bergmann, P. Ferriani, S. Heinze, G. Bihlmayer, A. Kubetzka, O. Pietzsch, S. Blügel, and R. Wiesendanger. Chiral magnetic order at surfaces driven by inversion asymmetry. *Nature*, 447(7141):190–193, May 2007.

[23] P. Ferriani, K. von Bergmann, E.Y. Vedmedenko, S. Heinze, M. Bode, M. Heide, G. Bihlmayer, S. Blügel, and R. Wiesendanger. Atomic-scale spin spiral with a unique rotational sense: Mn monolayer on W(001). *Physical Review Letters*, 101(2), jul 2008.

[24] A. Arrott. Dzialoshinski-moriya interactions about defects in antiferromagnetic and ferromagnetic materials. *Journal of Applied Physics*, 34(4):1108–1109, April 1963.

[25] A. N. Bogdanov and U. K. Rößler. Chiral symmetry breaking in magnetic thin films and multilayers. *Phys. Rev. Lett.*, 87:037203, June 2001.

[26] A. Thiaville, S. Rohart, E. Jué, V. Cros, and A. Fert. Dynamics of Dzyaloshinskii domain walls in ultrathin magnetic films. *Europhys. Lett.*, 100(5):57002, 2012.

[27] V. N. Krivoruchko. Spin waves damping in nanometre-scale magnetic materials (review article). *Low Temperature Physics*, 41(9):670–681, September 2015.

[28] L. Berger. Dragging of domains by an electric current in very pure, non-compensated, ferromagnetic metals. *Physics Letters A*, 46(1):3–4, November 1973.

[29] L. Berger. Prediction of a domain-drag effect in uniaxial, non-compensated, ferromagnetic metals. *Solid State Communications*, 14(6):947–956, March 1974.

[30] L. Berger. Low-field magnetoresistance and domain drag in ferromagnets. *J. Appl. Phys.*, 49(3):2156–2161, 1978.

[31] L. Berger. Domain drag effect in the presence of variable magnetic field or variable transport current. *J. Appl. Phys.*, 50(B3):2137–2139, 1979.

[32] L. Berger. Exchange interaction between ferromagnetic domain wall and electric current in very thin metallic films. *J. Appl. Phys.*, 55(6):1954–1956, 1984.

[33] L. Berger. Possible existence of a Josephson effect in ferromagnets. *Phys. Rev. B*, 33(3):1572–1578, February 1986.

[34] L. Berger. Motion of a magnetic domain wall traversed by fast-rising current pulses. *Journal of Applied Physics*, 71(6):2721–2726, March 1992.

[35] P. P. Freitas and L. Berger. Observation of s-d exchange force between domain walls and electric current in very thin permalloy films. *Journal of Applied Physics*, 57(4):1266–1269, February 1985.

[36] C.-Y. Hung and L. Berger. Exchange forces between domain wall and electric current in permalloy films of variable thickness. *Journal of Applied Physics*, 63(8):4276–4278, April 1988.

[37] J. C. Slonczewski. Current-driven excitation of magnetic multilayers. *J. Magn. Magn. Mat.*, 159(1-2):L1–L7, 1996.

[38] G. Tatara and H. Kohno. Theory of current-driven domain wall motion: Spin transfer versus momentum transfer. *Phys. Rev. Lett.*, 92(8):086601, 2004.

[39] X. Waintal and M. Viret. Current-induced distortion of a magnetic domain wall. *Europhys. Lett.*, 65(3):427, 2004.

[40] A. Vanhaverbeke and M. Viret. Simple model of current-induced spin torque in domain walls. *Physical Review B*, 75(2), January 2007.

[41] S. Zhang and Z. Li. Roles of nonequilibrium conduction electrons on the magnetization dynamics of ferromagnets. *Phys. Rev. Lett.*, 93(12):127204, 2004.

[42] A. Thiaville, Y. Nakatani, J. Miltat, and Y. Suzuki. Micromagnetic understanding of current-driven domain wall motion in patterned nanowires. *Europhys. Lett.*, 69:990–996, 2005.

[43] A. Brataas, A. D. Kent, and H. Ohno. Current-induced torques in magnetic materials. *Nat. Mater.*, 11(5):372–381, May 2012.

[44] M. Hayashi, L. Thomas, Ya. B. Bazaliy, C. Rettner, R. Moriya, X. Jiang, and S. S. P. Parkin. Influence of current on field-driven domain wall motion in permalloy nanowires from time resolved measurements of anisotropic magnetoresistance. *Phys. Rev. Lett.*, 96(19):197207, 2006.

[45] M. D. Stiles, W. M. Saslow, M. J. Donahue, and A. Zangwill. Adiabatic domain wall motion and Landau-Lifshitz damping. *Phys. Rev. B*, 75:214423, June 2007.

[46] M. I. D'Yakonov and V. I. Perel'. Possibility of orienting electron spins with current. *Journal of Experimental and Theoretical Physics Letters*, 13:467, June 1971.

[47] A. V. Khvalkovskiy, V. Cros, D. Apalkov, V. Nikitin, M. Krounbi, K. A. Zvezdin, A. Anane, J. Grollier, and A. Fert. Matching domain-wall configuration and spin-orbit torques for efficient domain-wall motion. *Phys. Rev. B*, 87:020402, January 2013.

[48] K. Garello, I. M. Miron, C. O. Avci, F. Freimuth, Y. Mokrousov, Stefan Blügel, Stéphane Auffret, O. Boulle, G. Gaudin, and P. Gambardella. Symmetry and magnitude of spin-orbit torques in ferromagnetic heterostructures. *Nat. Nano.*, 8(8):587–593, August 2013.

[49] W. Döring. Über die Trägheit der Wände zwischen Weißschen Bezirken. *Z. Naturforsch*, 3a:373–379, 1948.

[50] T. L. Gilbert. *Formulation, foundations and applications of the phenomenological theory of ferromagnetism*. PhD thesis, Illinois Institute of Technology, Chicago, 1956.

[51] W. F. Brown. *Micromagnetics*. Wiley Interscience, New York, 1963.

[52] P. Chauve, T. Giamarchi, and P. Le Doussal. Creep and depinning in disordered media. *Physical Review B*, 62(10):6241–6267, September 2000.

[53] T.C. Huang, R. Gilles, and G. Will. Thin-film thickness and density determination from x-ray reflectivity data using a conventional power diffractometer. *Thin Solid Films*, 230(2):99–101, August 1993.

[54] L. Lutterotti, D. Chateigner, S. Ferrari, and J. Ricote. Texture, residual stress and structural analysis of thin films using a combined x-ray analysis. *Thin Solid Films*, 450(1):34–41, February 2004.

[55] A. Lamperti, S.-M. Ahn, B. Ocker, R. Mantovan, and D. Ravelosona. Interface width evaluation in thin layered CoFeB/MgO multilayers including Ru or Ta buffer layer by x-ray reflectivity. *Thin Solid Films*, 533:79–82, apr 2013.

[56] L. E. Rehn and P. R. Okamoto. Recent progress in understanding ion-beam mixing of metals. *Nuclear Instruments and Methods in Physics Research Section B: Beam Interactions with Materials and Atoms*, 39(1-4):104–113, March 1989.

[57] M. G. Le Boité, A. Traverse, H. Bernas, C. Janot, and J. Chevrier. Study of ion beam mixed multilayers via neutron scattering. *Materials Letters*, 6(5-6):173–176, March 1988.

[58] M. G. Le Boité, A. Traverse, L. Névot, B. Pardo, and J. Corno. Characterization of ion-beam mixed multilayers via grazing x-ray reflectometry. *Journal of Materials Research*, 3(06):1089–1096, December 1988.

[59] A Traverse, M. G. Le Boité, and G Martin. Quantitative description of mixing with light ions. *Europhysics Letters (EPL)*, 8(7):633–637, April 1989.

[60] J. Chaumont, F. Lalu, M. Salome, A.-M. Lamoise, and H. Bernas. A medium energy facility for variable temperature implantation and analysis. *Nuclear Instruments and Methods in Physics Research*, 189(1):193–198, October 1981.

[61] T. Lahtinen. Ferromagnetic-ferroelectric domain coupling in multiferroic heterostructures. PhD dissertation, 2013.

[62] A. Vansteenkiste and B. Van de Wiele. Mumax: A new high-performance micromagnetic simulation tool. *J. Magn. Magn. Mat.*, 323(21):2585–2591, 2011.

[63] A. Vansteenkiste, J. Leliaert, M. Dvornik, M. Helsen, F. Garcia-Sanchez, and B. Van Waeyenberge. The design and verification of MuMax3. *AIP Advances*, 4(10):107133, October 2014.

[64] J. Leliaert, M. Dvornik, J. Mulkers, J. De Clercq, M. V. Milošević, and B. Van Waeyenberge. Fast micromagnetic simulations on GPU - recent advances made with mumax^3. *Journal of Physics D: Applied Physics*, January 2018.

[65] K.-J. Kim, J.-C. Lee, S.-M. Ahn, K.-S. Lee, C.-W. Lee, Y. J. Cho, S. Seo, K.-H. Shin, S.-B. Choe, and H.-W. Lee. Interdimensional universality of dynamic interfaces. *Nature*, 458(7239):740–742, April 2009.

[66] J. Leliaert, B. Van de Wiele, A. Vansteenkiste, L. Laurson, G. Durin, L. Dupré, and B. Van Waeyenberge. A numerical approach to incorporate intrinsic material defects in micromagnetic simulations. *J. Appl. Phys.*, 115(17):17D102, 2014.

[67] J. Leliaert, B. Van de Wiele, A. Vansteenkiste, L. Laurson, G. Durin, L. Dupré, and B. Van Waeyenberge. Current-driven domain wall mobility in polycrystalline permalloy nanowires: A numerical study. *J. Appl. Phys.*, 115(23):233903, 2014.

[68] J. Leliaert, B. Van de Wiele, A. Vansteenkiste, L. Laurson, G. Durin, Luc Dupré, and B. Van Waeyenberge. Influence of material defects on current-driven vortex domain wall mobility. *Phys. Rev. B*, 89:064419, February 2014.

[69] T. Kishi, H. Yoda, T. Kai, T. Nagase, E. Kitagawa, M. Yoshikawa, K. Nishiyama, T. Daibou, M. Nagamine, M. Amano, S. Takahashi, M. Nakayama, N. Shimomura, H. Aikawa, S. Ikegawa, S. Yuasa, K. Yakushiji, H. Kubota, A. Fukushima, M. Oogane, T. Miyazaki, and K. Ando. Lower-current and fast switching of a perpendicular TMR for high speed and high density spin-transfer-torque MRAM. In *2008 IEEE International Electron Devices Meeting*. IEEE, December 2008.

[70] S. Mangin, D. Ravelosona, J. A. Katine, M. J. Carey, B. D. Terris, and Eric E. Fullerton. Current-induced magnetization reversal in nanopillars with perpendicular anisotropy. *Nature Materials*, 5(3):210–215, February 2006.

[71] H. Meng and J.-P. Wang. Spin transfer in nanomagnetic devices with perpendicular anisotropy. *Applied Physics Letters*, 88(17):172506, April 2006.

[72] M. Yoshikawa, E. Kitagawa, T. Nagase, T. Daibou, M. Nagamine, K. Nishiyama, T. Kishi, and H. Yoda. Tunnel magnetoresistance over 100% in MgO-based magnetic tunnel junction films with perpendicular magnetic $L1_0$- FePt electrodes. , 44(11):2573–2576, November 2008.

[73] G. Kim, Y. Sakuraba, M. Oogane, Y. Ando, and T. Miyazaki. Tunneling magnetoresistance of magnetic tunnel junctions using perpendicular magnetization L10-CoPt electrodes. *Applied Physics Letters*, 92(17):172502, April 2008.

[74] J.-H. Park, C. Park, T. Jeong, M. T. Moneck, N. T. Nufer, and J.-G. Zhu. Co-Pt multilayer based magnetic tunnel junctions using perpendicular magnetic anisotropy. *Journal of Applied Physics*, 103(7):07A917, April 2008.

[75] B. Carvello, C. Ducruet, B. Rodmacq, S. Auffret, E. Gautier, G. Gaudin, and B. Dieny. Sizable room-temperature magnetoresistance in cobalt based magnetic tunnel junctions with out-of-plane anisotropy. *Applied Physics Letters*, 92(10):102508, March 2008.

[76] K. Mizunuma, S. Ikeda, J. H. Park, H. Yamamoto, H. Gan, K. Miura, H. Hasegawa, J. Hayakawa, F. Matsukura, and H. Ohno. MgO barrier-perpendicular magnetic tunnel junctions with CoFe/Pd multilayers and ferromagnetic insertion layers. *Applied Physics Letters*, 95(23):232516, December 2009.

[77] T. Manago and H. Akinaga. Direct observation of magnetization reversal of epitaxial MnAs films. *Surface Science*, 600(17):3492–3495, September 2006.

[78] H. Ohmori, T. Hatori, and S. Nakagawa. Perpendicular magnetic tunnel junction with tunneling magnetoresistance ratio of 64% using MgO (100) barrier layer prepared at room temperature. *Journal of Applied Physics*, 103(7):07A911, April 2008.

[79] N. Nishimura, T. Hirai, A. Koganei, T. Ikeda, K. Okano, Y. Sekiguchi, and Y. Osada. Magnetic tunnel junction device with perpendicular magnetization films for high-density magnetic random access memory. *Journal of Applied Physics*, 91(8):5246–5249, April 2002.

[80] S. Ikeda, K. Miura, H. Yamamoto, K. Mizunuma, H. D. Gan, M. Endo, S. Kanai, J. Hayakawa, F. Matsukura, and H. Ohno. A perpendicular-anisotropy CoFeB–MgO magnetic tunnel junction. *Nature Materials*, 9(9):721–724, July 2010.

[81] Y. M. Lee, J. Hayakawa, S. Ikeda, F. Matsukura, and H. Ohno. Effect of electrode composition on the tunnel magnetoresistance of pseudo-spin-valve magnetic tunnel junction with a MgO tunnel barrier. *Applied Physics Letters*, 90(21):212507, May 2007.

[82] A. T. G. Pym, A. Lamperti, B. K. Tanner, T. Dimopoulos, M. Rhrig, and J. Wecker. Interface sharpening in CoFeB magnetic tunnel junctions. *Applied Physics Letters*, 88(16):162505, April 2006.

[83] S. Isogami, M. Tsunoda, K. Komagaki, K. Sunaga, Y. Uehara, M. Sato, T. Miyajima, and M. Takahashi. In situ heat treatment of ultrathin MgO layer for giant magnetoresistance ratio with low resistance area product in CoFeB/MgO/CoFeB magnetic tunnel junctions. *Applied Physics Letters*, 93(19):192109, November 2008.

[84] S. Monso, B. Rodmacq, S. Auffret, G. Casali, F. Fettar, B. Gilles, B. Dieny, and P. Boyer. Crossover from in-plane to perpendicular anisotropy in Pt/CoFe/AlO_x sandwiches as a function of Al oxidation: A very accurate control of the oxidation of tunnel barriers. *Applied Physics Letters*, 80(22):4157–4159, June 2002.

[85] N. Ding, T. L. Wang, K. P. Tai, J. H. Li, X. He, Y. Dai, and B. X. Liu. Structural phase transition in the Fe-Ta system studied by ion beam mixing. *Journal of Alloys and Compounds*, 476(1-2):253–256, May 2009.

[86] S. S. P. Parkin, C. Kaiser, A. Panchula, P. M. Rice, B. Hughes, M. Samant, and S.-H. Yang. Giant tunnelling magnetoresistance at room temperature with MgO (100) tunnel barriers. *Nature Materials*, 3(12):862–867, October 2004.

[87] J. H. Jung, S. H. Lim, and S. R. Lee. Strong perpendicular magnetic anisotropy in thick CoFeB films sandwiched by Pd and MgO layers. *Applied Physics Letters*, 96(4):042503, January 2010.

[88] L. Liu, O. J. Lee, T. J. Gudmundsen, D. C. Ralph, and R. A. Buhrman. Current-induced switching of perpendicularly magnetized magnetic layers using spin torque from the spin hall effect. *Physical Review Letters*, 109(9), August 2012.

[89] W.-G. Wang, M. Li, S. Hageman, and C. L. Chien. Electric-field-assisted switching in magnetic tunnel junctions. *Nature Materials*, 11(1):64–68, November 2011.

[90] T. Liu, J. W. Cai, and Li Sun. Large enhanced perpendicular magnetic anisotropy in CoFeB/MgO system with the typical Ta buffer replaced by an Hf layer. *AIP Advances*, 2(3):032151, September 2012.

[91] Y.-W. Oh, K.-D. Lee, J.-R. Jeong, and B.-G. Park. Interfacial perpendicular magnetic anisotropy in CoFeB/MgO structure with various underlayers. *Journal of Applied Physics*, 115(17):17C724, May 2014.

[92] J. Sinha, M. Hayashi, A. J. Kellock, S. Fukami, M. Yamanouchi, H. Sato, S. Ikeda, S. Mitani, S.-H. Yang, S. S. P. Parkin, and H. Ohno. Enhanced interface perpendicular magnetic anisotropy in Ta|CoFeB|MgO using nitrogen doped ta underlayers. *Applied Physics Letters*, 102(24):242405, June 2013.

[93] A. Barman, S. Wang, O. Hellwig, A. Berger, Eric E. Fullerton, and H. Schmidt. Ultrafast magnetization dynamics in high perpendicular anisotropy $[Co/Pt]_n$ multilayers. *Journal of Applied Physics*, 101(9):09D102, May 2007.

[94] S.-M. Ahn and G. S. D. Beach. Crossover between in-plane and perpendicular anisotropy in Ta/Co_xFe_{100-x}/MgO films as a function of Co composition. *Journal of Applied Physics*, 113(17):17C112, May 2013.

[95] M. Yamanouchi, R. Koizumi, S. Ikeda, H. Sato, K. Mizunuma, K. Miura, H. D. Gan, F. Matsukura, and H. Ohno. Dependence of magnetic anisotropy on MgO thickness and buffer layer in $Co_{20}Fe_{60}B_{20}$-MgO structure. *Journal of Applied Physics*, 109(7):07C712, April 2011.

[96] C. Burrowes, N. Vernier, J.-P. Adam, L. Herrera Diez, K. Garcia, I. Barisic, G. Agnus, S. Eimer, Joo-Von Kim, T. Devolder, and et al. Low depinning fields in Ta-CoFeB-MgO ultrathin films with perpendicular magnetic anisotropy. *Appl. Phys. Lett.*, 103(18):182401, 2013.

[97] A. P. Mihai, J. P. Attané, L. Vila, C. Beigné, J. C. Pillet, and A. Marty. Magnetization reversal dominated by domain wall pinning in FePt based spin valves. *Applied Physics Letters*, 94(12):122509, March 2009.

[98] P. J. Metaxas, J. P. Jamet, A. Mougin, M. Cormier, J. Ferré, V. Baltz, B. Rodmacq, B. Dieny, and R. L. Stamps. Creep and flow regimes of magnetic domain-wall motion in ultrathin Pt/Co/Pt films with perpendicular anisotropy. *Physical Review Letters*, 99(21), November 2007.

[99] K. Yamada, J.-P. Jamet, Y. Nakatani, A. Mougin, A. Thiaville, T. Ono, and J. Ferré. Influence of instabilities on high-field magnetic domain wall velocity in (Co/Ni) nanostrips. *Applied Physics Express*, 4(11):113001, October 2011.

[100] C. Chappert. Planar patterned magnetic media obtained by ion irradiation. *Science*, 280(5371):1919–1922, June 1998.

[101] T. Devolder, J. Ferré, C. Chappert, H. Bernas, J.-P. Jamet, and V. Mathet. Magnetic properties of He^+-irradiated Pt/Co/Pt ultrathin films. *Physical Review B*, 64(6), July 2001.

[102] T. Devolder. Light ion irradiation of Co/Pt systems: Structural origin of the decrease in magnetic anisotropy. *Physical Review B*, 62(9):5794–5802, September 2000.

[103] L. Herrera Diez, F. Garcia-Sanchez, J.-P. Adam, T. Devolder, S. Eimer, M. S. El Hadri, A. Lamperti, R. Mantovan, B. Ocker, and D. Ravelosona. Controlling magnetic domain wall motion in the creep regime in He^+-irradiated CoFeB/MgO films with perpendicular anisotropy. *Applied Physics Letters*, 107(3):032401, 2015.

[104] X. Chen, K. Y. Wang, Z. L. Wu, S. L. Jiang, G. Yang, Y. Liu, J. Teng, and G. H. Yu. Interfacial electronic structure-modulated magnetic anisotropy in Ta/CoFeB/MgO/Ta multilayers. *Applied Physics Letters*, 105(9):092402, 2014.

[105] T. Devolder, I. Barisic, S. Eimer, K. Garcia, J.-P. Adam, B. Ockert, and D. Ravelosona. Irradiation-induced tailoring of the magnetism of CoFeB/MgO ultrathin films. *Journal of Applied Physics*, 113(20):203912, May 2013.

[106] D. Ravelosona. *Nanoscale Magnetic Materials and Applications*. Springer US, 2009.

[107] K. J. Måløy, S. Santucci, J. Schmittbuhl, and R. Toussaint. Local waiting time fluctuations along a randomly pinned crack front. *Physical Review Letters*, 96(4), January 2006.

[108] K. T. Tallakstad, R. Toussaint, S. Santucci, J. Schmittbuhl, and K. J. Måløy. Local dynamics of a randomly pinned crack front during creep and forced propagation: An experimental study. *Physical Review E*, 83(4), April 2011.

[109] M. Hayashi, L. Thomas, C. Rettner, R. Moriya, and S. S. P. Parkin. Direct observation of the coherent precession of magnetic domain walls propagating along permalloy nanowires. *Nat. Phys.*, 3(1):21–25, 2007.

[110] S. Lepadatu, A. Vanhaverbeke, D. Atkinson, R. Allenspach, and C. H. Marrows. Dependence of domain-wall depinning threshold current on pinning profile. *Phys. Rev. Lett.*, 102(12):127203, 2009.

[111] M. Kläui, C. A. F. Vaz, J. A. C. Bland, W. Wernsdorfer, G. Faini, E. Cambril, L. J. Heyderman, F. Nolting, and U. Rudiger. Controlled and reproducible domain wall displacement by current pulses injected into ferromagnetic ring structures. *Phys. Rev. Lett.*, 94(10):106601, 2005.

[112] A. Yamaguchi, T. Ono, S. Nasu, K. Miyake, K. Mibu, and T. Shinjo. Real-space observation of current-driven domain wall motion in submicron magnetic wires. *Phys. Rev. Lett.*, 92(7):077205, 2004.

[113] G. Meier, M. Bolte, R. Eiselt, B. Krüger, D.-H. Kim, and P. Fischer. Direct imaging of stochastic domain-wall motion driven by nanosecond current pulses. *Phys. Rev. Lett.*, 98(18):187202, 2007.

[114] L. San Emeterio Alvarez, K.-Y. Wang, S. Lepadatu, S. Landi, S. J. Bending, and C. H. Marrows. Spin-transfer-torque-assisted domain-wall creep in a Co/Pt multilayer wire. *Phys. Rev. Lett.*, 104(13), April 2010.

[115] O. Boulle, J. Kimling, P. Warnicke, M. Kläui, U. Rüdiger, G. Malinowski, H. J. M. Swagten, B. Koopmans, C. Ulysse, and G. Faini. Nonadiabatic spin transfer torque in high anisotropy magnetic nanowires with narrow domain walls. *Phys. Rev. Lett.*, 101(21), November 2008.

[116] S. Emori, U. Bauer, S.-M. Ahn, E. Martinez, and G. S. D. Beach. Current-driven dynamics of chiral ferromagnetic domain walls. *Nat. Mater.*, 12(7):611–616, July 2013.

[117] I. Dzyaloshinsky. A thermodynamic theory of "weak" ferromagnetism of antiferromagnetics. *Journal of Physics and Chemistry of Solids*, 4(4):241–255, January 1958.

[118] T. Moriya. Anisotropic superexchange interaction and weak ferromagnetism. *Phys. Rev.*, 120:91–98, October 1960.

[119] K.-J. Kim, J.-C. Lee, K.-H. Shin, H.-W. Lee, and S.-B. Choe. Universal classes of magnetic-field- and electric-current-induced magnetic domain-wall dynamics in one and two dimensional regimes. *Current Applied Physics*, 13(1):228 – 236, 2013.

[120] K.-S. Ryu, L. Thomas, S.-H. Yang, and S. S. P. Parkin. Chiral spin torque at magnetic domain walls. *Nat Nano*, 8(7):527–533, July 2013.

[121] O. J. Lee, L. Q. Liu, C. F. Pai, Y. Li, H. W. Tseng, P. G. Gowtham, J. P. Park, D. C. Ralph, and R. A. Buhrman. Central role of domain wall depinning for perpendicular magnetization switching driven by spin torque from the spin hall effect. *Phys. Rev. B*, 89:024418, Jan 2014.

[122] S.-G. Je, D.-H. Kim, S.-C. Yoo, B.-C. Min, K.-J. Lee, and S.-B. Choe. Asymmetric magnetic domain-wall motion by the dzyaloshinskii-moriya interaction. *Phys. Rev. B*, 88:214401, December 2013.

[123] A. Hrabec, N. A. Porter, A. Wells, M. J. Benitez, G. Burnell, S. McVitie, D. McGrouther, T. A. Moore, and C. H. Marrows. Measuring and tailoring the dzyaloshinskii-moriya interaction in perpendicularly magnetized thin films. *Phys. Rev. B*, 90:020402, Jul 2014.

[124] S. Jaiswal, K. Litzius, I. Lemesh, F. Büttner, S. Finizio, J. Raabe, M. Weigand, K. Lee, J. Langer, B. Ocker, G. Jakob, G. S. D. Beach, and M. Kläui. Investigation of the dzyaloshinskii-moriya interaction and room temperature skyrmions in W/CoFeB/MgO thin films and microwires. *Applied Physics Letters*, 111(2):022409, July 2017.

[125] R. Soucaille, M. Belmeguenai, J. Torrejon, J.-V. Kim, T. Devolder, Y. Roussigné, S.-M. Chérif, A. A. Stashkevich, M. Hayashi, and J.-P. Adam. Probing the dzyaloshinskii-moriya interaction in CoFeB ultrathin films using domain wall creep and brillouin light spectroscopy. *Physical Review B*, 94(10), September 2016.

[126] R. A. Khan, P. M. Shepley, A. Hrabec, A. W. J. Wells, B. Ocker, C. H. Marrows, and T. A. Moore. Effect of annealing on the interfacial dzyaloshinskii-moriya interaction in Ta/CoFeB/MgO trilayers. *Applied Physics Letters*, 109(13):132404, September 2016.

[127] R. Lavrijsen, D. M. F. Hartmann, A. van den Brink, Y. Yin, B. Barcones, R. A. Duine, M. A. Verheijen, H. J. M. Swagten, and B. Koopmans. Asymmetric magnetic bubble expansion under in-plane field in Pt/Co/Pt: Effect of interface engineering. *Physical Review B*, 91(10), March 2015.

[128] S. Tacchi, R. E. Troncoso, M. Ahlberg, G. Gubbiotti, M. Madami, J. Åkerman, and P. Landeros. Interfacial Dzyaloshinskii-Moriya interaction in Pt/CoFeB films: Effect of the heavy-metal thickness. *Physical Review Letters*, 118(14), April 2017.

[129] N. S. Kiselev, A. N. Bogdanov, R. Schäfer, and U. K. Rößler. Chiral skyrmions in thin magnetic films: new objects for magnetic storage technologies? *Journal of Physics D: Applied Physics*, 44(39):392001, September 2011.

[130] E. Jué, A. Thiaville, S. Pizzini, J. Miltat, J. Sampaio, L. D. Buda-Prejbeanu, S. Rohart, J. Vogel, M. Bonfim, O. Boulle, and et al. Domain wall dynamics in ultrathin Pt/Co/AlO_x microstrips under large combined magnetic fields. *Phys. Rev. B*, 93(1), January 2016.

[131] Y. Yoshimura, K.-J. Kim, T. Taniguchi, T. Tono, K. Ueda, R. Hiramatsu, T. Moriyama, K. Yamada, Y. Nakatani, and T. Ono. Soliton-like magnetic domain wall motioninducedby the interfacial Dzyaloshinskii-Moriya interaction. *Nature Physics*, November 2015.

[132] H.-B. Braun. Topological effects in nanomagnetism: from superparamagnetism to chiral quantum solitons. *Adv. Phys.*, 61(1):1–116, February 2012.

[133] D.-Y. Kim, D.-H. Kim, and S.-B. Choe. Intrinsic asymmetry in chiral domain walls due to the Dzyaloshinskii-Moriya interaction. *Applied Physics Express*, 9(5):053001, April 2016.

[134] D. Lau, V. Sundar, J.-G. Zhu, and V. Sokalski. Energetic molding of chiral magnetic bubbles. *Physical Review B*, 94(6), August 2016.

[135] J. P. Pellegren, D. Lau, and V. Sokalski. Dispersive stiffness of Dzyaloshinskii domain walls. *Phys. Rev. Lett.*, 119(2), July 2017.

[136] S. Ali Nasseri, Eduardo Martinez, and Gianfranco Durin. Collective coordinate descriptions of magnetic domain wall motion in perpendicularly magnetized nanostructures under the application of in-plane fields. *Journal of Magnetism and Magnetic Materials*, 468:25–43, December 2018.

[137] Alberto Rosso. *Depiegeage de varietes elastiques en milieu aleatoire*. PhD thesis, Analyse de donnees, Statistiques et Probabilites. Universite Pierre et Marie Curie - Paris VI, Francais., 2002.